STUDIES OF BLOOD FLOW IN ARTERIAL BIFURCATIONS : FROM INFLUENCE OF HEMODYNAMICS ON ENDOTHELIAL CELL RESPONSE TO VESSEL WALL MECHANICS

by

Bong Jae Chung

B.S., Kyung Hee University, 1990

M.S., University of Pittsburgh, 1998

Submitted to the Graduate Faculty of

School of Engineering in partial fulfillment

of the requirements for the degree of

Doctor of Philosophy

University of Pittsburgh

2004

UNIVERSITY OF PITTSBURGH

SCHOOL OF ENGINEERING

This dissertation was presented

by

Bong Jae Chung

It was defended on

April 8, 2004

and approved by

G. P. Galdi, Professor, Department of Mechanical Engineering, University of Pittsburgh

D. A. Vorp, Associate Professor, Department of Surgery and Bioengineering, University of Pittsburgh

D. G. Peters, Assistant Professor, Department of Medicine, Division of Pulmonary, Allergy and Critical Care Medicine, University of Pittsburgh

P. Smolinski, Associate Professor, Department of Mechanical Engineering, University of Pittsburgh

Dissertation Director: Anne M. Robertson, Associate Professor, Department of Mechanical Engineering

ABSTRACT

STUDIES OF BLOOD FLOW IN ARTERIAL BIFURCATIONS : FROM INFLUENCE OF HEMODYNAMICS ON ENDOTHELIAL CELL RESPONSE TO VESSEL WALL MECHANICS

Bong Jae Chung, Ph.D.

University of Pittsburgh, 2004

The pathology of arterial diseases such as aneurysms and atherosclerosis is of great clinical interest. Several decades have passed since attempts to correlate hemodynamic factors to pathology of these diseases began. Under the hypothesis that hemodynamics is an important factor responsible for arterial diseases, we attempt to (i) investigate geometrical risk factors responsible for aneurysm formation in arterial bifurcations, (ii) evaluate a current hypothesis that aneurysms develop as a result of purely inertial effects on pressure fields at bifurcations (iii) design a novel flow chamber which reproduces flow fields found at arterial bifurcations to study endothelial cell functions due to hemodynamic stresses and (iv) develop a small on large theory for modeling small periodic motions of arterial walls superposed on large deformations. An outcome of this work included the development of a new methodology for generating realistic idealized bifurcation models.

A number of researchers have identified geometric features common to arterial bifurcations. Here, idealized models have been developed that contain all these geometric features. These idealized models are used to investigate effects of Re, radius of curvature and bifurcation angle on arterial bifurcations. Elevated pressure and wall shear stress at the apex of

bifurcation, which could be responsible for aneurysm formation, are found to arise as the fluid is diverted into the two daughter branches. Careful modeling of the apex region of the bifurcation is found to be needed for study of aneurysm due the important role of radius of curvature. The bifurcation angle is found to have only minor influence on the stresses at the apex region. Through this analysis, we found that the elevated wall shear stress at the apex is likely an important risk factor responsible for the formation of aneurysms.

Based on the results from the computational bifurcation study, a flow device was designed to test the response of endothelial cells to wall shear stresses found at arterial bifurcations. The function of endothelial cells responding to hemodynamic stresses are hypothesized to degrade arterial walls and in turn, possibly cause initiation of aneurysms. Through numerical and analytical studies, we successfully designed a novel flow chamber which has two flow regimes : one for testing the cells exposed to wall shear stresses found in straight arteries and the other found at arterial bifurcations. This second section recreates the quantitative and qualitative features of flow fields found at arterial bifurcations.

In order to model blood and arterial wall interaction in studies of hemodynamic factors related to arterial diseases and aging, a constitutive model for the vessel wall is required. Based on multi-mechanism theory, the role of elastin and collagen fibers, responsible for the passive mechanical response of arteries, are included as separate mechanisms. This theory is then used with small on large theory which approximates large deformations as the superposition of a small deformation on a large deformation. Taking this approach, the prestretch and preloading of the vessel can be included. Since deformations due to oscillatory motions of arterial walls are reported to be small compared with deformations due to the preloadings, the small on large theory is appropriate. The novelty of this study was to (i) employ a nonlinear constitutive equation for the large deformation region, (ii) develop governing equations for the wall motion using a small on large theory and (iii) include the separate roles of elastin and collagen fibers in modeling vessel walls.

TABLE OF CONTENTS

LIST OF TABLES

LIST OF FIGURES

ACKNOWLEDGMENT

Many people supported me during the completion of this thesis with helpful criticism, assistance and references. This thesis would have never been possible without them. First of all, I would like to express my deepest sense of gratitude to my supervisor Dr. Anne M. Robertson for her patient guidance, encouragement and excellent advice throughout this study. My sincere thanks will also extend to other members of my committee, Dr. G.P. Galdi, Dr. D.A. Vorp, Dr. D.G. Peters and Dr. P. Smolinski. I also thank Dr. A. Quarteroni for giving me the opportunity to visit the Swiss Federal Institute of Technology (EPFL) as a visiting researcher during the summer of 2003 and Dr. R. Russo, G. Starita and P. Maremonti of the University of Naples II, Italy for the opportunity to attend the international conference, Contemporary Challenges in Applied Fluid Dynamics held in Capo Miseno, Italy in the summer of 2001.

I am thankful to my colleagues Ashwin, Doni, Igor, Has, Khaled, David, Fernando and Raffaella for sharing experiences and knowledge during the time of study.

The investigation was supported by the grants from (i) the National Science Foundation CTS-9870488, (ii) The Whitaker Foundation RG-96-0544, (iii) Office of Naval Research N00014-02-1-0436 and (iv) the National Science Foundation 0104680.

Finally, I would like to express my deepest gratitude for the constant support, understanding and love that I received from my parents in law, my sister, my brothers, my brothers in law during the past years. I also would like to convey my special thanks to my beloved parents, Ha Un Chung and Doo Hei Goo and my darling wife, In Soon Yoo for being extraordinarily supportive especially during my PhD years. This work would not be possible without their love and encouragement.

Dedicated to My Parents and My Wife

1.0 INTRODUCTION

A cerebral aneurysm is one type of arterial disease of the human cerebral vasculature. When an aneurysm ruptures, the blood flooded into the subarachnoid space or brain parenchyma causes a subarachnoid hemorrhage (SAH) or occasionally an intracerebral hemorrhage (ICH). In 50% of the cases, this is fatal.[154–156] Cerebral aneurysms are mostly found at apecies of arterial bifurcations or the neck of curved arteries.[71, 79–81] We confine our attention to arterial bifurcations in this work. The etiology of the cerebral aneurysms has been debated by a number of authors.[80, 102, 105, 122] Some researchers believe that aneurysms originate from congenital factors[80, 105] while some authors hypothesize that biomechanical factors play important roles in the genesis, growth and rupture of aneurysms.[24, 102, 103, 122] In this work, we hypothesize that hemodynamic forces are important factors in the formation of aneurysms near the apecies of arterial bifurcations.

If hemodynamics plays an important role in the initiation of aneurysms, mechanical forces such as pressure and shear force acting on the apex region of the bifurcation must be responsible for aneurysm formation. The local pressure is mildly elevated at the region of the bifurcation due to momentum transfer and the wall shear stress found near the apex region varies along the neck of the bifurcation and is highly elevated near the apex. These local forces found at the apex of the bifurcation may damage the walls near the bifurcation and thereby, lead to the development of aneurysms. Typically, the flow in the bifurcation is characterized by a given volume flow rate, fluid properties and geometrical shape. Therefore, risk factors for aneurysm development may be related to Reynolds number and geometry.

We hypothesize that the magnitude of wall stress at the apex of the bifurcation is significantly elevated, challenging the homeostasis of the arterial wall in this region. We explore risk factors based on this hypothesis. In order to find the risk factors, idealized geometric models of arterial bifurcations are developed and used in numerical analysis to compute the flow fields in the bifurcation. The idealized models are carefully constructed to include

key geometric features found in *in vivo* arterial bifurcations. The models including the key geometric features are then used to explore Reynolds number and geometric effects. Several authors explored the role of geometric risk factors in atherosclerosis and have studied the effect of the angles between the daughter branches of the bifurcation focusing on the outer walls of the bifurcations where atherosclerotic plaques are commonly found.[62,157] We also explore the effect of angles focusing attention at the apex region where aneurysms typically are found. The two dimensional studies of sharp corner effect on flows showed that aphysical values of pressure and shear stress are obtained in sharp corner models.[60,61,72,91,104] We use rounded corners in the bifurcation models and study the effect of radius of curvature at the apex.

Our second hypothesis is that endothelial cells lining on the innermost layer of the vessel walls exposed to the wall shear stress found at the apex play a significant role in the development of aneurysms. The role of endothelial cells on arterial diseases such as atherosclerosis have been debated by many authors.[2,8,129] Numerous researchers reported that altered shear stress field can damage the endothelial cells and cause intercellular reorganization.[1,2,4] Mechanical shear force locally changes ion channel activation,[7,11] cell turnover rate[15] and cell orientation in flow direction.[2,5,7] The local changes may lead to global alterations such as vasoregulation.[36] It has been hypothesized that these morphological and functional changes of the endothelium can be responsible for the initiation of arterial diseases. However, the specific mechanisms responsible for the development of the diseases are still not clearly understood.

The response of the endothelial cells under physiological loading conditions has been investigated in *in vitro* environments. Many *in vitro* devices have been developed to test the response of the endothelial cells to shear stress. The devices include parallel plate flow chambers, capillary tubes, parallel circular disk flow chambers and cone–and–plate viscometers. In many studies, these chambers have been employed to investigate the response of

the cells exposed to shear stress fields similar to those found on the walls of a straight artery[7,15,17,39,40] and on the outer walls of a bifurcating artery.[2,14] The wall shear stress fields on the walls of straight arteries are homogeneous while inhomogeneous shear stress fields are found on the outer walls of the bifurcations. Some flow devices include a step to investigate the cell response to inhomogeneous shear stress fields arising from flow recirculation.[2,14] These chambers have been designed to elucidate the mechanisms responsible for the initiation of atherosclerotic disease. The values of shear stress found on the walls near the apex of the arterial bifurcation are not homogeneous and are not recirculating. For this reason, a novel flow chamber must be designed for the purpose of studying cell response to shear stress found in the region near the arterial bifurcation. We found that a T-shaped flow chamber is an appropriate model for this study and designed the chamber for the investigation of the cells exposed to the shear stress found at the apex of the bifurcation.

The main design criteria for parallel plate flow chambers are related to obtaining a homogeneous shear stress field. In order to produce a required magnitude of wall shear stress, the two dimensional analytical solution for the fully developed flow between two infinite parallel plates have been used for the parallel plate devices. The solution relates the corresponding wall shear stress to a given flow rate. However, the wall shear stress from the analytical solution does not occupy the entire bottom plate of the chamber due to viscous effects near the lateral walls and inertial effects near the inlet region. Many authors have recognized the inertial effects in the inlet region and estimated the region where they are significant using boundary layer theory.[52] The boundary layer theory is based on a uniform and unidirectional inlet velocity profile and high Reynolds number. The typical flow chamber experiments run for lower Re than the Re necessary for boundary layer theory. Furthermore, the inlet velocity profile found in the inlet region of the chambers are uniform and unidirectional, rather than three dimensional. As a result, the boundary layer theory is not accurate in estimating the inertial effects in typical flow chambers.

Since the importance of cell-to-cell communication has been reported by a number of researchers,[31,44–47] a test region for the cells should be defined with care. Moreover, our T-shaped flow chamber must produce wall shear stress fields similar to those found in arterial bifurcations. For this reasons, we need to quantify the flow in the T-shaped flow chamber to confine the cells in the region of "well defined flow" which satisfies our cell test condition. Avoiding the rough estimates inherent in boundary layer theory, both an analytical and numerical analyses are made to determine a region where the wall shear stress is within a chosen percentage of the two dimensional values. The qualitative and quantitative comparison between the shear stress characteristics near the T-junction of the T-shaped flow chamber and near the arterial bifurcation is made by a numerical approach. In addition, the inertial and viscous effects for the T-shaped chamber are quantified using both analytical and numerical approaches. These results are then used to develop a novel T-shaped flow chamber which can be used to expose endothelial cells to shear stress fields found at arterial bifurcations along with shear stress fields found at the walls of straight arteries. Therefore, the chamber is designed with two categories of test regions : one at the bifurcation of chamber and the other downstream of the bifurcation where the flow is nearly fully developed. This second category of flow regime is the same as that generated in a parallel plate flow chamber and will be used as a control. Because many biological assays only provide relative data, a flow chamber with a built in control such as the chamber will be very valuable.

As our final work, a mathematical model to describe periodic motions of vessel wall is proposed. In most analyses of the motion of vessel walls, a stress-free body is represented as a reference configuration and the inflation due to pressure as a load is applied to the body to describe the motion of the walls.[107,108,114] In general, *in vivo* blood vessels are axially stretched.[114,116,120,125,144] For example, when an *in vivo* blood vessel is cut in cross-section, the vessel axially shrinks in length. Hence, we include this axial extension in developing the equations of motion of blood vessel. Furthermore, *in vivo* arteries are preloaded by the systemic pressure (100 $mmHg$). The deformation of arterial walls due to pulsatility is re-

ported to be small compared with these large deformations, which result from prestretching and inflation by the systemic pressure in vessel walls.[109,110,114] Based on that, approximate solutions to the exact theory can be obtained using small on large theory. In this theory, small deformations are superposed on a known finite deformation of a compressible or incompressible homogeneous elastic body.[115] Using this theory, the periodic motions of vessel wall can be modeled as small inflation and compression due to pulsatile pressure superposed on finite axial extension and inflation.

Vessel prestretch is included in experiment studies of the canine descending aorta and a pressure radius curve obtained.[114] The curve shows that at a higher pressure level, the vessel wall becomes stiffer. This feature is believed to be due to the recruitment of collagen fibers.[112,114] M.R. Roach and A.C. Burton separated the roles of elastin and collagen fibers and reported that the recruitment of collagen fibers at a certain level of pressure is responsible for the stiffness of the arterial walls.[112] Recently, the roles of elastin and collagen fibers were quantified using a multi-mechanism theory without considering the prestretch.[141–143] In this theory, a new constitutive relation is introduced to account for the recruitment of collagen fibers. We use the muti-mechanism theory to separate the roles of elastin and collagen fibers and find the material constants, fitting the pressure–radius curve given in.[114] We then use these material constants to describe the periodic motions of a vessel wall using the equations developed by the small on large theory combined with the multi-mechanisms.

The modeling of the periodic motions of arterial walls has been performed by many authors.[140,145,146,150,151] Some authors did not account for prestretch or the base pressure[145,150,151] while, some authors included the effects of these preloadings using a membrane theory.[147] However, in this work, no constitutive equation is used for the large deformation region. Instead, both the stresses and strains of the large deformation must be known apriori. This limit the usefulness of this approach. The novelty of this study is to (i) employ a nonlinear constitutive equation for the large deformation region, (ii) develop

governing equations for the wall motion using a small on large theory and (iii) include the separate roles of elastin and collagen fibers in modeling vessel walls. The elastin fibers in arterial walls are degraded due to development, aging or diseases of arteries.[141,152,153] The quantification of the separate roles of elastin and collagen fibers using the multi-mechanism theory will therefore be useful to investigate the motions of aged and diseased arterial walls.

2.0 THE RELATIONSHIP BETWEEN BIFURCATION GEOMETRY AND HEMODYNAMIC STRESS IN MODEL OF CEREBRAL ARTERIAL BIFURCATIONS

2.1 Objectives

Cerebral aneurysms have a great propensity to initiate and develop at apecies of bifurcations.[71,79–81] Many researchers have hypothesized that hemodynamic forces are strongly related to the development of aneurysms at the apex region.[68–71,73,75–78,103] However specific mechanisms responsible for their formation, development and rupture still remain unknown. The flow field in the vasculature is determined by its geometry for a given flow rate and therefore, there may exist key geometric features related to the development of aneurysms. If so, these "geometric risk factors" would enable us to screen for patients who are predisposed to the formation of aneurysms and to perform a computational analysis in a more efficient way. Computational models including these key geometric risk factors would be more effective than models considering detailed individual geometric features of each patient's vasculature.

Great attention has been paid to investigating the role of hemodynamics in atherosclerosis in a number of numerical and experimental studies on bifurcations.[62,64,83,84,86,88,150,157] Atherosclerotic plaques have a tendency to accumulate on outer walls of daughter branches where recirculation and lowered wall shear stress are found.[3,20,82] The plaques are not typically found in the neighborhood of apecies of bifurcations. On the other hand, cerebral aneurysms are almost always found at apecies of bifurcations.[71,79–81] Therefore the regions of apecies of bifurcations have not been the focus of the studies of atherosclerosis. For example, many authors have employed computational models of bifurcations which contain sharp corners at apecies of bifurcations.[63–65] Past two dimensional analytical studies revealed that wall shear stress and pressure will be unbounded at sharp corners.[60,72,91,104] This is clearly an unphysical result. Two dimensional numerical studies captured this singularity, showing that pressure and wall shear stress become unbounded as meshes are refined at sharp corners

of bifurcation models.[61] There is no corresponding analytical work for three dimensional bifurcations. We show in Section 2.5 that in three dimensional models with sharp corners, pressure and wall shear stress are also unbounded at the apex. These singularities in pressure and wall shear stress are not found at more realistic rounded corners. Wall shear stress in rounded corner models is zero at the apex and the maximum value of the shear stress shifts away from the apex along the curve of the rounded corner. This is quantitatively different than the shear stress field in sharp corner models. It is therefore, necessary for us to design an idealized bifurcation model more carefully for studies of cerebral aneurysm initiation.

The regions of apecies of bifurcations have been widely thought to have elevated pressure and wall shear stress due to momentum transfer. Convective terms of the linear momentum equations have been thought to play an important role in pressure intensity at apecies of rounded bifurcations. One of the objectives of this work is to evaluate this hypothesis. Here, we hypothesize that Reynolds number would be a critical parameter affecting both pressure intensity and wall shear stress at apecies and explore its effect.

"Geometric risk factors" were described earlier by Friedman *et al*[62] and Perktold *et al*.[157] Their interests were focused on identifying the geometric features responsible for atherosclerotic alterations corresponding to flow divider curvatures of aortic bifurcations[62] and bifurcation angles of carotid bifurcations.[157] A second objective of this work is to identify possible "geometric risk factors" related to the formation of aneurysms. We explore effects of a bifurcation angle between two daughter branches and radius of curvature at the apecies of bifurcations.

2.2 An Idealized Model

Computational models of human cerebral bifurcated arteries for a numerical analysis were developed to investigate the "geometric risk factors" for studies of the aneurysm development. Typically, numerical models of human blood vessels are categorized by two types of models ; idealized models and reproductions of *in vivo* geometries. Three dimensional reconstructions of images from MRI or CT provide models close to real geometries. The models produced by the images are very useful for patient specific studies but disadvantageous because of large computing time and memory and difficulties in performance of parametric studies. On the other hand, idealized models require fewer computer resources and can be used in parametric studies to investigate geometric effects on flow fields. For these reasons idealized models are constructed in this study. To our knowledge, there are currently no idealized models that contain major geometric features of *in vivo* blood vessels, identified for example by.[93–96] Our aim in this research is to generate more realistic idealized models that contain all these features and can be used in parametric studies. These models are then used in the remainder of this chapter to study effects of Reynolds number, radius of curvature at apecies of bifurcations and bifurcation angles.

2.2.1 Geometric Features of Bifurcated Vessels

Attempts to obtain realistic idealized models of bifurcations are made by capturing the key geometric features commonly found in *in vivo* bifurcated vessels reported by a number of authors. A few researchers have reported that the trunk of the parent vessel widens towards the bifurcation in a typical bifurcated vessel.[93–95] The shape of cross-sectional area of the bifurcated vessel changes from relatively circular in the parent vessel to oval, to pinched oval, to a figure eight shape toward the bifurcation and then to two circles in two daughter branches.[94–96] In addition, the shape of the longitudinal perpendicular plane in the region of the bifurcation is parabolic.[97] A representative figure of a typical bifurcation

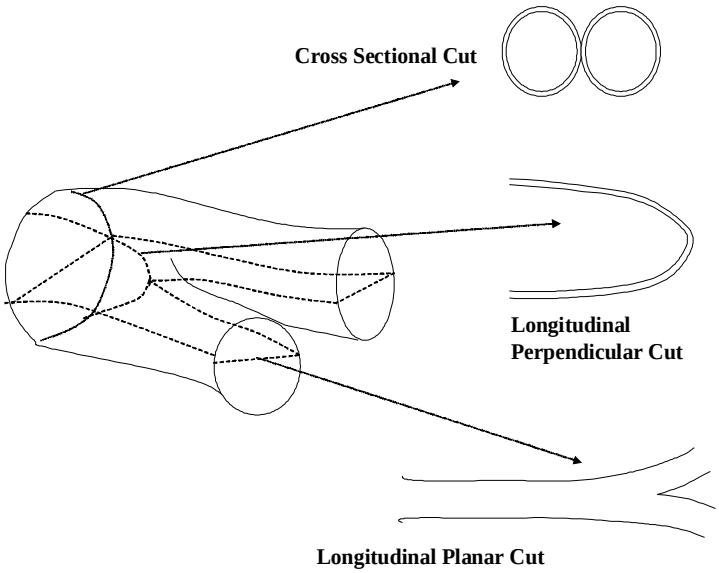

Figure 2.1. The schematic of bifurcation region of cerebral artery indicating 3 orthogonal sectioning planes by Helen M. Finlay [94].

reported by Helen M. Finlay *et al.*[94] is shown in Figure 2.1. Quantitative information on the cross sectional transition was obtained by Macfarlane *et al.*.[95,96] They evaluated the first bifurcation of the left and right anterior cerebral arteries of a 68 year old female to obtain cross sectional geometry using a technique based on the natural fluorescence of the collagen and elastin in the arterial wall.[95] A large number of cerebral bifurcations were analyzed by this methodology. The following significant geometric features on bifurcated vessels were found in all vessels studied.

1. An almost linear increase in cross sectional area with distance upstream from the apex of the bifurcation was found. Macfarlane reported that the ratio of cross sectional area of parent vessel divided by the distance from the apex (the slope of this line) ranged from -.7 mm to -2.3 mm.[95]

2. It was reported that the cross sectional area of the parent vessel increases from the constant cross sectional region to the apex of the bifurcation as 50% and 60% for the

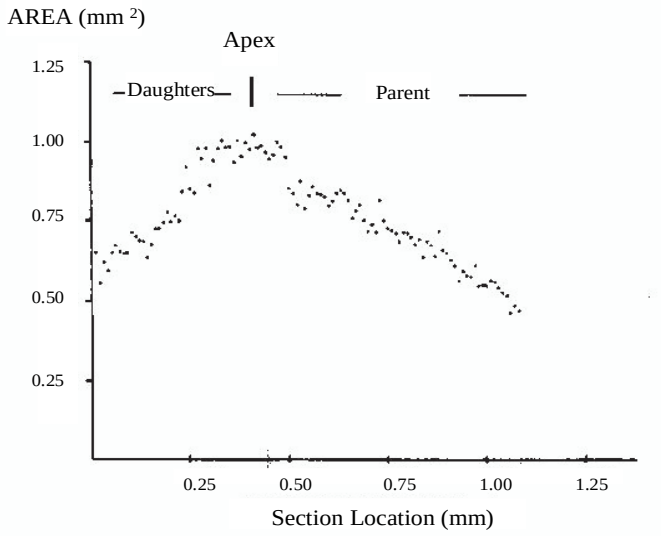

Figure 2.2. Geometric data of human cerebral arterial bifurcations from Macfarlane [95].

left and right ACA of a 68 year old woman[95] and 76.9% – 111% for the larger sample size of cerebral arteries considered in.[96]

3. Macfarlane *et al*. found that an increase along the axis formed by the intersection of the longitudinal planar and cross sectional planes is most likely the main source of increase of the cross sectional area of the parent vessel.[95,96]

Figure 2.2 demonstrates that the cross-sectional area of the parent trunk increases with distance downstream from the inlet region of the parent vessel and then approaches the maximum value at the apex of the bifurcation along a centerline of the vessel.

Past numerical studies on bifurcated vessels were mainly devoted to finding hemodynamic causes for accumulation of atherosclerotic plaques as discussed earlier. The plaques are mostly found at the outer walls of the daughter branches of bifurcations. Therefore little attention has been paid to the neighborhood of apecies of bifurcations and often erroneous geometrical models which included sharp corners at apecies of bifurcations were used.[63–65]

A few authors investigated the effect of sharp corners on stress field analytically and numerically.[60,61,72,91,104] Analytical studies on steady and two dimensional Stokes flow of an incompressible and Newtonian fluid past a wedge showed that the stress tensor is singular at the corner of the wedge.[72] Analytical solutions even for non-zero Reynolds number showed that wall shear stress and pressure will be unbounded at the sharp corner, regardless of surrounding geometry.[60,91,104] Two dimensional numerical study of a bifurcated vessel by Haljasima *et al.* revealed that pressure and wall shear stress at the sharp corner are unbounded.[61] Models which include the sharp corners are inappropriate in studies of aneurysms. Therefore, in this work, in addition to reproducing the geometric features in the idealized models, we will use rounded corners.

2.2.2 Numerical Models

Two types of geometries are employed for current parametric studies ; a model with curved daughter branches ("curved model") for studying the effect of Reynolds number and radius of curvature at the bifurcation and a model with straight daughter branches ("straight model") for studying the effect of bifurcation angles. All models are created by using a software package, Pro Engineer which is compatible with a fluid solver, ADINA for analysis [1]. The dimensions of the models are based on data provided by Macfarlane *et al.*.[95,96]

The main step in developing our models in Pro Engineer is to first create one half of the bifurcation geometry and then mirror it about a central plane. A primitive half model is composed of a trajectory along which the cross section of the model is changing. The trajectory forms the outside edge of the cross section to create for example, a circle. Cross sections are defined at specific points on the trajectory. A body is then generated by creating the blend between the cross sections. The key geometric features such as the widening of the parent trunk and the "pinching off" effect discussed in Section 2.2.1 are captured by

[1] Jill Cochran, a former undergraduate student, created these models

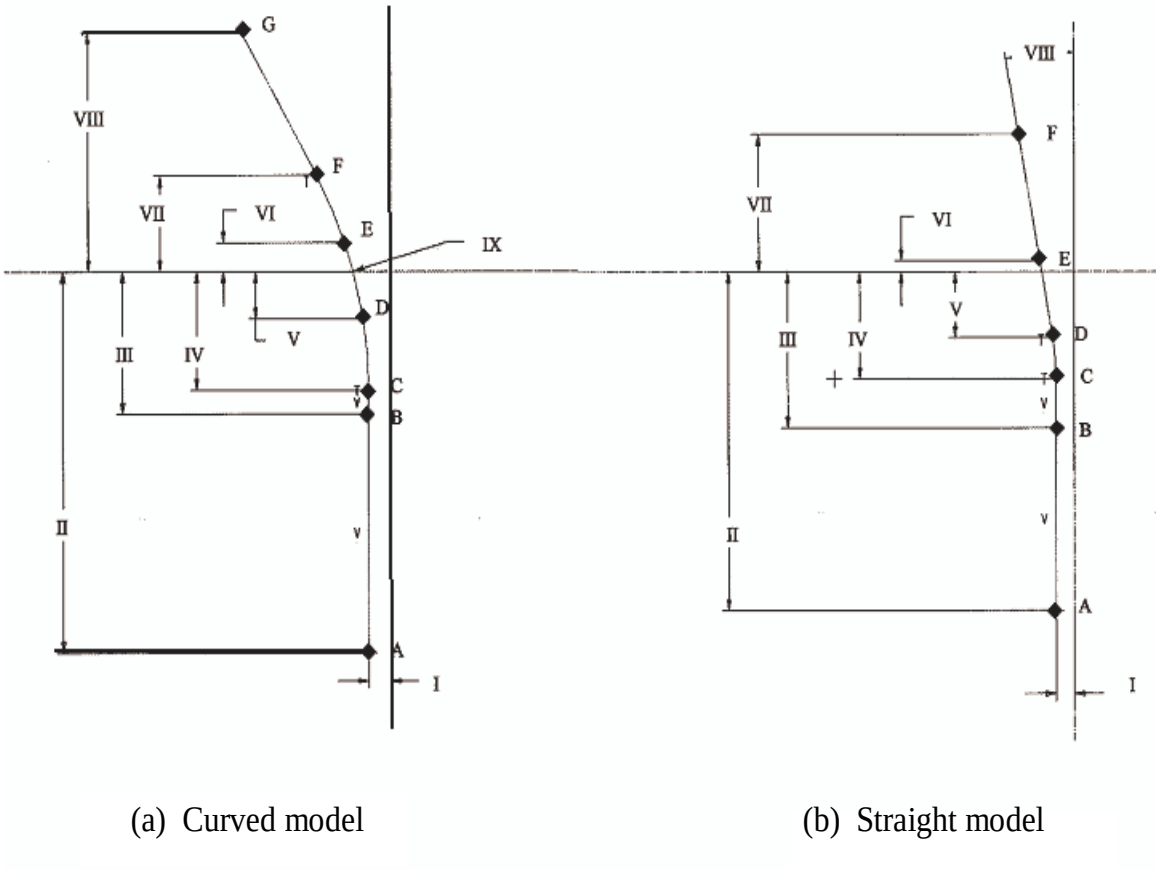

(a) Curved model (b) Straight model

Figure 2.3. Representative Pro Engineer drawings of the bifurcation model.

controlling the trajectories and the changing cross sections. In addition, the sharp corners at the bifurcations that arise when joining two daughter branches can be smoothed by a rounding technique. Detailed description for both curved and straight models are presented below.

2.2.2.1 Curved Model.

The curved model consists of two shorter straight segments connected by a large curved segment as can be seen in Figure 2.3 (a). As shown in the figure, seven points are used to define the trajectory of the curved model. The segments from point A to point C are straight, from C to F are curved with a single radius, and from F to G are straight. Cross

Table 2.1. Cross sectional geometry at labeled points in curved model .

Point/Segment	Cross-section
A	Circle-Parent
A-B	Circle-Parent
B	Circle-Parent
B-C	Transition-Circle-Oval
C	Transition-Circle-Oval
C-D	Transition-Circle-Oval
D	Oval
D-E	Transition-Oval-Circle
E	Circle-Daughter
E-F	Circle-Daughter
F	Circle-Daughter
F-G	Circle-Daughter
G	Circle-Daughter

sections are defined at points A, B, D, E, and G. The cross sections of A and B are circular with the diameter of the parent vessel. The cross section of D is oval at the bifurcation point. The cross sections of E and G are circles with the diameter of the daughter branch. A transition in cross section occurs from point B to point D (circle to oval), and from point D to point E (oval to circle). Table 2.1 shows cross sectional geometry at labeled points in the curved model. These features can be easily seen in Figure 2.4. Figure 2.5 represents a curved model created by this method to study the effect of Reynolds number and radius of curvature at the bifurcation.

2.2.2.2 Straight Model.

The straight model is composed of two long straight segments and a shorter curved segment as shown in Figure 2.3 (b). Six points define the trajectory of this model. The segment from point A to point C is straight, from point C and D is a curve of a single radius, and from point D to F is straight. Cross sections are defined at points A, B, D, E, and F. The cross sections of A and B are circles with the diameter of the parent branch. The cross

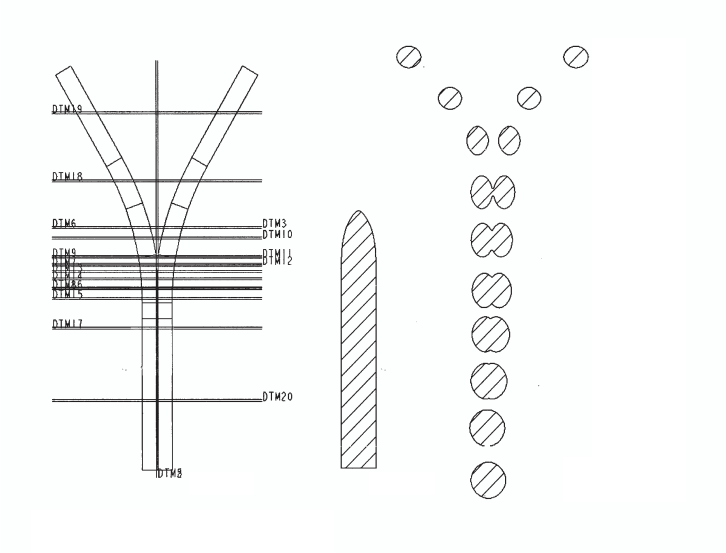

(a) longitudinal planar (b) longitudinal perpendicular (c) cross sectional

Figure 2.4. Orthogonal sections from a representative curved model.

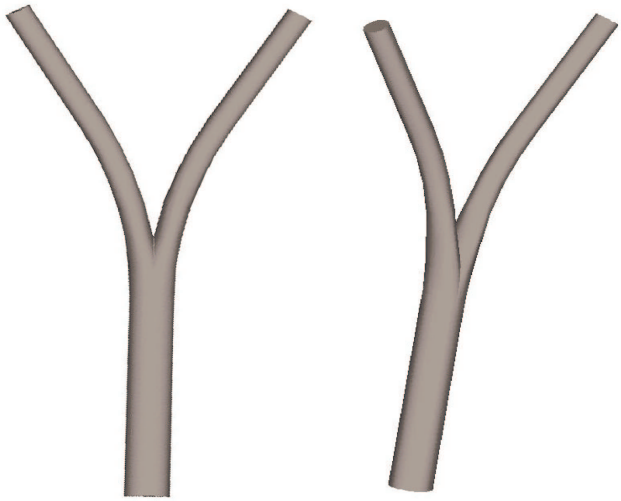

Figure 2.5. Curved bifurcation model with 20^o bifurcation angle.

Table 2.2. Cross sectional geometry at labeled points in straight model .

Point/Segment	Cross-section
A	Circle-Parent
A-B	Circle-Parent
B	Circle-Parent
B-C	Transition-Circle-Oval
C	Transition-Circle-Oval
C-D	Transition-Circle-Oval
D	Oval
D-E	Transition-Oval-Circle
E	Circle-Daughter
E-F	Circle-Daughter
F	Circle-Daughter

section of D is oval at the bifurcation point and the cross sections of points E and F are circles with the diameter of the daughter branch. The transition in cross section is found between points B and D (circle to oval), and between points D and E (oval to circle). Cross sectional geometry at labeled points in this model can be seen in Table 2.2. Orthogonal sections from a representative straight model are shown in Figure 2.6. Using this technique, we develop three straight models with bifurcation angles, β of 20^o, 40^o and 60^o to study the effect of bifurcation angles as shown in Figures 2.7, 2.8 and 2.9.

From the geometric data of arterial bifurcations from Macfarlane[95] (see Figure 2.2), the ratio of the area of two daughter branches to the area of a parent vessel is about the same. Based on this, the ratio of the diameters of two daughter branches to the diameter of a parent vessel is chosen to be 0.6. Distance between the apex and the inlet is 13.95 times larger than the radius of the parent vessel. We choose the sufficiently large distance to obtain a fully developed flow region at the inlet so that the result are unchanged with further increasing the length of the parent branch. Because data of the radius of curvature at the apex region is not available, the radius of curvature at the bifurcations of the models is explored over a range of curvatures of 0.065, 0.080 and 0.100 times the radius of the parent vessel.

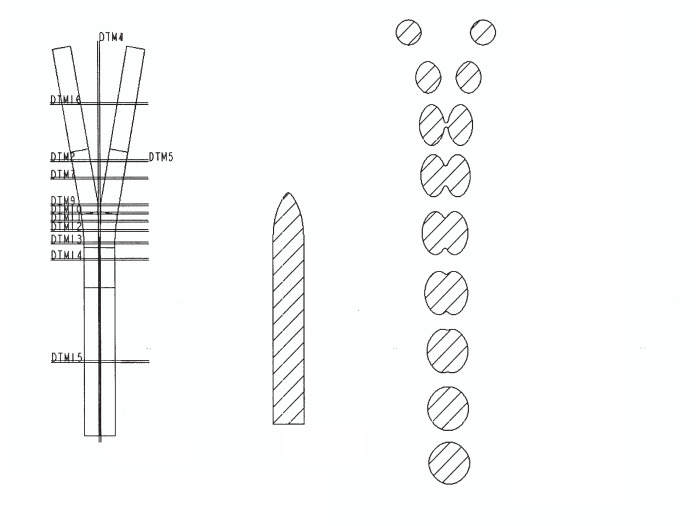

(a) longitudinal planar (b) longitudinal perpendicular (c) cross sectional

Figure 2.6. Orthogonal sections from a representative straight model.

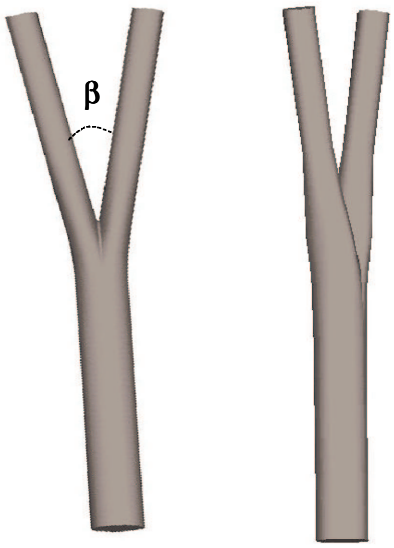

Figure 2.7. Straight bifurcation model with 20^o bifurcation angle.

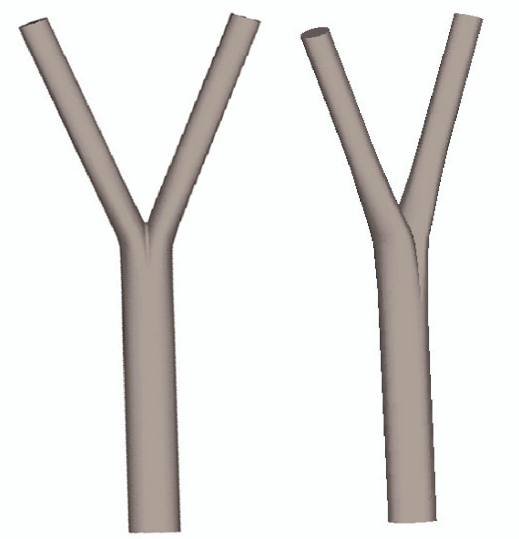

Figure 2.8. Straight bifurcation model with 40^o bifurcation angle.

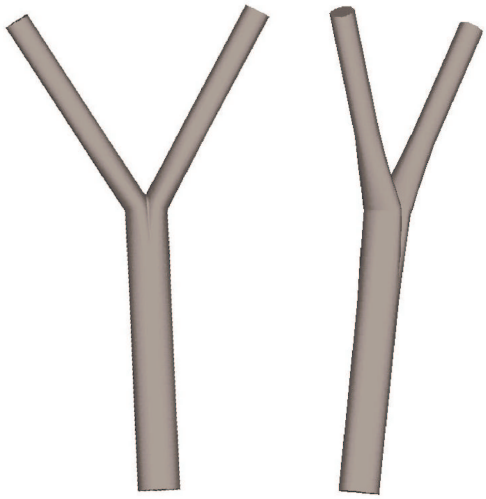

Figure 2.9. Straight bifurcation model with 60^o bifurcation angle.

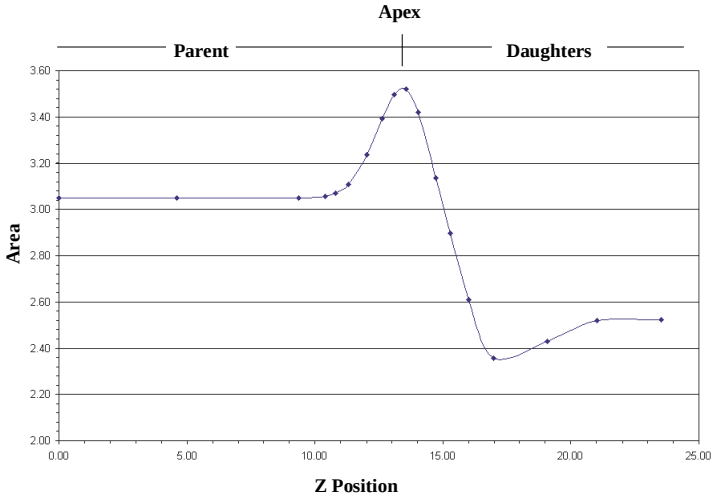

Figure 2.10. Cross-sectional area as a function of distance from the inlet.

2.2.3 Validation

All the models created by Pro Engineer successfully include the significant geometric features reported in[93–95, 97] and discussed in Section 2.2.1. Their orthogonal sections from the representative models agree well with the geometric features provided by[93–95, 97] (see figure 2.4, 2.6). The figures show that the shape of cross-sectional area of the bifurcation is circular in a parent vessel and it becomes a oval and transitions smoothly to a figure eight shape until it pinches off into two daughter branches. In addition, the shape of the boundary of the bifurcation in the longitudinal perpendicular plane is parabolic. Shown in Figure 2.10 is a plot of the cross sectional area versus the distance from the inlet. The cross sectional area displays an approximately linear increase (taper : 0.224) before the bifurcation and a linear decrease (taper : -0.363) afterward. This feature is qualitatively in accord with the features provided by Macfarlane *et al.*. Finally, as can be seen in Figure 2.11, all junctions joined by the parent and two daughter branches are smoothed. In particular, round corners at the apecies of the bifurcation models are generated to eliminate the sharp corners for physical relevance.

Figure 2.11. Enlarged view of round corner at the apex of the bifurcation.

2.3 Governing Equations and Non-dimensionalization

The fluid is modeled as incompressible, homogenous and linearly viscous and the flow as steady. Therefore, the motion of the fluid is governed by the following equations referred to rectangular Cartesian coordinates, x_i,

$$v_{i,i} = 0, \tag{2.1}$$

$$\rho v_{i,j} v_j = T_{ij,j}, \tag{2.2}$$

$$T_{ij} = -p\delta_{ij} + \mu(v_{i,j} + v_{j,i}), \tag{2.3}$$

where v_i are the components of velocity vector, ρ is the fluid density, μ is the fluid dynamic viscosity, T_{ij} are the components of the Cauchy stress tensor, the notation $(), i$ denotes $\partial()/\partial x_i$. Equations 2.1 and 2.2 represent the incompressibility and linear momentum equations, respectively. The assumption of steady flow in cerebral arterial bifurcations is motivated by the fact that the value of Womersley parameter is small for unsteady flow in cerebral arteries. For unsteady, fully developed flow driven by an oscillatory pressure gradient in a straight pipe with circular cross section, the value of Womersley parameter range from 1.3 to 2.7 for the cerebral arteries with $2 \sim 4$ mm diameters. Hence, we can consider

Table 2.3. Models for parametric studies .

Model	Radius of Curvature (R_c)	Angle (β)	Parametric Studies
A curved model	0.065, 0.08, 0.1	20^o	Re, R_c
A straight model	0.1	$20^o, 40^o, 60^o$	Angle of daughter branches relative to parent branch

the flow in cerebral arteries with $2 \sim 4$ mm diameters as quasi-steady.

Non-dimensional variables are defined as

$$\bar{x}_i = \frac{x_i}{D}, \quad \bar{v}_i = \frac{v_i}{U}, \quad \bar{p} = \frac{(p - p_{in})D}{2\mu U}, \tag{2.4}$$

where D is the diameter of the parent vessel, U is the average velocity at the inlet of the parent vessel, p_{in} is the pressure at the inlet of the parent vessel. The dimensionless parameter used in this study is the Reynolds number defined as

$$Re = \frac{\rho U D}{\mu}. \tag{2.5}$$

The Reynolds number is used as one of the parameters for the parametric studies.

Based on the definition of Re, we plan to perform the parametric studies using the curved and straight models as shown in Table 2.3.

2.4 Numerical Formulation

2.4.1 Boundary Conditions

Due to geometric symmetry, half models are used for calculating flow fields in the bifurcation models. The half models significantly diminish the amount of work for mesh generation

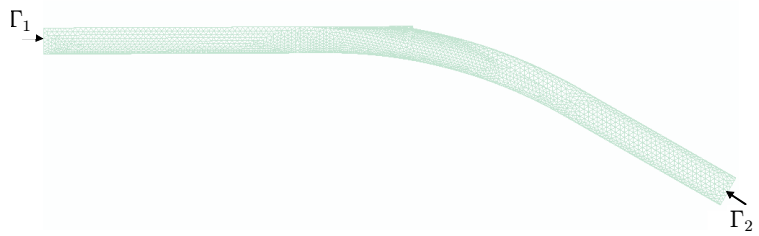

Figure 2.12. Representative meshed bifurcation with inlet, Γ_1 and outlet, Γ_2.

and computing time. Figure 2.12 shows a representative meshed bifurcated model. The fluid enters at inlet Γ_1 and exits at outlet Γ_2.

The Cauchy stress tensor, T_{ij} in the linear momentum equations 2.2 can be expressed in the either physical or mathematical formulation since the difference between the stress tensors in both formulations is divergence free. A modified stress tensor, T'_{ij} is used in the mathematical formulation. It has no transposed term of velocity gradient as expressed in Equation 2.6.

$$T'_{ij} = -p\delta_{ij} + \mu v_{i,j}. \tag{2.6}$$

Note that the equation of linear momentum has a similar form for both formulations as

$$\rho v_{i,j} v_j = T_{ij,j} = T'_{ij,j}. \tag{2.7}$$

The stress tensor, T'_{ij} in the mathematical formulation is considered for the purpose of inlet

and outlet boundary conditions. Then the following boundary conditions are applied ;

$$t'_i = T'_{ij} n_j = \left(\mu \frac{\partial v_i}{\partial x_j} n_j - p n_i) \right) |_{\Gamma_\alpha} = C_\alpha n_i \qquad \text{for } \alpha = 1, 2, \tag{2.8}$$

$$\varepsilon_{ijk} t'_j n_k = 0, \quad \text{on symmetry plane} \tag{2.9}$$

where n_i are components of the outward normal to the surface and C_α is a prescribed constant. The modified traction vector, t'_i is specified to be constants at the inlet, Γ_1 and the outlet, Γ_2 (see Equation 2.8). Imposing 2.8 at the boundaries is consistent with fully developed flow conditions (Pouisseulle flow). For this work, C_1 is chosen to be zero at Γ_1 and C_2 is chosen to obtain a required range of the Reynolds number based on the inlet diameter at Γ_2. On the symmetry plane, the perfect slip condition is specified and no slip conditions are applied on the surrounding walls of the bifurcation models.

Evaluation of the applicability of the mathematical traction as a numerical boundary condition for flow in a straight pipe of circular cross section is given in Section 2.5. The detailed explanation of this boundary condition is discussed in[66] for the numerical aspects and[57,58] for the mathematical aspects.

2.4.2 Solution Methods

The governing equations, 2.1 and 2.2 are solved by utilizing the commercial software package ADINA, version 7.5 (Automatic Dynamic Incremental Nonlinear Analysis, Watertown, MA) based on a finite element method. Bodies created in Pro-Engineer software are imported into ADINA fluid solver and meshed entirely by employing free-form mesh (irregular meshes) generating four-node tetrahedral elements. Meshes are refined in the bifurcation region where high pressure gradients are expected.

The tetrahedral elements have a linear interpolation function, which is called "a shape function" for pressure and a bubble function for the velocities.[66] A finite volume approach of upwinding is used to overcome numerical instabilities at high Reynolds numbers.[66] The steady, incompressible Navier Stokes equations with the boundary conditions described in Sections 2.3 and 2.4.1 are solved by a sparse solver based on the Gauss elimination method. The sparse solver solves a system of linear algebraic equations. The Newton-Raphson iterative scheme is used to solve the nonlinear finite element equations.[66] The convergence criterion for the major iteration is as follows. The major iteration loop is Newton-Raphson iteration and the iterate is stopped if the following condition is satisfied.

$$\frac{|| X^i - X^{i-1} ||}{|| X^i ||} \leq RTOL, \tag{2.10}$$

where $RTOL$ is a chosen tolerance. X^i denotes the solution vector for the velocity and pressure at iteration i and $|| X ||$ is the Euclidean vector norm defined as

$$|| X ||= (\sum_j | x_j |^2)^{1/2}, \tag{2.11}$$

with the x_j being the components of the vector X. Therefore the norms (magnitude) of the difference between velocity and pressure from previous iteration and those from current iteration are used for the convergence criterion. Our calculations are stopped when the condition (2.10) with $RTOL = 0.001$ is met for both velocity and pressure.

2.4.3 Mesh Convergence

Characteristics of the pressure along centerlines of the bifurcation models are our primary concern. We determine if inertial effects cause a localized high pressure at the apecies and look for "geometric risk factors". Mesh refinement studies are conducted by refining the meshes in the bifurcation region where the steep wall shear stress and pressure gradient ex-

Table 2.4. Mesh refinement studies .

Mesh Density	E1	E2	E3	E4	E5	E6	E7
Number of Elements	47800	50000	52000	54000	56000	60000	81000

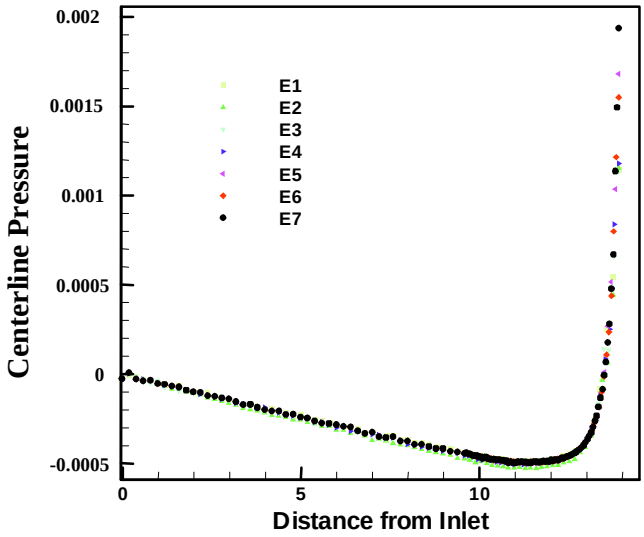

Figure 2.13. Centerline pressure (Pa) along the distance from the inlet of the model for seven different mesh densities.

ist. Meshes are refined in the bifurcated region by increasing the number of elements at that region. Table 2.4 shows the seven different mesh densities with the number of total elements generated using the curved model. The centerline pressures evaluated in all the models are presented in Figure 2.13. Comparison between the variations of centerline pressures of E6 and E7 mesh densities shows that pressure differences between the two models are within 0.5 % range along the centerlines. Numerical bifurcation models for the parametric studies are then based on the E7 mesh density.

2.5 Results (Re, Radius of curvature, bifurcation angle)

As discussed earlier, the mathematical traction is specified at the inlet and outlet boundaries of the half model. We perform a numerical analysis on a straight cylinder using both the physical and mathematical tractions to evaluate the applicability of mathematical traction as a boundary condition by employing the ADINA-F fluid solver. We compare the analytical solution for fully developed flow in a straight pipe with the numerical solutions obtained by applying the physical traction (PT) and mathematical traction (MT) boundary conditions to the inlet of the straight cylinder for the validation. For the computational analysis, uniform constant normal traction at the inlet and zero normal traction at the outlet of the straight cylinder are specified for $Re = 100$. When we assume that gravity effect is negligible, the analytical solution for steady, fully developed flow is

$$\mathbf{v} = \frac{1}{4\mu}(-\frac{dp}{dx})(\frac{D^2}{4} - r^2)\mathbf{e}_x, \tag{2.12}$$

where r and x are the radial and axial spatial variables, respectively. The magnitudes of velocities, v obtained numerically using MT and PT formulations are compared to the magnitude of velocity from the analytical solution for the same Re number. The radial distance r and v obtained numerically are normalized, dividing by the radius of the pipe, $D/2$ and maximum velocity v_{max} from the analytical solution. The results are shown in Figure 2.14 by denoting the normalized v and r as v^* and r^*, respectively. As shown in the figure, the analytical solution matches well with the axial velocity for the mathematical traction (MT) (maximum error = 1.2%). The axial velocity for the physical traction (PT) on the other hand, deviates up to 11% compared to the analytic solution. The mathematical traction is therefore chosen as a numerical boundary condition in our models.

This work focuses on applications to blood flow in the human circulatory system. The fluid for analysis is human blood. Human blood exhibits shear thinning non-Newtonian behavior at low shear rates. We used the value of the viscosity reported by C.G. Caro, which is

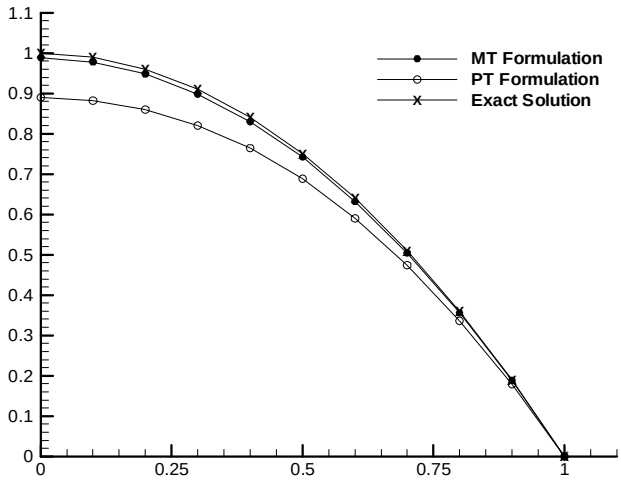

Figure 2.14. Comparison of normalized velocity profiles for exact solution, PT formulation and MT formulation at inlet.

0.0035 Ns/m^2 as the viscosity of human blood for our analysis. The density of human blood is 1050 kg/m^3. The parametric studies of the bifurcation models were carried out based on these human blood properties.

The curved model is used to study the inertial effects. Reynolds numbers are chosen to be 255, 505, 755 based on the inlet average velocity, U and the diameter of the parent vessel, D. Radius of curvature, R_c is selected to be 0.065. Pressure variation along the centerline of the model for the three cases is presented in Figures 2.15, 2.16, 2.17. As expected, elevated pressure is localized in the region of the bifurcation. The pressure values of the bifurcation region appear to be greatly altered as the Re changed. Clearer evidence supporting this is shown in Figure 2.18. The figure shows the centerline pressure along the distance from the inlet up to the apex of the bifurcation. Higher Reynolds number results in higher centerline pressure. We can also see that there exists a steep pressure gradient in the region of the bifurcation. In addition, a larger pressure gradient is found at higher Reynolds number (see a smaller box in Figure 2.18). These facts prove our hypothesis, that elevated pres-

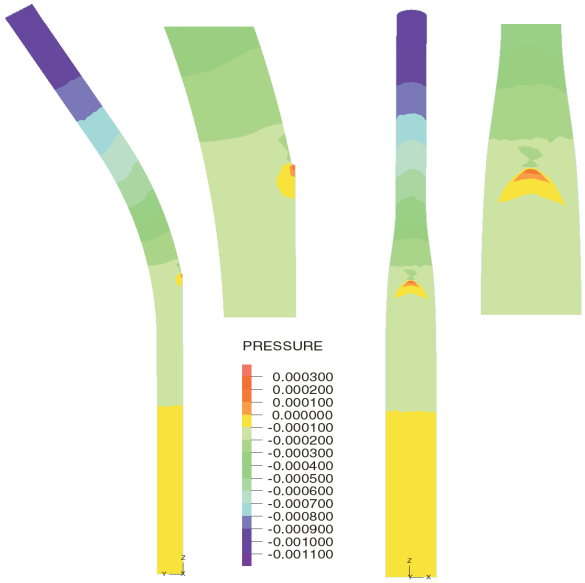

Figure 2.15. Pressure (Pa) variation in the curved model at Re = 255 and $R_c = 0.065$.

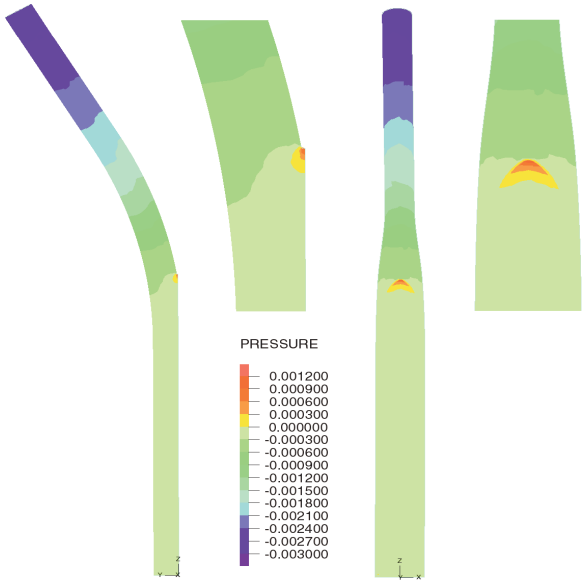

Figure 2.16. Pressure (Pa) variation in the curved model at Re = 505 and $R_c = 0.065$.

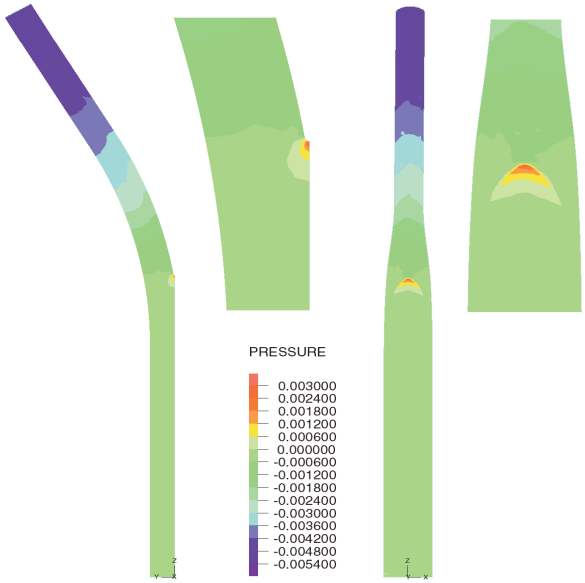

Figure 2.17. Pressure (Pa) variation in the curved model at Re = 755 and $R_c = 0.065$.

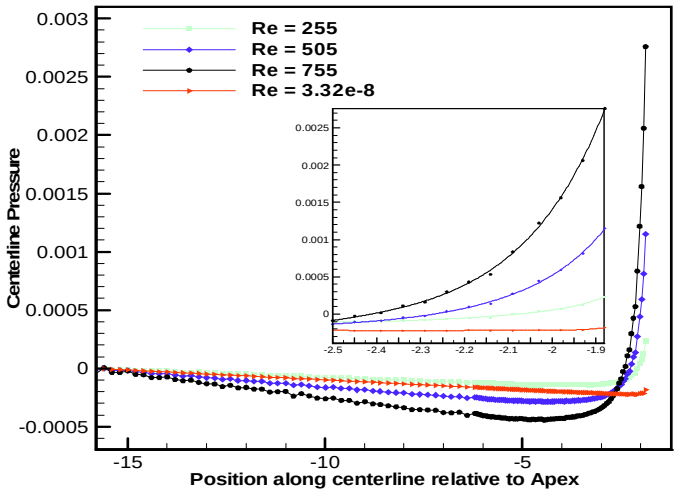

Figure 2.18. Centerline pressure (Pa) with distance downstream from the inlet to the apex in the curved model at Re = 255, 505, 755 and $R_c = 0.065$.

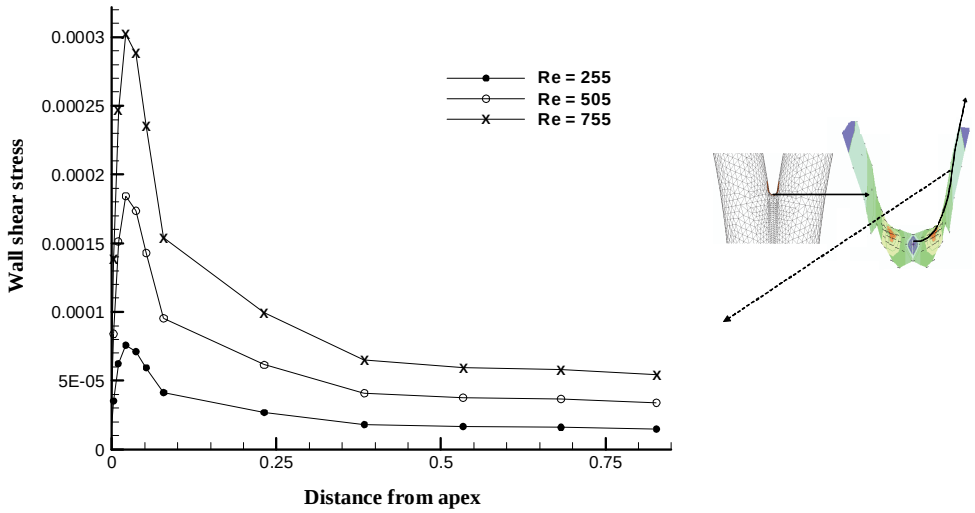

Figure 2.19. Wall shear stress (Pa) along the neck of the bifurcation in the curved model at Re = 255, 505, 755 and $R_c = 0.065$.

sure at apecies of bifurcations results from increased inertial effects. Stokes flow, in which the inertial effect is negligible, is simulated to determine whether the geometric effects can contribute to the sudden increase in the centerline pressure in the region of bifurcation for this bifurcation model ($R_c = 0.065$). The change in pressure in the bifurcation region is not significant, therefore supporting our hypothesis.

Increasing Reynolds number increases the magnitudes of wall shear stresses along the center neck of the bifurcation (see Figure 2.19). As shown in the figure, at each Re, the value of wall shear stress is found to be zero at the apex because of the geometrical symmetry and then increases along the neck of the bifurcation up to the maximum value. It then decreases to a constant value of wall shear stress found in a straight artery at a given flow rate. The overall values of these wall shear stresses increase as Re increases along the neck, concluding that increased inertial force elevates overall values of wall shear stresses at the vicinity of the apex of bifurcation.

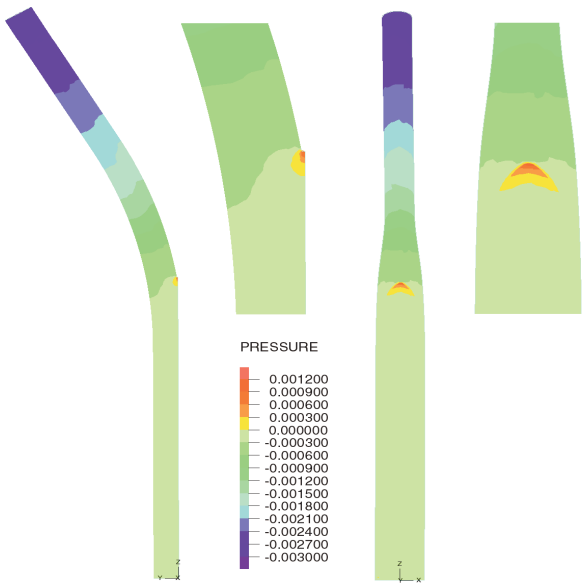

Figure 2.20. Pressure (Pa) variation in the curved model at Re = 505 and $R_c = 0.065$.

The second study is used to investigate the round corner effect that most researchers previously disregarded. Fixing the Reynolds number at 505, a sharp corner and three radius of curvature, R_c (S = sharp corner, A = 0.065, B = 0.08, C = 0.1) at the corner of the bifurcation model are used. The pressure contour plots for the three cases are shown in Figures 2.20, 2.21, 2.22. Although it is difficult to find any differences from the contour plots, the lines inside a smaller box in Figure 2.23 make clear two facts. One is that as the radius of curvature increases, the pressure decreases. The other is that the centerline pressure at the sharp corner of the bifurcation is unbounded. In our numerical studies this unboundness cannot be attained though it is more accurately modeled with increasing mesh density. As seen in Figure 2.23, the pressure at the sharp corner drops significantly. Due to the singularity at the nodal point, we see a discontinuity in the pressure curve. As stated previously, wall shear stress at a sharp corner is also unbounded as mesh is refined in the region of the apex (see Figure 2.24). The maximum wall shear stress decreases as the radius of curvature increases as shown in Figure 2.25. The unboundness of pressure and wall shear stress at a sharp corner and lowering effect of larger radius of curvature on wall shear stress in three dimensional model are compatible with the results found in two dimensional numer-

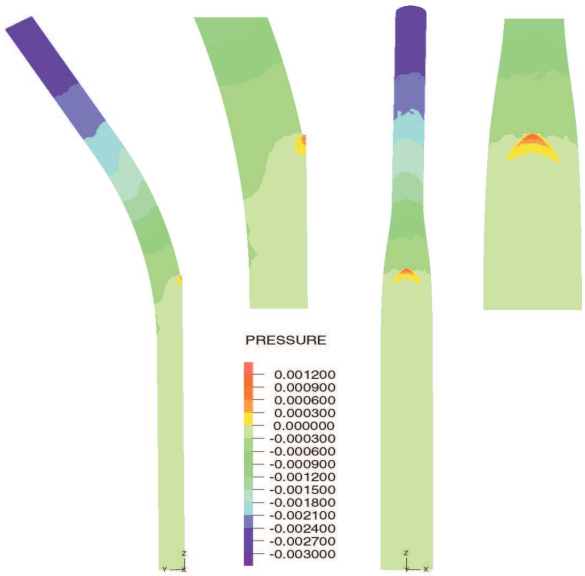

Figure 2.21. Pressure (Pa) variation in the curved model at Re = 505 and $R_c = 0.08$.

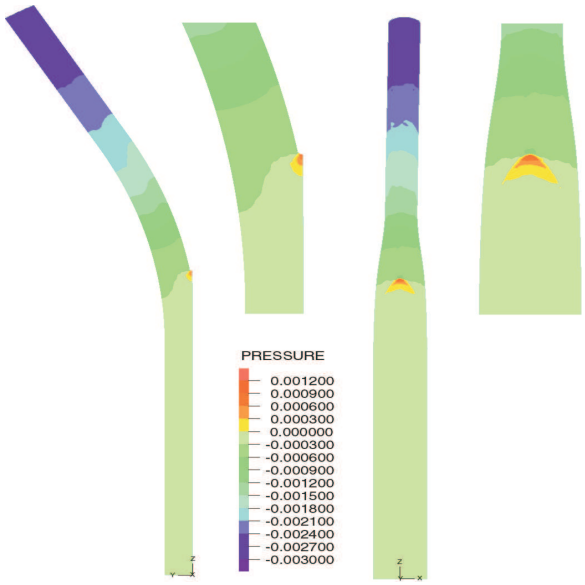

Figure 2.22. Pressure (Pa) variation in the curved model at Re = 505 and $R_c = 0.1$.

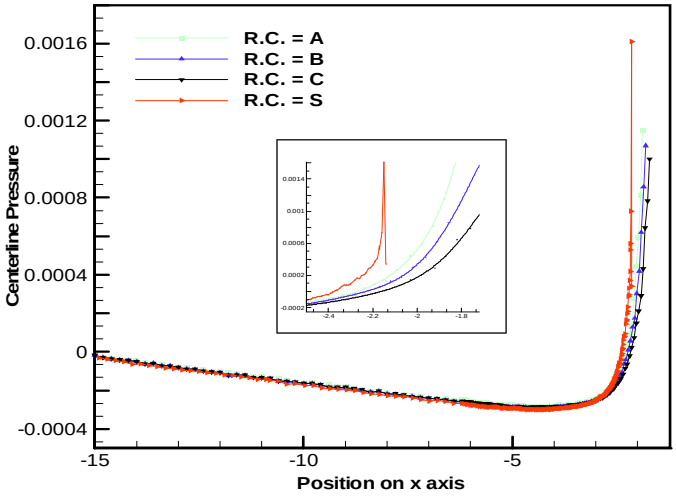

Figure 2.23. Centerline pressure (Pa) with distance downstream from the inlet to the apex in the curved model at Re = 505 and $R_c = 0.065$, 0.08 and 0.1.

ical model of bifurcation.[61] These facts reenforce the point that care should be taken in computational studies when modeling the bifurcation.

As our final parametric study, the effect of the angles between the two daughter branches using the straight model is explored. Angles are selected to be $20^o, 40^o, 60^o$ fixing the Reynolds number at 505 and radius of curvature at $R_c = 0.1$. Three representative pressure contour plots and plots of centerline pressure along the distance from the inlet for the models with three angles are presented in Figures 2.26, 2.27, 2.28 and 2.29 respectively. The effect of bifurcation angle on wall shear stress is also shown in Figure 2.30. As seen in Figures 2.29 and 2.30, there are no major differences in pressure gradients and wall shear stresses at the bifurcations, implying the effect of angle in this range on wall shear stresses and pressures at the apex is almost negligible.

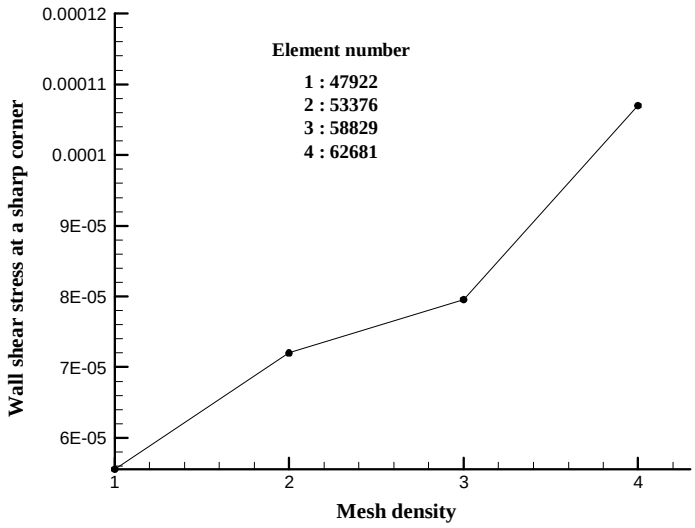

Figure 2.24. Sharp corner effect on wall shear stress.

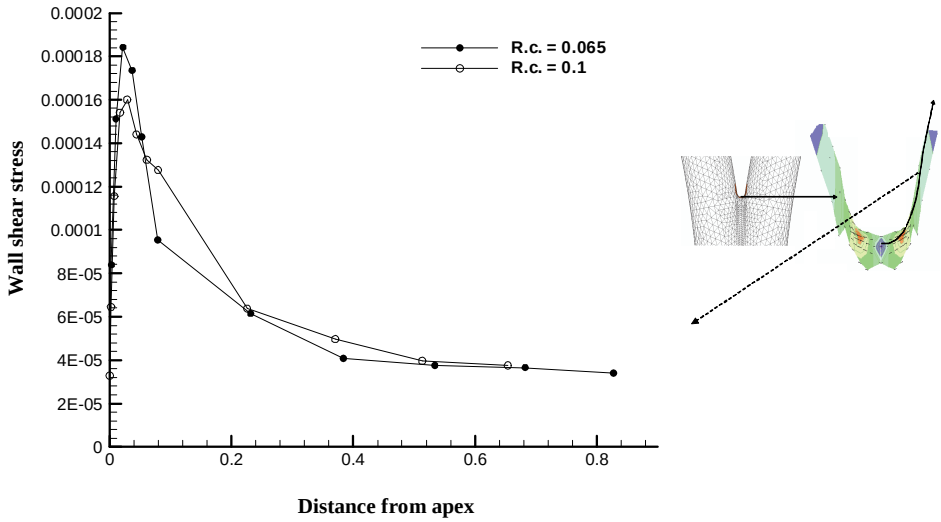

Figure 2.25. Wall shear stress (Pa) along the neck of the bifurcation in the curved model at Re = 505 and $R_c = 0.065$ and 0.1.

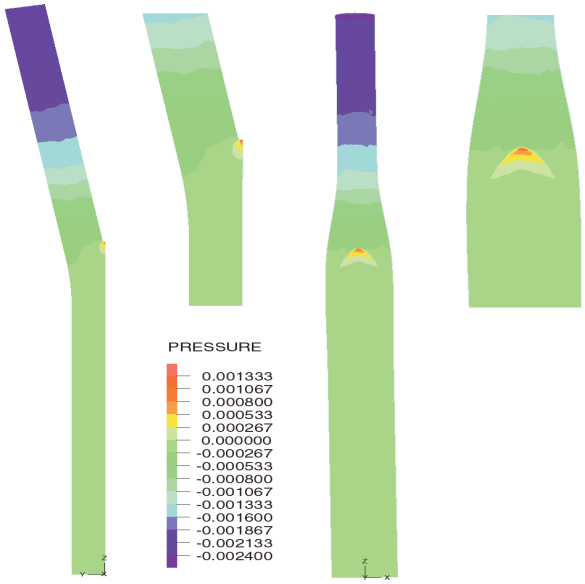

Figure 2.26. Pressure (Pa) variation in the straight model with 20^o bifurcation angle at Re = 505 and $R_c = 0.1$.

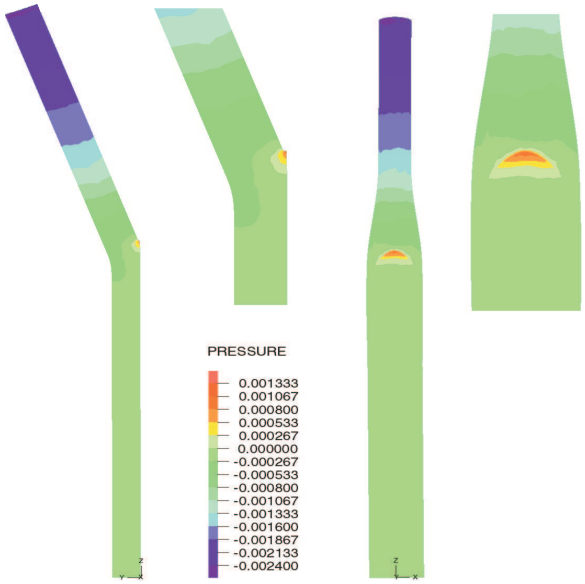

Figure 2.27. Pressure (Pa) variation in the straight model with 40^o bifurcation angle at Re = 505 and $R_c = 0.1$.

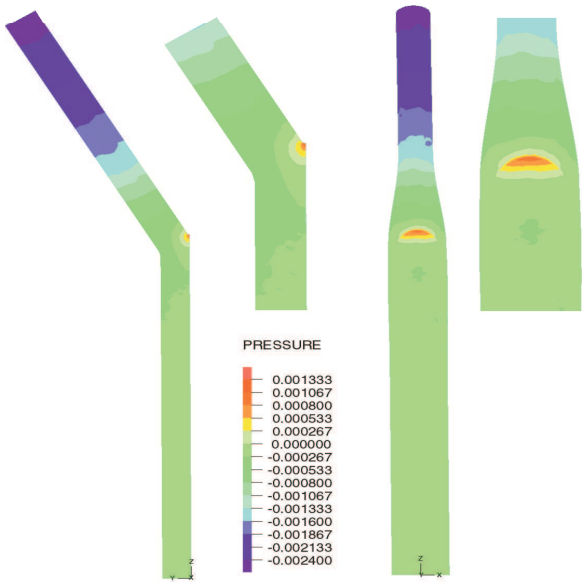

Figure 2.28. Pressure (Pa) variation in the straight model with 60^o bifurcation angle at Re = 505 and $R_c = 0.1$.

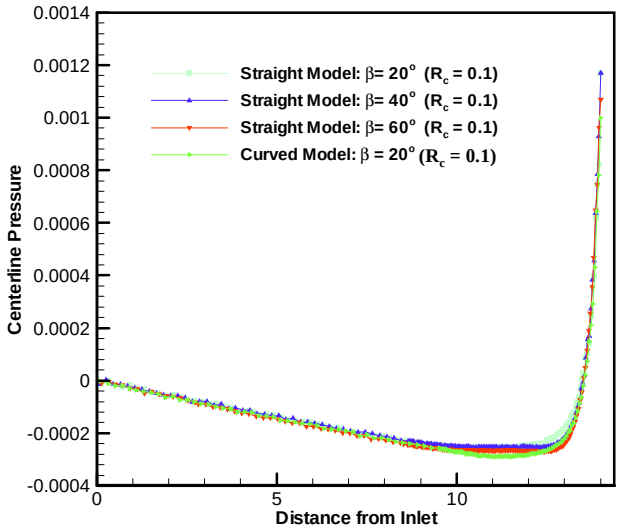

Figure 2.29. Centerline pressure (Pa) with distance downstream from the inlet to the apex in the straight models with 20^o, 40^o and 60^o bifurcation angles at Re = 505 and $R_c = 0.1$.

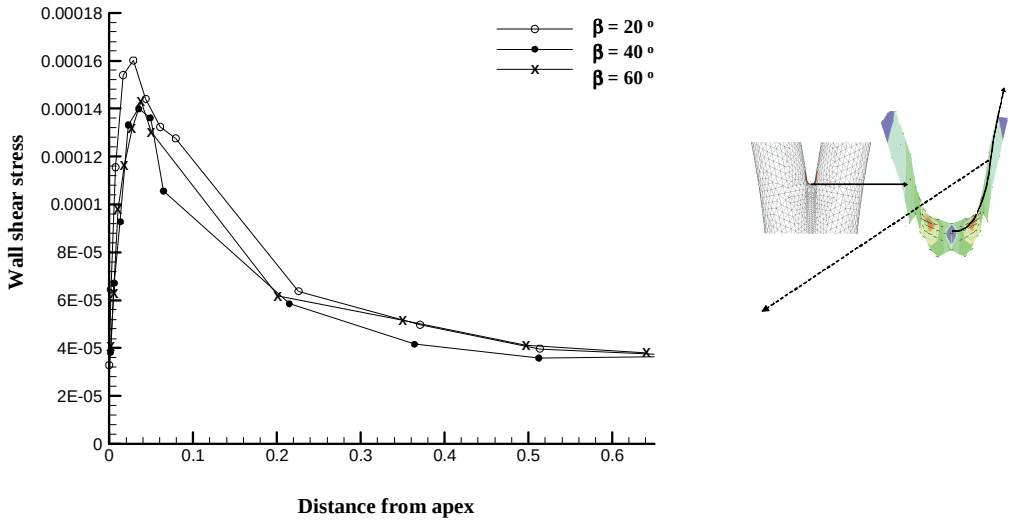

Figure 2.30. Wall shear stress (Pa) along the neck of the bifurcation in the straight models with 20^o, 40^o and 60^o bifurcation angles at Re = 505 and $R_c = 0.1$.

2.6 Discussion of Results and Future Work

In order to investigate the geometric risk factors thought to be responsible for the aneurysm formation at the bifurcation, we created the two types of idealized models ; a straight and a curved model including key geometric features found in *in vivo* bifurcated arteries. Using these geometries, the effects of Reynolds number, radius of curvature and bifurcation angle on the centerline pressure from the inlet to apex and wall shear stress at the vicinity of the apex were numerically explored.

From the Reynolds number study, we found that (i) elevated pressure gradients in the region proximal to the apex of bifurcation result from inertial force, not from geometric shape, and (ii) larger inertial force results in larger centerline pressure gradients and overall wall shear stresses at the vicinity of the apex. Bifurcation angle was found not to be an important parameter for increase of the centerline pressures and wall shear stresses. As emphasized earlier, rounding a sharp corner is found to be very important for computational studies of bifurcation geometry to find hemodynamic effects on aneurysm formation since

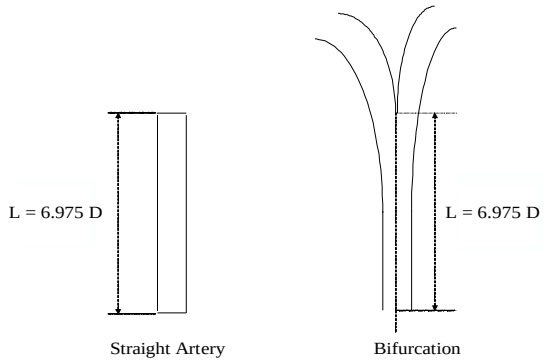

Figure 2.31. A straight artery and a bifurcation showing its length.

pressure and wall shear stress are unbounded at a sharp corner. Patient specific geometry of the apex region should be found to investigate hemodynamic effect more precisely because larger radius of curvature lowers the values of pressure gradients and wall shear stresses.

Appendix A shows detailed calculations to convert the values of pressures or wall shear stresses presented in the result section to actual values for bifurcations with 2mm and 4mm diameters using the dimensionless parameters given in Equations 2.4 and 2.5. Pressure differences from inlet to apex, ΔP found in bifurcations with 2mm, 3.2mm and 4mm diameters (curved model with $R_c = 0.065$) are then compared to those from inlet to outlet found in straight arteries with 2mm, 3.2mm and 4mm diameters for given Reynolds numbers. The length of the straight artery and the length from the apex to the inlet of the bifurcation is $6.975 \times D$ as shown in Figure 2.31. It turns out that pressure differences in bifurcations are about $1.8 \sim 6.1$ times larger than those in straight arteries for a given Re (see Table 2.5[2]). Maximum wall shear stresses found at the apex regions of bifurcations (curved model with $R_c = 0.065$) are also compared with wall shear stresses found in straight arteries for a given Re (see Table 2.6). As shown in the table, we found that the maximum wall shear stresses at the apex regions are about $14.2 \sim 17.4$ times larger than wall shear stresses found in straight arteries. Typical value of wall shear stress found at the lateral walls of straight segments

[2]*'s in the table are well outside the expected physiological region.

Table 2.5. Pressure differences found in straight arteries and bifurcations for given Reynolds numbers ($\Delta P(mmHg)$) .

	Straight artery			Bifurcation		
Re	ΔP	ΔP	ΔP	ΔP	ΔP	ΔP
	$D = 2mm$	$D = 3.2mm$	$D = 4mm$	$D = 2mm$	$D = 3.2mm$	$D = 4mm$
255	1.25	0.49	0.31	2.25	0.88	0.56
505	*	0.96	0.62	*	3.52	2.25
755	*	*	0.92	*	*	5.63

Table 2.6. Wall shear stresses found in straight arteries and at the apex regions of bifurcations for given Reynolds numbers ($\tau_w(dynes/cm^2)$) .

	Straight artery			Bifurcation		
Re	τ_w	τ_w	τ_w	τ_w	τ_w	τ_w
	$D = 2mm$	$D = 3.2mm$	$D = 4mm$	$D = 2mm$	$D = 3.2mm$	$D = 4mm$
255	53.33	20.34	13.33	757.49	295.87	189.37
505	*	45.86	26.66	*	719.13	460.25
755	*	*	40.00	*	*	755.99

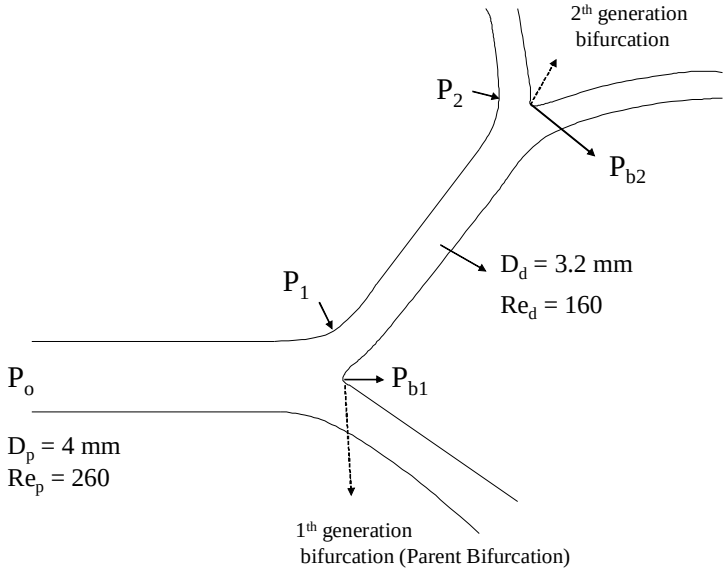

Figure 2.32. Pressures and the corresponding Re to wall shear stress 15 $dynes/cm^2$ in two generation bifurcations with the diameter D_p and D_d.

of the vascular system are commonly believed to be nearly constant and on the order of 15 $dynes/cm^2$. The supposition that the geometry of the arterial tree is such that wall shear stress is approximately constant, is also supported by the cube law analysis.[148] Recalling the relationship between Re and τ_w for a straight segment

$$Re = \frac{\rho D^2}{4\mu^2}\tau_w, \tag{2.13}$$

it is clear that for fixed blood properties and chosen vessel diameter, D, only a small range of Re will correspond to τ_w of order 15 $dynes/cm^2$. For example, it follows from Equation 2.13 that for a vessel with $D = 4mm$ the Reynolds number will be on the order of 260. To emphasize this, in Table 2.6, values which are well outside the physiological wall shear stress range are noted with a "*".

We now consider a representative section of the arterial tree containing two generations of bifurcations (see Figure 2.32). In the following discussion, wall shear stress is fixed as 15 $dynes/cm^2$. The diameter and Re of the second generation bifurcation could be estimated

by Equation 2.13 as $D_d = 3.2mm$ and $Re_d = 160$ using continuity. For the parent bifurcation with $D_p = 4mm$, Re_p is around 260 for $\tau_w = 15\ dynes/cm^2$. Since the elevation of pressure at the bifurcation is found to be a local effect and therefore, the pressure drop $(P_o - P_1)$ from the inlet of parent bifurcation to the inlet of the second generation bifurcation is nearly the same value found in a straight artery (0.31 $mmHg$ for $Re = 255$) from our numerical analysis (see for example, Figure 2.15). Then, the pressure increase $(P_{b2} - P_1)$ between the apex and the inlet of the second generation bifurcation can be estimated by extrapolating the values given in Table 2.5 for $Re = 160$ (nonlinear fit) and is found to be around 0.4 $mmHg$. Then it turns out that the total pressure increase $(P_{b2} - P_o)$ from the inlet of parent bifurcation to the apex of the second generation bifurcation is about 0.71 $mmHg$, which is slightly larger than the pressure increase $(P_{b1} - P_o)$ between the apex and the inlet of parent bifurcation $(0.56mmHg)$. This value of pressure increase is small compared to the average blood pressure $(100mmHg)$. Therefore, it is unlikely that this amount of elevation of pressure at the apex of either bifurcations will play a major role in the initiation of aneurysms. Since the spatial pressure variation at the apex is more severe (see for example, Figure 2.15), we would conclude that the spatial gradient of pressure at the apex could play a role in the aneurysm formation though to date there is physical explanation of this.

The maximum wall shear stress at the apex of the parent bifurcation ($Re = 255$) is 189.37 $dynes/cm^2$ as shown in Table 2.6. The value of wall shear stress at the apex is quite large compared to the value found in a straight artery. This high value of wall shear stress may affect the turnover rate and the viability of endothelial cells, which could be a major factor in wall degradation. Therefore, we conclude that the elevation of wall shear stress at the apex of bifurcation may be an important risk factor for the aneurysm initiation.

As for the pressure calculations, the maximum wall shear stress found at the apex of the second generation bifurcation was estimated by extrapolating the values given in Table 2.6 (linear fit). The maximum wall shear stress at the apex of the second generation bifurcation

was found to be 135 $dynes/cm^2$, which is smaller than the value found at the apex of the parent bifurcation. This demonstrates that the apex wall shear stress will decrease as blood flows through increasing generations of the arterial tree. Significantly, this is consistent with the sparse population of aneurysms in several generations more away from the circle of Willis.

As discussed throughout this chapter, several assumptions have been introduced in our studies of blood flow in cerebral bifurcations. In this chapter, the flow was modeled as unsteady. This assumption is more appropriate in arteries with small diameters such as the cerebral arteries ($2 \sim 4\ mm$) where the Womersley numbers are small (1.3 – 2.7). Arterial walls are flexible and fluctuate with time under the propagation of pressure waves. In oder to simplify the analysis, in this chapter, we modeled the walls of bifurcations as rigid. The periodic motion of the vessel walls which typically less than 10 % strain throughout the vasculature system ($^{(136)}$), is particularly small in the cerebral arteries due to the dampening of the pulse wave as it travels into the cerebral vasculature. For this reason, the mathematical modeling of the periodic motions of walls is left for future studies in which the propagation of pulse waves is of interest. We have not yet studied the effects of asymmetry in the bifurcation geometry and of varying the area ratios of parent and daughter branches. These geometrical parameters may also be important in determining risk factors. Specifically, an angular asymmetry in bifurcation branches may shift the location of the maximum wall shear stress closer or farther from the apex of the bifurcation and may also alter the maximum wall shear stress. This in turn may alter the position of the aneurysm. We need to undertake a more detailed study of these effects. In this work, we modeled the blood as a Newtonian fluid. Blood is non-Newtonian due to the shear thinning effects of viscosity with shear rate. However, K. Perktold *et al.* showed that there are only minor differences in the magnitude of wall shear stress between studies using Newtonian and shear thinning fluids in a carotid

bifurcation model at fixed flow rate.[157] Their results show that the shear thinning viscosity found in blood lowers the magnitude of wall shear stress at the inner wall by 10% compared with the results of a Newtonian fluid. As a result, the use of Newtonian fluid, slightly overestimates the magnitude of wall shear stress.

3.0 A NOVEL FLOW CHAMBER

3.1 Objectives

Cellular tissues such as endothelial cells, blood cells, bone cells and cardiac cells are under physiological loading conditions *in vivo*.[9,12,123] Endothelial cells are layered on the luminal wall of the blood vessel, exposed to blood flow under a cardiac cycle. The morphological and functional alterations of endothelium due to blood flow have been hypothesized to be responsible for vascular diseases by many researchers.[2,8,129] Mechanical effects such as shear stress, strain and normal stress have been reported to affect the morphology and function of endothelial cells as biomechanical mediators in intercellular reorganization[1,2,4] and.[5–9] Mechanical shear stress deforms original polygonal shapes of endothelial cells to ellipsoidal shapes, aligning them with flow direction.[2,5,7] Moreover, temporal and spatial shear stress gradient have been shown to play an important role in the response of endothelial cells.[16,31–33] These temporal and spatial shear stress gradients locally change cell turnover rate,[15] ion channel activation,[7,11] intercellular signaling,[129] cellular cytoskeleton,[2,11] gene expression at the level of transcription and protein synthesis.[2,4,14–16,129] These local changes may lead to vasoregulation[36] and arterial wall remodeling.[37] In spite of researchers' efforts, the specific mechanisms regulating these cellular responses are not fully understood.

Because of the geometrical complexity of arteries and resolution limitations of current technology to measure wall shear stress and pressure, *in vivo* studies of the endothelial cell response to shear stress have been limited. As a result, various types of *in vitro* flow devices have been developed to simulate the *in vivo* biomechanical environment of the vascular endothelial cells. Current designs of flow chambers include parallel plate geometries,[7,15,17,18,38–40] capillary tube geometries,[41,42] cone–and–plate geometries.[2,5,8,9,16] Most flow devices used in laboratories are parallel plate flow chambers and cone–and–plate viscometers. The cone–and–plate viscometer has the advantage that it does not have a reservoir effect. However, it generates a secondary flow motion with undesirable spatially inhomoge-

neous shear stress levels. On the other hand, the parallel plate flow device generates a reservoir effect but a desirable homogeneous shear stress level without a secondary motion. Because the flow in the parallel plate flow chamber is driven by pressure gradients, the pressure changes nearly linearly in the axial direction of the chamber. In the past, the level of pressure variation has been considered negligible. More recently researchers have begun to explore this effect.[13] Given the wide range of pressure found throughout the arterial system and over one heart cycle, it seems unlikely that the magnitude of pressure plays as significant a role as wall shear stress. We do not discuss the effect of pressure on the cells in this study and it will remain for future work. Most existing flow devices were designed to produce either a homogeneous shear stress or inhomogeneous shear stress found near the recirculation regions of flow past a step. The flow devices which include steps were in general, designed to investigate endothelial cell response to shear stress found in the outer walls of bifurcations where atherosclerotic lesions are localized.[2,14]

Most parallel plate flow chambers have inlet reservoirs to reduce high inertial effects in the chambers so that they produce nearly homogeneous shear stresses on the entire bottom plates. Previous researchers have recognized the significance of the reservoir effect and some have used the results from boundary layer theory[52] to estimate the inertial effect.[17,18,39,48] Entrance length due to momentum transfer from the reservoirs cannot be however, simply obtained by the boundary layer theory, mainly because of the inlet flow condition and the range of Reynolds number assumed in the theory.[52] The uniform flow profile as an inlet condition in the theory is typically quite different from the inlet flow profiles found in the most parallel plate chambers except the flow chamber designed by Ruel *et al.*.[48] The Reynolds number appropriate for the theory is larger than typical Reynolds number used in flow chambers.[17,18] As a result of these two issues, the boundary layer theory significantly underestimates the entrance length for the typical flow chambers.[52] Moreover, viscous dissipation near the side walls of the chamber affects flow characteristics, producing values of shear stress more than 80% of the desired value. The data can be contaminated if the cells

exposed to the altered shear stress are included in the data analysis. Furthermore, the cells exposed to the altered shear stress can influence the response of other cells due to cell–to–cell communication.[31,44–47] Therefore, flow chambers must be carefully designed to obtain meaningful data.

Several authors have reported the analysis of their flow chambers to estimate the effects of the lateral walls and inlet reservoir. Ruel *et al.* injected dye in the flow chamber[48] and Nauman *et al.* used beads[17] to evaluate whether the streamlines were parallel to the chamber wall. Ruel *et al.* used boundary layer theory to estimate the effect of the lateral walls of their own flow chamber.[48] Nauman *et al.* used particle image velocimetry to evaluate whether the velocity field was uniform across the width of the flow chamber.[17] However, there exists an exact solution for fully developed flow in a channel that will be discussed later to evaluate the effect of the lateral walls. Therefore instead of the rough approximation using boundary layer theory which Ruel *et al.* used, the exact solution can be used to evaluate the lateral wall effect. The uniformity of the velocity across the width that Nauman *et al.* concluded is not in accord with the analytic solution and furthermore, the use of relatively large beads which are about one–third the channel height reduced the accuracy of their measurement, as noted by the authors.

We design a flow chamber to expose the endothelial cells to wall shear stress found at the arterial bifurcation to study the hemodynamic effects on the cells near the bifurcation. Clearly understanding the hemodynamic effects on endothelium *in vitro* strongly relies upon a scientifically accurate design process. The accurate observation of desired flow characteristics in laboratories is not easy due to the limitations of apparatus capabilities. Taking advantage of the large increase in computer technology, we took a numerical approach in the design of our flow chamber and therefore, a more quantitative approach in the evaluation of the effects of the inlet and outlet reservoirs and lateral walls, avoiding the rough estimates

of boundary layer theory. Our goal is to design a flow chamber which can provide a substantial region for cell testing outside the region governed by lateral wall, entrance and exit effects.

As discussed in Chapter 2, we expect wall shear stress to play a more major role than pressure in aneurysm formation. Therefore, in the design process, the focus is on reproducing the wall shear stress field. In the numerical studies discussed in Chapter 2, we found that wall shear stress near the apex of the bifurcation is not homogeneous but varies along the neck of the bifurcation. Endothelial cells in this region therefore, experience inhomogeneous shear stress. It is therefore, necessary for us to redesign the existing flow chambers to produce the shear stress characteristics qualitatively and quantitatively similar to those found near the apex of the bifurcation. Our computational approach will demonstrate that a T-shaped flow chamber is appropriate to study the response of endothelial cells to wall shear stress fields found at arterial bifurcations.

Our aim in this analysis is to design flow chambers in which the test endothelial cells are exposed to "well defined flow". As will be discussed later in detail, this "well defined flow" is defined as the flow which satisfies principle design criteria. A parallel plate flow chamber is numerically designed and then built prior to the design of the T-shaped flow chamber. This pre-construction of the parallel plate flow chamber enables us to investigate the methods to prevent leakage of the fluid in the chamber, to eliminate air bubbles captured in the chamber, to control a desired volume flow rate and to manipulate the endothelial cells. Furthermore, the numerical design of the parallel plate flow chamber allows us to investigate the effects of reservoirs and lateral walls. The quantitative and qualitative features of the wall shear stress found in the region of T-junction as well as the effects of reservoirs and lateral walls of the T-chamber can be estimated by the numerical analysis on a two dimensional T-shaped channel and three dimensional parallel plates with a reservoir.

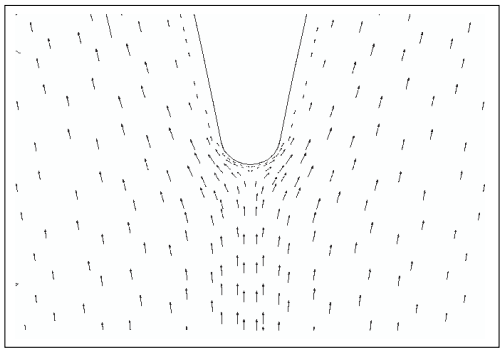

Figure 3.1. Representative velocity profile at the bifurcation with $d_p = 4mm$, radius of curvature $= 0.2mm$, $Re = 255$.

3.2 Flow Characteristics at the Apex of the Bifurcation

In the previous chapter, we developed idealized symmetric models of bifurcated vessels and numerically analyzed blood flow in the vessels, modeling the blood as an incompressible, homogeneous, linearly viscous fluid. The study revealed that wall shear stress found in the region of the apex of the bifurcation is not homogeneous. Due to the geometrical symmetry, the fluid impacts the apex of the bifurcation and then divides symmetrically into the two daughter branches as can be seen in Figure 3.1. The flow then becomes nearly fully developed distal to the apex. Steep velocity gradients present in the region proximal to the stagnation point as shown Figure 3.1. Shown in Figure 3.2 are shear stress contours on the wall of the bifurcation and a shear stress curve along the center neck of the bifurcation. In the figure, the wall shear stress increases up to the maximum value from zero at the apex and decreases to a constant value along the center neck of the bifurcation. We now consider the curve formed by the intersection of the longitudinal plane and the surface of the arterial model. The wall shear stress at points (slice 1) on this curve are shown in Figure 3.3. The other slices correspond to two planes parallel to the longitudinal plane, but progressively further away from the apex point (0.04 mm away from the apex point). If the stress field was perfectly two-dimensional, these curves would be identical. Though the maximum drops slightly, the shear stress is close to two-dimensional in this region. This is likely due to the

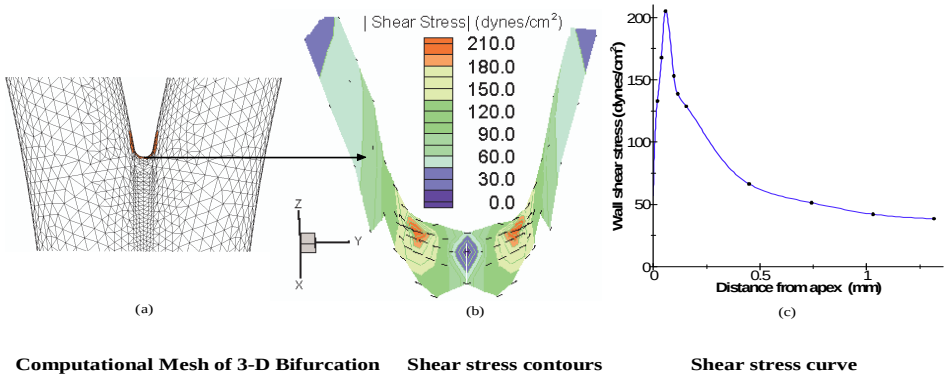

Figure 3.2. Shear stress contours on the wall of the bifurcation and a shear stress curve along the center neck of the bifurcation with $d_p = 4mm$, radius of curvature $= 0.2mm$, $Re = 255$.

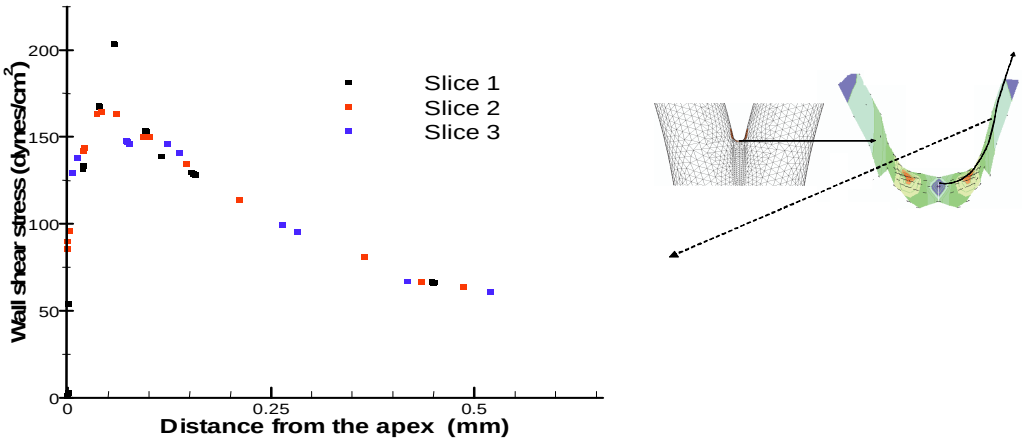

Figure 3.3. Wall shear stresses at points on the curve formed by the intersection of the longitudinal plane and planes parallel to the longitudinal plane and the surface of the arterial model.

fact that the principal radii of curvature at the apex, are opposite in sign and significantly different in magnitude. Our *in vitro* flow chamber model makes use of this two dimensionality. As discussed in the next section, part of our design criteria is to recreate these flow features in the *in vitro* test chamber.

3.3 Criteria for Flow Chamber Design

The principal design criteria for the T-shaped flow chamber for investigating the endothelial cell response to shear stress found in the apex region of the bifurcation are as follows :

1. The flow chamber should reproduce qualitative features of stress field found on arterial walls at the apex of a bifurcation.

2. Quantitative features of the stress field in the test region of the flow chamber should be the same order of magnitude as those found on arterial walls at the apex of a bifurcation

3. The shear stress field should be approximately two dimensional in a large percentage of chamber : "Active Test Region"

4. The "Active Test Region" should be wide enough to obtain sufficient quantities of cells for genetic testing.

In particular, the third criterion is important due to cell–to–cell communication.[31, 44–47] The "Active Test Region" (ATR) is defined as a region where the third criterion is met. In the ATR, the effects of lateral walls and reservoirs should be below a specified magnitude (see Section 3.6). The "well defined flow" is defined as flow which (i) recreates quantitative and qualitative features of stress field found on arterial walls at the apex of a bifurcation (the first and second criteria) and (ii) satisfies the third criterion.

3.4 Methods of Flow Chamber Design

To expose the test endothelial cells to the "well defined flow", the flow in the chamber needs to be quantified. For this purpose numerical studies are carried out. However, the numerical analysis of the three-dimensional T-shaped flow chamber is quite expensive. Moreover, the ratio of the width of the chamber to the height of the channel is quite large. Such a large ratio in geometrical dimension caused numerical instability even for a small Reynolds number in our analysis. We thereby analyze the computational model of the T-chamber by combining two dimensional analysis on the T-shaped channel with three dimensional analysis on two segments of a parallel plate with a reservoir. The following discussion explains how the T-shaped flow chamber can be numerically designed using the combination of the two and three dimensional analyses :

- Two dimensional analysis

  The two dimensional numerical analysis on the T-shaped channel (see for example, Figure 3.27) is performed to satisfy the first and second criterion. Due to the large ratio of the width of the chamber to the height of the channel, in most regions of the chamber, the flow is laterally two dimensional[53, 53] except the regions near the reservoirs and lateral walls. Therefore, the two dimensional analysis is sufficient to inform us about flow characteristics in the region of the T-junction of the chamber except the regions near the reservoirs and lateral walls. The effects of the reservoirs and lateral walls will be evaluated using a three dimensional analysis.

- Three dimensional analysis

  The third and fourth design criterion are achieved using a three dimensional numerical computation on the following two models of segments of a parallel plate,

  1. A parallel plate with the inlet reservoir, Model 1 (see for example, Figure 3.29)

2. A parallel plate with the outlet reservoir, Model 2 (see for example, Figure 3.30)

Because the two daughter branches with the outlet reservoirs are symmetric, only one model (Model 2) is employed. Instead of using the entire chamber, the two models of segments are used to evaluate the effects of inlet and outlet reservoirs. Since the flow in the regions beyond an entrance or exit length is nearly fully developed, a fully developed condition can be specified at the inlet of Model 2 or outlet of Model 1. The height of the parent branch and length of the daughter branch are chosen to be sufficiently long for this purpose. However, there are flow disturbances due to the effect of the lateral walls in the region of the T-junction. The effect can not be evaluated by this analysis. Since the effect of lateral walls of a rectangular duct with a large geometrical ratio is very small as will be discussed later, we assume that the effect is small. So, it will not be discussed in this study and will remain for future work.

This combination of the two and three dimensional approaches decreases the necessary computational work. It should be also noted that the dimensions of the chambers should be carefully chosen for both the requirement of the design criteria and numerical stability.

As discussed previously, the construction of the parallel plate flow chamber precedes that of the T-shaped flow chamber. We also study the effect of size of the reservoir on the entrance length from the numerical design of the parallel plate chamber and then use the result to determine the size of the reservoir of the T-shaped flow chamber. The parallel plate flow chamber has been successfully built using the numerical results and tested in our laboratory. We begin our design analysis with the numerical design of the parallel plate flow chamber.

3.5 Mathematical and Numerical Formulations

The numerical analyses for the design of both the flow chambers are performed by modeling the perfusion fluid as incompressible, homogeneous and linearly viscous. In this case,

Equations 2.1 – 2.3 are the governing equations for the fluid. The boundary conditions 2.8, which are employed in the previous bifurcation studies are used again for this study.

Equations 2.1 – 2.3 with the boundary conditions 2.8 are solved using ADINA software package. The Newton–Raphson method is used to linearize the nonlinear finite element equations and a sparse solver is used to solve a linear set of algebraic equations.[66] The detailed numerical methods employed in ADINA fluid solver are discussed in Chapter 2, Section 2.4.2.

3.6 Parallel Plate Flow Chamber

For the design analysis of the parallel plate flow chamber, we only need the third and fourth design criterion. We first discuss the shear stress field on the bottom plate where cells are grown. In classical parallel flow devices, the assumption that all cultured cells are exposed to nearly the same shear stress in magnitude and direction is made for the data analysis. Some flow devices use a sub–domain of the entire bottom surface for testing the cells.[39,48,49] In other chambers, the cells are cultured on the entire surface of the bottom plate.[17,18] In both cases, the shear stress, $\tau_{fd_{2D}}$ for two dimensional, steady, fully developed flow between two infinite parallel plates is assumed to be applied to all the cells. As will be discussed later in detail, the relationship between the wall shear stress and the volume flow rate for the flow is assumed to be

$$\tau_{fd_{2D}} = \frac{6Q\mu}{wh^2}, \tag{3.1}$$

where μ is the fluid viscosity, w is the channel width and h is the channel height. However, the wall shear stress is not homogenous on the entire surface of the bottom plate due to the inlet and outlet effects from the reservoirs and viscous effects from the side walls. For example, the wall shear stress near the lateral walls deviates more than 80% of that expected by Equation 3.1.[98] The deviation due to the reservoir effect may be much larger. For a given flow rate, Q the test cells are supposed to experience the wall shear stress close to that

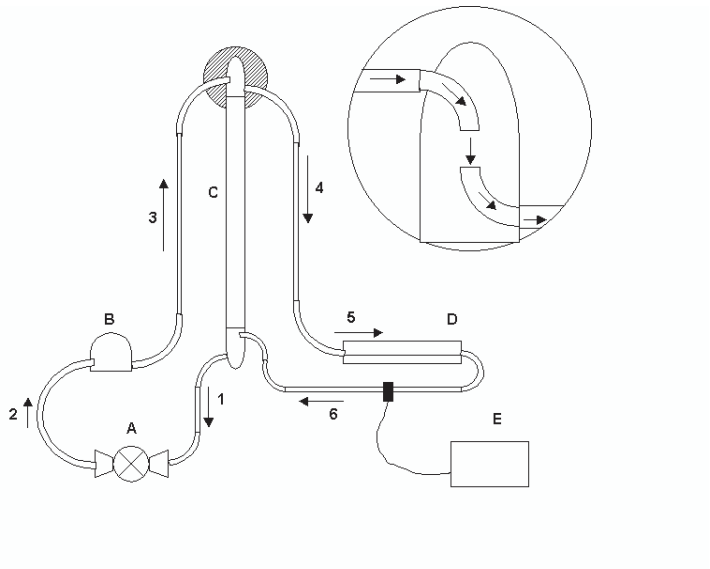

Figure 3.4. Schematic of flow loop.

predicted by Equation 3.1 since the cells are confined to a sub-region of the entire bottom surface in some existing flow chambers.[39,48,49] However, not many authors have measured the effects of reservoirs and lateral walls quantitatively. In our study, both numerical and analytical methods are approached to measure such effects. We then identify an "Active Test Region" (ATR) defined as the region where wall shear stress is within a chosen percentage of 3.1 to meet the third and fourth criterion, which will be discussed in detail in later section.

3.6.1 Flow Loop for Parallel Plate Flow Chamber

A schematic of flow loop is shown in Figure 3.4. The flow loop is described as follows :

1. Culture medium is pumped from lower reservoir of head tube [C] with peristaltic pump [A].

2. The fluid flows through pulse dampener [B] to eliminate pump vibration and achieves steady flow.

3. The fluid is raised to the top of head tube [C] where head driven flow begins. Fluid

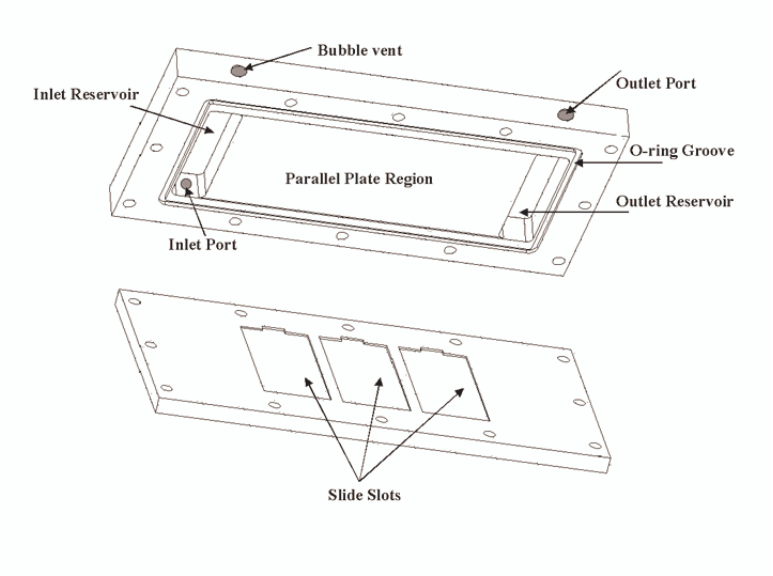

Figure 3.5. A assembled parallel plate flow chamber.

passes from the inlet tube to the outlet tube as shown in the blow up view and atmospheric pressure is achieved. Any extra fluid pumped to the top of the head tube is allowed to overflow and runs down to the lower reservoir.

4. Fluid flow is driven by the height difference inside the head tube.

5. The fluid enters the flow chamber [D] and comes in contact with the endothelial cells exposing them to the desired shear stress.

6. The fluid passes by an ultrasonic flow meter [E] and into the lower reservoir of the head tube to be pumped back through the system.

The parallel plate flow chamber is designed by modifying a chamber proposed by J.A. Frangos *et al.*.[18] The parallel plate flow chamber shown in Figure 3.5 is composed of two machined acrylic sheets. The bottom plate has rectangular recessed areas to allow for three high tolerance slides to be inserted. These slides, on which the endothelial cells are cultured, have a tolerance of .001 inch to prevent movement when flow passes over the slides. The upper plate is machined to include three recessed regions, an entrance reservoir, the flow path, and an exit reservoir. The flow region is machined to 6.50 $\times$ 2.75 $\times$ .020 inch and

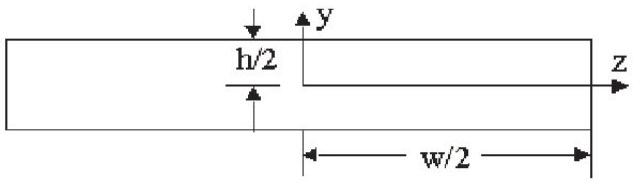

Figure 3.6. Cross section of flow chamber in yz plane.

is flanked by the two reservoirs of .75 × 3.75 × .625 inch. The two plates are sealed with an o-ring and screwed together with 12 screws that are capped with plastic tees for easy hand tightening. The 12 screws ensure that a good seal is kept around the o-ring as well as maintaining the .020 inch gap inside the chamber. The medium flows into the inlet reservoir through the cylindrical opening and flows out from the out reservoirs. Figure 3.6 shows the vertical cross sectional view of the parallel plate region. Referred to a rectangular Cartesian coordinate system (x, y, z), the top and bottom plates are placed at $y = \pm h/2$ while the lateral walls at $z = \pm w/2$, making the parallel plate region of the thickness h and width w. The bottom plate of the flow chamber can be seen in Figure 3.7. The interfaces between the inlet reservoir and the parallel plate region and between the outlet reservoir and the parallel plate region are located at $x = 0$ and $x = L$, respectively. The Active Test Region denoted in the figure will be discussed in detail in a later section. Table 3.1 shows the dimensions of the flow chamber as well as three other representative parallel plate flow devices.

The comparison of flow in chambers with reservoirs of two different lengths is made to investigate the effect of size of the reservoir on the entrance and exit length. The height and width of the reservoirs are 1.6 cm and 1.9 cm, respectively. One of the flow chambers has an inlet and an outlet reservoir of the length equal to the channel width, w (shorter reservoir) as shown in Figure 3.11. The other flow chamber is designed to have 25% longer (9.4 cm long) reservoirs than the shorter reservoir by equally lengthening both the inlet and outlet reservoirs in ±z-direction as shown in Figure 3.12.

Table 3.1. Geometric parameters for flow chambers .

Chamber	h (cm)	w (cm)	L (cm)	β = h/w	Range of Re (20^oC) for $\tau_{fd_{2D}} \in [10, 55]$ dynes/cm^2	Range of Re (37^oC) for $\tau_{fd_{2D}} \in [10, 55]$ dynes/cm^2
Chung *et al.*	0.0254	7.6	16.5	0.0033	[13,59]	[26,109]
Chung *et al.*	0.050	7.6	16.5	0.0066	[50,229]	[101,464]
Frangos[18]	0.0254	2.3		0.011	[13,59]	[26,109]
Nauman *et al.*[17]	0.022	4.1		0.0054	[9.7,44]	[20,90]
Ruel *et al.*[48]	0.1	7.5		0.014	[200,917]	[405,1858]

3.6.2 Dimensionless Parameters

The non-dimensional parameters used in this analysis are the Reynolds number Re, and the lateral channel aspect ratio β, which can be expressed in the forms of

$$Re = \frac{\rho \bar{V} h}{\mu}, \quad \beta = \frac{h}{w}, \tag{3.2}$$

where $\bar{V}$ is the average velocity, $Q/(hw)$. These two dimensionless parameters determine the size of the ATR. It will be discussed later that the length of the ATR determined by the effect of the reservoirs is a function of Re and β, whereas the width of ATR determined by the effect of lateral walls is a function of β. The values of β commonly used in current flow chambers are listed in Table 3.1 and will be discussed later.

We denote the distance between the ATR and the channel inlet, outlet and lateral walls as L_{en}, L_{ex} and L_w, respectively, Figure 3.7. We define the dimensionless variables of L_{en}, L_{ex} and L_w for later convenience as follows.

$$\tilde{L}_{en} = \frac{L_{en}}{L}, \qquad \tilde{L}_{ex} = \frac{L_{ex}}{L}, \qquad \tilde{L}_w = \frac{L_w}{w/2}. \tag{3.3}$$

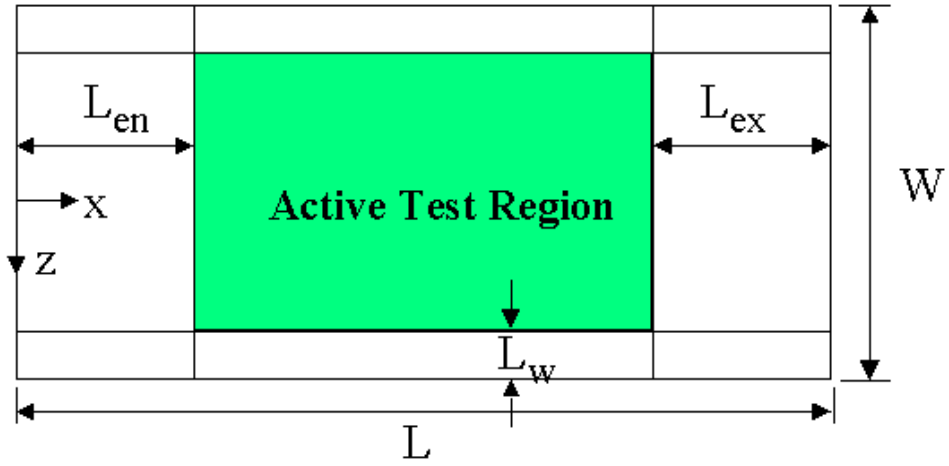

Figure 3.7. Cross section of flow chamber in xz plane with schematic of Active Test Region.

3.6.3 Evaluation of Active Test Region

As emphasized in the earlier section, flow chambers are designed to produce a homogeneous shear stress on their lower plates for cell testing. When one tests biological cells under shear forces and evaluates the biological data, it is commonly assumed that the flow field over the cells is purely two dimensional and fully developed. For such a flow field, the velocity field and corresponding volume flow rate can be obtained by considering steady flow between infinite parallel plates such that

$$\vec{v} = \frac{h^2}{8\mu}(-\frac{dp}{dx})(1-(\frac{y}{h/2})^2)\vec{e}_x, \tag{3.4}$$

$$Q = \frac{h^3 w}{12\mu}(-\frac{dp}{dx}). \tag{3.5}$$

It follows that the stress vector $\vec{t}$ obtained from Cauchy stress tensor, Equations 3.4 and 3.5 on the lower plate is

$$\vec{t} = 6\frac{Q\mu}{wh^2}\vec{e}_x - p(x)\,\vec{e}_y. \tag{3.6}$$

We denote the $\vec{e}_x$ component of Equation 3.6 as the wall shear stress, $\tau_{fd_{2D}}$ and already given in Equation 3.1. Another purpose in the design process of the flow chamber is to develop

a flow chamber with a sufficient area for cells. It is therefore, somewhat necessary to choose a reasonable deviation for $\tau_{fd_{2D}}$ to obtain the Active Test Region.

Generally, the wall shear stress, τ_w found on the entire surface of the lower plate is a function of x and z due to the effects of lateral walls and reservoirs. We define the ATR as a region where the following inequality condition is satisfied.

$$100\ \frac{|\tau_w(x,z) - \tau_{fd_{2D}}|}{|\tau_{fd_{2D}}|} \leq \gamma. \tag{3.7}$$

The Active Test Region is evaluated by using a chosen γ. Thereby, the chosen percentage, γ of $\tau_{fd_{2D}}$ determines the size of the ATR. The choice of a value of γ is not quite straightforward because it is still unknown how sensitively the endothelial cells respond to the magnitude of shear stress. We choose the value of γ of 5% in this study.

As shown in Figure 3.7, the ATR is a rectangular sub-region of the entire surface of the lower plate. However, the largest possible ATR will not be in general, rectangular. We make use of three variables, L_{en}, L_{ex}, L_w to determine the largest possible rectangular ATR (see Figure 3.18). The ATR is evaluated in a way that we find the corresponding smallest possible values of L_{en} and L_{ex} for a chosen value of L_w that satisfy the condition 3.7.

3.6.4 Analytical Solutions

We now begin to quantify the effects of reservoirs and lateral walls. In this section, we confine our attention to classic "analytic results" that are applicable to our design analysis.

3.6.4.1 Inlet Length.

When fluid flows a rectangular duct or cylindrical conduit from a large reservoir, inertial force dominates in the inlet region of the duct or conduit.[50] The inertial force dies out

within a certain distance while viscous force begins to dominate. This distance is commonly called "Inlet Length" while such an effect is called "Entrance Effect". In general, fluid flow is said to be fully developed when inertial force is very small relative to viscous force. However, the flow never becomes fully developed in a finite distance from the inlet of a duct because the velocity field is an analytic function.[51] The inlet length is still useful for practical purposes as a method to estimate when the flow is approximately fully developed.

One of the typical and classic examples of analytic approaches in order to predict the entrance length is the solution of the inlet length for the flow in a semi-infinite two dimensional straight channel with flat parallel walls based on boundary layer theory.[52] The actual inlet length estimated by this theory is $L_e = 0.04Re\ h$. The result agrees well with the corresponding numerical solution to full Navier Stokes equations. However, this estimate is not a good approximation in obtaining the inlet length of our flow chamber. There are a few reasons. Generally, the inlet length depends on the inlet velocity profile, the Reynolds number, cross sectional geometry and the measure being used to asses the degree of fully developed flow. The value of inlet length from the boundary layer theory is predicted based on unidirectional flow with a constant magnitude at the inlet cross section. And, secondly, the boundary layer results are valid only for large Reynolds number.[52] Typical flow chamber experiments employ too small a Reynolds number to use the boundary layer theory to find the entrance length. Moreover, the velocity vectors of the flow entering the inlet cross section from the reservoir of our flow chamber are not uniaxial and of constant magnitude. The vectors have three non-zero components being functions of the spatial variables (x, y, z) at the inlet. The profile generated by typical flow chambers is also far from uniform. Three dimensional numerical analysis, which will be discussed in later section is therefore, the only source to calculate the inlet length of our flow chamber.

3.6.4.2 Effect of Lateral Walls in Fully Developed Region.

We now focus our attention on the effect of lateral walls to obtain L_w which relies upon the dimensionless parameter, β given in Equation 3.8 for fully developed flow. Unlike the inlet length, the effect of lateral walls in the region where the flow is fully developed purely due to viscous dissipation can be quantitatively measured by an analytical approach. The analytic solution for steady, fully developed flow in a channel of rectangular cross section is given by[53,53] (see also[55]) and therefore, L_w can be directly calculated from the solution. The velocity field, the corresponding flow rate and wall shear stress referred to rectangular Cartesian coordinate are

$$\begin{aligned}
\vec{v}(y,z) &= \frac{h^2}{8\mu}(-\frac{dp}{dx})\left[(1-\frac{y^2}{(h/2)^2}) - \frac{32}{\pi^3}\sum_{n=1,3,5...}^{\infty}(-1)^{\frac{(n-1)}{2}}\frac{\cosh(\frac{n\pi z}{h})}{\cosh(\frac{n\pi w}{2h})}\frac{\cos(\frac{n\pi y}{h})}{n^3}\right]\vec{e}_x, \\
Q &= \frac{h^3 w}{12\mu}(-\frac{dp}{dx})\left[1-\frac{192}{\pi^5}\frac{h}{w}\sum_{n=1,3,5...}^{\infty}\frac{1}{n^5}\tanh(\frac{n\pi w}{2h})\right], \\
\tau_{fd_{3D}}(z) &= \frac{h}{2}(-\frac{dp}{dx})\left[1-\frac{8}{\pi^2}\sum_{n=1,3,5...}^{\infty}\frac{1}{n^2}\frac{\cosh(\frac{n\pi z}{h})}{\cosh(\frac{n\pi w}{2h})}\right].
\end{aligned} \tag{3.8}$$

Combining Equation 3.1 with 3.8, the non-dimensional wall shear stress for fixed flow rate reduces to

$$\tilde{\tau}(\tilde{z}) = \frac{\tau_{fd_{3D}}(\tilde{z})}{\tau_{fd_{2D}}} = \left[\frac{1-\frac{8}{\pi^2}\sum_{n=1,3,5...}^{\infty}\frac{1}{n^2}\frac{\cosh(\frac{n\pi\tilde{z}}{2\beta})}{\cosh(\frac{n\pi}{2\beta})}}{1-\frac{192}{\pi^5}\beta\sum_{n=1,3,5...}^{\infty}\frac{1}{n^5}\tanh(\frac{n\pi}{2\beta})}\right], \tag{3.9}$$

where the dimensionless variable $\tilde{z} = z/(w/2)$. The non-dimensional wall shear stress, $\tilde{\tau}(\tilde{z})$ in Equation 3.9 provides information about the deviation of the wall shear stress of the region where the flow is fully developed in the parallel plates relative to the wall shear stress of the ATR.

Figure 3.8 shows the profile of the normalized wall shear stress along the width of the channel. As β decreases, $\tilde{\tau}$ becomes flatter and thereby, the value of L_w decreases. The value of the wall shear stress at the center is slightly different than $\tau_{fd_{2D}}$. The aspect ratio β turns

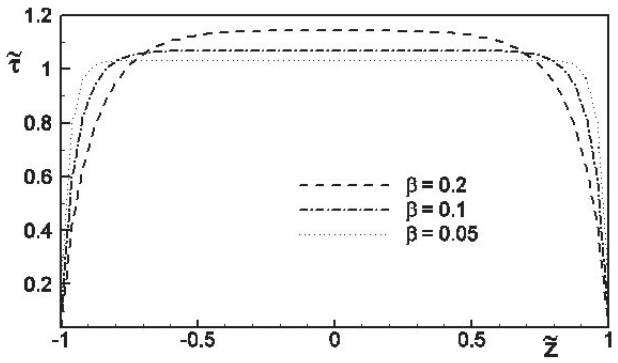

Figure 3.8. Non-dimensional wall shear stress as a function of $\tilde{z}$ for $\beta = 0.05, 0.1, 0.2$.

out to play an important role in obtaining sufficiently large ATR. As seen in Figure 3.9, a critical value, β^* that the equality condition of (3.7) is met is around 0.074 for $\gamma = 5\%$. β must be less than β^* because for larger β than β^*, the wall shear stress at the center of the chamber is so different from $\tau_{fd_{2D}}$ that condition (3.7) will not be met for $\gamma = 5\%$. The values of β for the flow chambers discussed here are all less than 0.014 as listed in Table 3.1. It can be seen from Figure 3.10 that the $\tilde{L}_w$ is only a function of the aspect ratio, β and the Reynolds number does not play any role on this length, $\tilde{L}_w$. Within the chamber outside the inlet length, $\tilde{L}_w$ can be easily calculated from Equation 3.8. $\tilde{L}_w$ as a function of β is shown in Figure 3.10 by considering three criterion of γ : 5.0%, 10.0% and 20.0%. This figure covers the range of β for all the flow chambers we consider in Table 3.1. The function $\tilde{L}_w(\beta)$ is nearly linear in the range of β shown in the figure for both criterion. Table 3.2 shows the values of $\tilde{L}_w$ for all the flow chambers. The effect of lateral walls is comparatively small for all the flow chambers discussed here. A more profitable way to obtain the largest possible ATR is to select larger L_w than the values of L_w evaluated in this section. The explanation will be given in the result section.

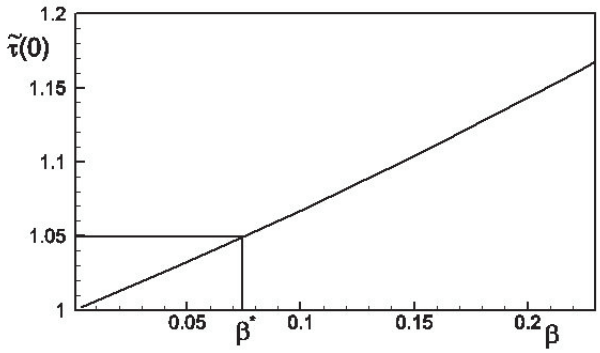

Figure 3.9. Non-dimensional wall shear stress as a function of aspect ratio β for $\tilde{z} = 0$.

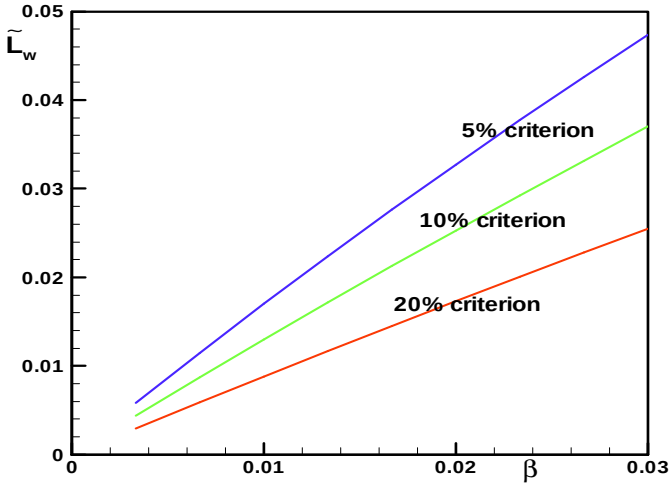

Figure 3.10. Dependence of $\tilde{L}_w$ on β for $\gamma = 5.0\%$, 10.0% and 20.0%.

Table 3.2. Values of $\tilde{L}_w$ and L_w for fully developed flow in two flow chambers with $\gamma = 5.0\%$.

Chamber	β	$\tilde{L_w}$	w/2	L_w
5.0 % Criterion				
Chung *et al.*	0.0033	0.0058	3.8 cm	0.022 cm
Frangos[18]	0.011	0.019	1.15 cm	0.021 cm
Nauman *et al.*[17]	0.0054	0.0093	2.05 cm	0.019 cm
Ruel *et al.*[48]	0.014	0.023	3.75 cm	0.088 cm

3.6.5 Numerical Analysis

As discussed earlier, the analytical solution based on the boundary layer theory is not applicable to the studies of L_{en} and L_{ex}. Instead, we perform a numerical analysis to study the entrance, exit and lateral effects outside the fully developed region. By virtue of the symmetry of our parallel plate flow chamber and rapid development of the flow field for the range of Reynolds numbers used in this study, the half models of the flow chamber are employed (see Figure 3.11) for our numerical analysis. As a result, one half model is used for two half parallel plates with a reservoir: a half chamber with an inlet reservoir (Inlet Chamber) to obtain L_{en} and a half chamber with an outlet reservoir (Outlet Chamber) to obtain L_{ex}. A computational model for the two chambers, which is composed of one half of the rectangular channel, the rectangular reservoir and a connecting segment of pipe is seen in Figure 3.11. The fluid enters at the pipe opening, Γ_1 and exits at the outlet of the half chamber, Γ_2 for the inlet chamber. For the outlet chamber, the fluid enters at Γ_2 and exits at Γ_1.

3.6.5.1 Numerical Boundary Conditions.

No slip conditions are applied on the surrounding walls. Let us now consider boundary conditions specified at Γ_1 and Γ_2 for both chambers. At the inlet, Γ_1 and outlet, Γ_2 of both chambers, C_2 is set to zero and C_1 is chosen to obtain a desired flow rate for the inlet chamber in Equation 2.8. For the outlet chamber, identical boundary conditions to those for

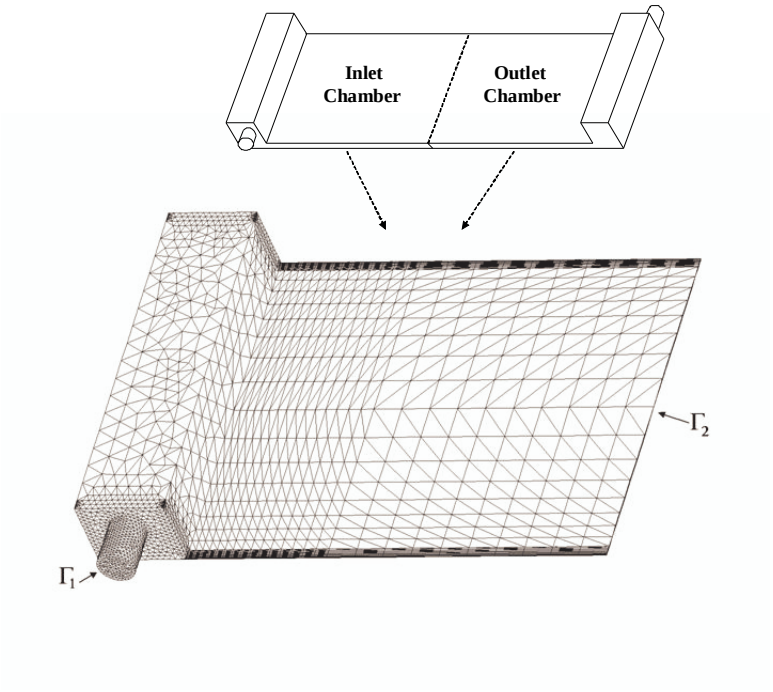

Figure 3.11. Distribution of mesh in computational domain for shorter reservoir.

the inlet chamber are specified. C_2 is set to zero and C_1 is chosen to obtain the same flow rate with that for the inlet chamber. C_1 is a positive constant for the inlet chamber and a negative constant for the outlet chamber. Prescribing these boundary conditions result in nearly fully developed flow at the cylindrical opening, Γ_1 and the outlet boundary of the parallel plate region, Γ_2.

3.6.5.2 Mesh Refinement Study.

Regular meshes are combined with irregular meshes in the computational domain in ADINA, version 7.5. A rule-based mesh (regular mesh) is used for the rectangular channel in conjunction with a free-form mesh (irregular mesh) for the reservoir and pipe opening. We employ a Delaunay mesh algorithm generating four-node tetrahedral elements for the free form mesh. Figure 3.11 and 3.12 show the computational fluid meshes of two models used in this study. In order to increase the accuracy of numerical solutions the meshes are refined near the lateral walls, the junction of the pipe and reservoir as well as the junction of the channel and reservoir, where steep velocity gradients are expected. The number of meshes near the lateral walls is gradually increased in the lateral direction in order that the shear

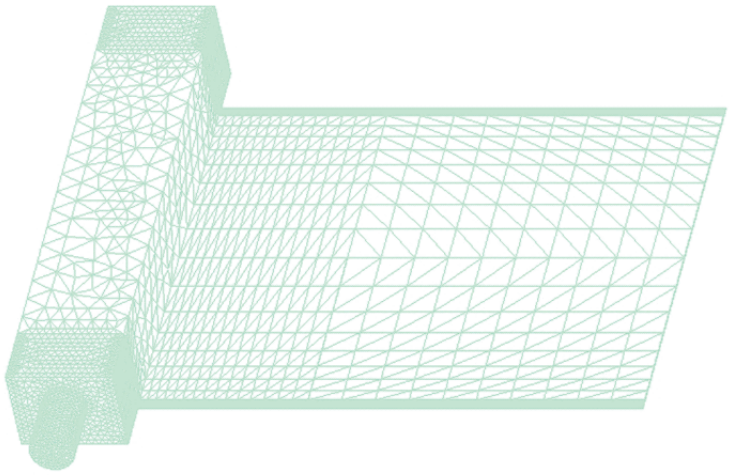

Figure 3.12. Distribution of mesh in computational domain for longer reservoir.

stress near the side walls are computed more accurately. Even highly elevated element density is employed very near the lateral walls in Figures 3.11 and 3.12 because steep velocity gradient presents very near the side walls. The meshes are also refined in the junction of the cylindrical opening and reservoir. In addition, the mesh density is increased gradually from right to left in the axial direction in Figures 3.11 and 3.12 in order to perform the computation with care in highly inertial regions.

In modeling a numerical fluid domain, the determination of a proper mesh density is critical to obtain satisfactory results. The execution of mesh refinement study is the only source to derive confident results because exact solutions or experimental results are not available in this study. The inlet length caused by the inertial force from the reservoir is considered as a factor in determining the appropriate mesh density in our study. Mesh refinement is considered to be sufficient when the successive increment of the element density in steps of 10,000 elements results in less than 8% change in the calculated inlet length, L_{en}, which is seen to be a significant deceleration in slope from the previous mesh elements. Based on the result, over 80,000 four–node tetrahedral elements are generated and used in

all computational studies. The results of the mesh refinement study are listed in Table 3.3 for two different choices of L_w.

Table 3.3. Results for Mesh Refinement Study .

L_w = 0.21 cm	
Number of Elements	L_{en} (cm)
60,000	1.52
70,000	2.04
80,000	2.22

L_w = 0.031 cm	
Number of Elements	L_{en} (cm)
60,000	3.62
70,000	3.62
80,000	3.62

3.6.5.3 Numerical Results and Discussion.

$\tilde{L}_{en}$ and $\tilde{L}_{ex}$ are a function of the Reynolds number as emphasized previously. The Reynolds numbers studied here are 16.1, 33.1 and 51.8 and their corresponding values of $\tau_{fd_{2D}}$ (at 20^o C) are 15.0, 30.1 and 48.0 dynes/cm^2. The typical range of the wall shear stress considered in most flow chambers is from 10 to 55 dynes/cm^2. As can be seen in Figure 3.13 and 3.14, The values of $\tilde{L}_{en}$ and $\tilde{L}_{ex}$ as a function of Re for two choices of L_w for the shorter reservoir are plotted. $\tilde{L}_w$ is chosen to be 0.008 in Figure 3.13, while $\tilde{L}_w$ is 0.055 in Figure 3.15. These values become higher as Re increases overall. The values of $\tilde{L}_{ex}$ are smaller than $\tilde{L}_{en}$, which means that the inlet reservoir has a more serious effect on the entrance length than the effect of the outlet reservoir on the exit length. In addition, both $\tilde{L}_{en}$ and $\tilde{L}_{ex}$ increase as $\tilde{L}_w$ is decreased. $\tilde{L}_{en}$ and $\tilde{L}_{ex}$ for the two reservoirs are compared for two different $\tilde{L}_w$ at Re = 33.1, 51.8. In Figure 3.15, the comparison of $\tilde{L}_{en}$ is made for the two reservoirs when $\tilde{L}_w = 0.008$ (L_w = 0.031 cm) while in Figure 3.16, $\tilde{L}_w = 0.055$ (L_w =0.21 cm). $\tilde{L}_{ex}$ for the shorter reservoir is compared to $\tilde{L}_{ex}$ for the longer reservoir when $\tilde{L}_w$ = 0.008 in Figure 3.17. These figures illustrate that the longer reservoir dramatically reduces $\tilde{L}_{en}$ and $\tilde{L}_{ex}$ for both $\tilde{L}_w$ at Re = 33.1 and 51.8 and thereby, increases the size of the Active Test Region as shown in Table 3.4.

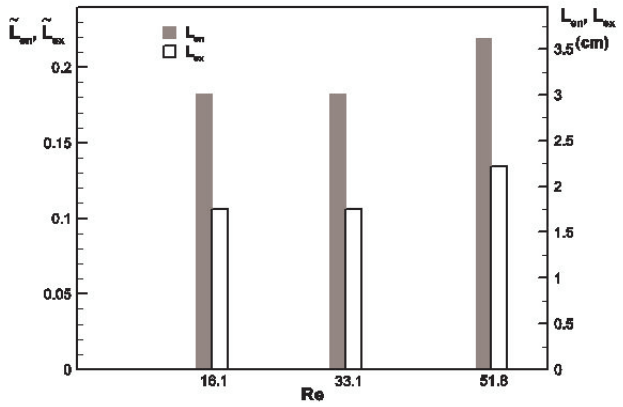

Figure 3.13. Dependence of $\tilde{L}_{en}$ and $\tilde{L}_{ex}$ on Reynolds number for $\tilde{L}_w = 0.008$, ($L_w = 0.031cm$) and Re = 16.1, 33.1, 51.8 ($\tau_{fd_{2D}} = 15.0, 30.1, 48.0 dynes/cm^2$).

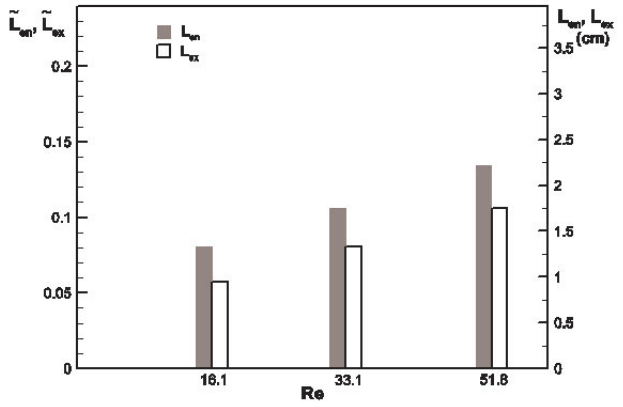

Figure 3.14. Dependence of $\tilde{L}_{en}$ and $\tilde{L}_{ex}$ on Reynolds number for $\tilde{L}_w = 0.055$, ($L_w = 0.21cm$) and Re = 16.1, 33.1, 51.8 ($\tau_{fd_{2D}} = 15.0, 30.1, 48.0 dynes/cm^2$).

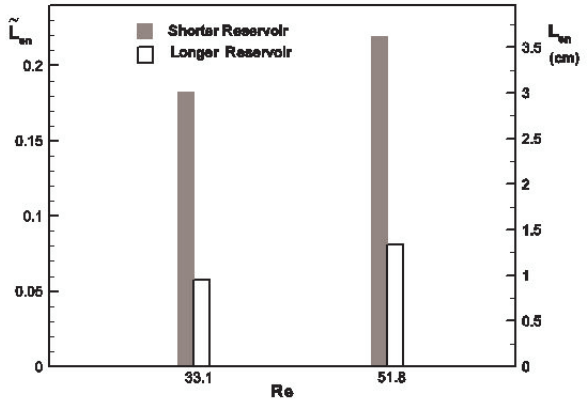

Figure 3.15. Comparison of $\tilde{L}_{en}$ for two reservoirs for $\tilde{L}_w = 0.008$, ($L_w = 0.031cm$) and Re = 33.1, 51.8 ($\tau_{fd_{2D}} = 30.1, 48.0 dynes/cm^2$).

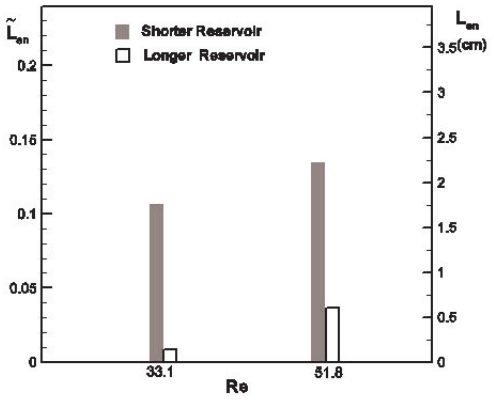

Figure 3.16. Comparison of $\tilde{L}_{en}$ for two reservoirs for $\tilde{L}_w = 0.055$, ($L_w = 0.21cm$) and Re =33.1, 51.8 ($\tau_{fd_{2D}} = 30.1, 48.0 dynes/cm^2$).

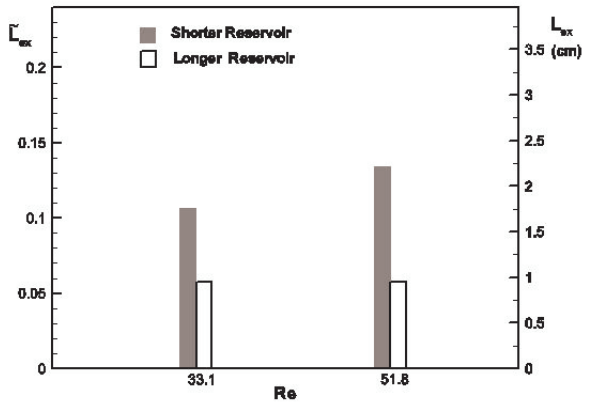

Figure 3.17. Comparison of $\tilde{L}_{ex}$ for two reservoirs for $\tilde{L}_w = 0.008$, ($L_w = 0.031cm$) and Re = 33.1, 51.8 ($\tau_{fd_{2D}} = 30.1, 48.0 dynes/cm^2$).

For illustrative purpose, two possible Active Test Regions of the flow chamber with longer reservoirs are shown in Figure 3.18. Since the shape of the ATR is not unique, our preferable shape of the ATR is chosen to be a rectangle so that we can easily control the areas where biological cells are grown. The choice of L_w is based on experimental or design considerations so, we can choose the values of L_w to maximize the area of the ATR. The values of areas of the ATR listed in Table 3.4 illustrate that for the range of Re used in this study, the choice of larger L_w results in larger area of the ATR for both flow chambers : one with shorter reservoirs and the other with longer reservoirs. The increment of L_w from 0.031 cm to 0.21 cm increases the size of the ATR as shown in Table 3.4. The larger areas of the ATR are obtained in the flow chamber with longer reservoirs compared to the flow chamber with shorter reservoirs for the two choices of L_w at $Re = 33.1$ and 51.8. The longer reservoir increases the sizes of the ATR by 25% on the average for all selected L_w at $Re = 33.1$ and 51.8. The individual percentage of the improvement on the size of the ATR are shown in Table 3.4. Note that the highest values of L_{en} and L_{ex} are always found near the side wall opposite to the inlet or outlet cylindrical opening.

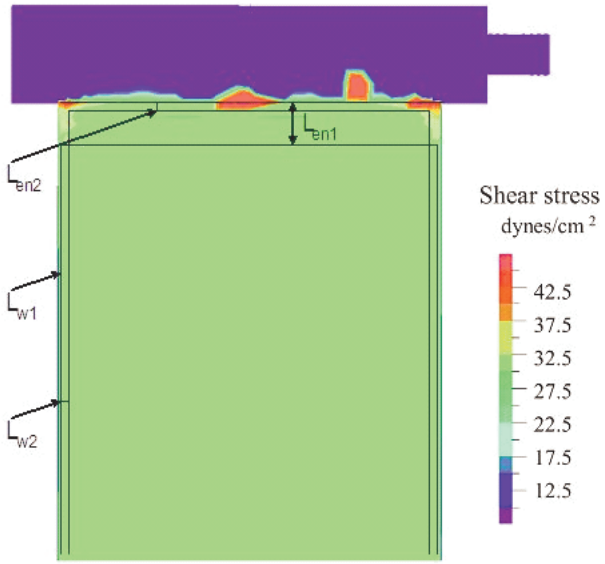

Figure 3.18. Representative figure of contours of constant wall shear stress and two possible Active Test Regions.

Table 3.4. Summary of size of active test region as a function of Re and L_w for two reservoir geometries .

			Shorter reservoir				Longer Reservoir			
Re	L_w (cm)		L_{en} (cm)	L_{ex} (cm)	Area of ATR (cm^2)		L_{en} (cm)	L_{ex} (cm)	Area of ATR (cm^2)	% of improvement %
16.1	0.031		3.02	1.75	88.7					
33.1	0.031		3.02	1.75	88.7		0.95	0.95	110.5	24.57
51.8	0.031		3.62	2.22	80.6		1.33	0.95	107.6	33.5
16.1	0.21		1.33	0.95	102.5					
33.1	0.21		1.75	1.33	96.7		0.14	0.14	116.9	20.89
51.8	0.21		2.22	1.75	90.2		0.60	0.14	113.6	25.9

The physical locations of the first and second glass slides are $x = 2.2\ cm$ and $x = 14.3\ cm$, respectively. Therefore, for the flow chamber with shorter reservoirs the larger value of L_w (0.21 cm) must be used to assure that all cells can be confined in the well defined ATR, even for the small Re. The flow chamber with longer reservoirs on the other hand, can use both the values of L_w in Table 3.4. The largest possible ATR is obtained by using the longer reservoir, choosing the larger value of L_w as shown in Table 3.4. This ensures a room of over $85cm^2$ for cultured cells given by three distinct slides in the Active Test Region.

Care should be taken when we calculate the flow rate and Re using a desired wall shear stress since the fluid density, ρ and viscosity, μ depend on temperature. We typically use the properties of water for those of the perfusion fluids. The values of ρ and μ of water are 1.0 g/cm^3 and 0.01 g/(cm s) (see,e.g.[50]), respectively at 20^{o}C and 1 atmospheric pressure. However, in typical experiments of the flow chambers, physiological conditions are used. In that case, temperature and pressure are maintained near 37^o and 1 atm and then, the density of water is nearly unchanged, 0.993 g/cm^3 and the viscosity drops to 0.007 g/(cm s) (see,e.g.[50]), which is about 30% decrease. A number of researchers overestimated the wall shear stress by using the density and the viscosity of water at 20^{o}C and 1 atm of pressure for their experimental runs at 37^{o}C. The relationship between wall shear stress based on the viscosity (actual viscosity) at 37^{o}C and wall shear stress (expected viscosity) at 20^{o}C is in a form of

$$\tau_{fd_{2D}}(\text{actual}) = 0.7\tau_{fd_{2D}}(\text{expected}) \tag{3.10}$$

The values of the Reynolds number at 20^{o}C and 37^{o}C for all the flow chambers when the range of $\tau_{fd_{2D}}$ is 10-55 dynes/cm^2 are listed in Table 3.1.

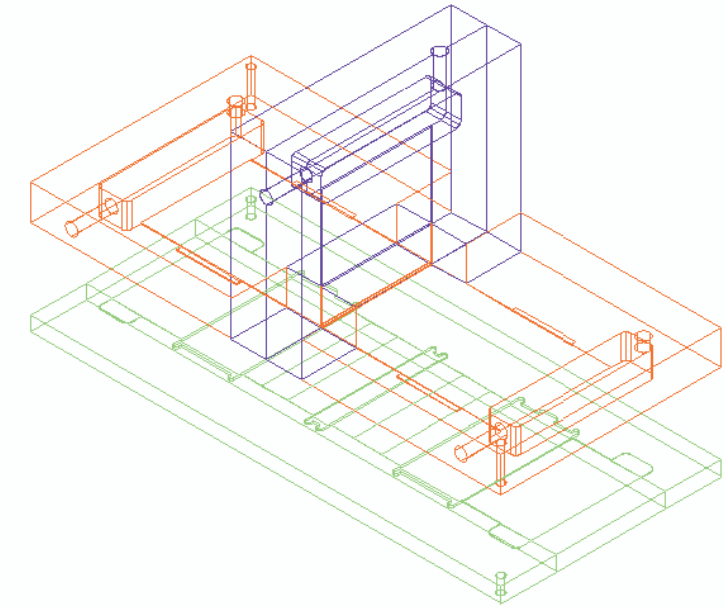

Figure 3.19. A 3-D assembled T-shaped flow chamber.

3.7 T-shaped Flow Chamber

Our main goal for this research is to construct the T-shaped flow chamber to test endothelial cells exposed to wall shear stresses found at arterial bifurcations and in straight arteries simultaneously. The T-flow chamber is numerically designed using all the design criteria discussed in Section 3.3 and built based on the computational results. We have designed and manufactured the parallel plate flow chamber by evaluating the effects of reservoirs and lateral walls using the third and fourth design criteria. The purpose of pre-construction of the parallel plate flow chamber was to develop methods for eliminating air bubbles, preventing fluid leakage, controlling a desired flow rate and manipulating the cells.

3.7.1 Flow System for T-shaped Flow Chamber

The T-shaped flow chamber is designed to have three reservoirs : one upper reservoir at the inlet and two lower reservoirs at the outlets. Culture medium flows into the upper reservoir and moves down through the vertical slit and flows out from the two lower reservoirs attached to two daughter branches as shown in Figure 3.19 and 3.20. The medium from the

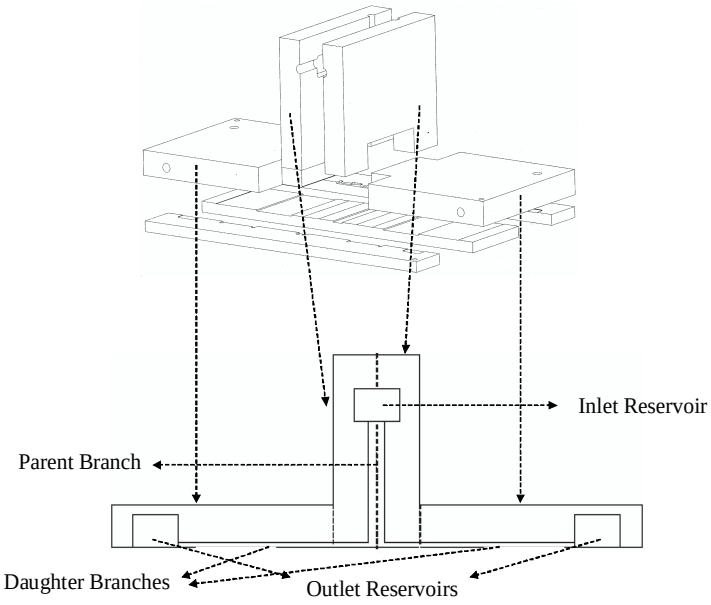

Figure 3.20. T-shaped flow chamber - side cutaway view of parts of constructed chamber.

vertical slit is divided into the two daughter branches. As in the parallel plate flow chamber, there are three slide slots where the endothelial cells on the bottom plate reside (see Figure 3.21); one in the region of the T-junction, the others in the regions of the parallel plates. The cells are supposed to experience two types of shear forces ; constant and unidirectional shear force in the regions of the parallel plates and shear force similar to that found at the apex of the bifurcation in the region of the T-junction. Accordingly, there are two tapering regions on the bottom plate. These regions are devised to obtain two desired wall shear stresses for one experimental run : 15 – 30 $dynes/cm^2$ in the regions of the parallel plates (Test Region I) and 150 – 190 $dynes/cm^2$ in the region of the T-junction (Test Region II) (see Figure 3.21).

3.7.2 Design Methods

To meet the first and second design criteria, the flow characteristics found at the apex of the bifurcation must be qualitatively and quantitatively similar to those at the T-junction

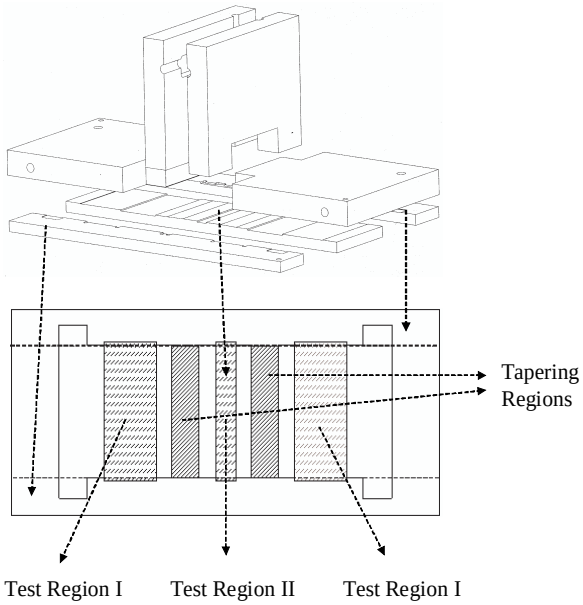

Figure 3.21. T-shaped flow chamber - bottom plate of constructed chamber.

of T-shaped flow chamber. The velocity and pressure fields in a two dimensional T-shaped flow channel are computed to investigate the applicability of our T-shaped flow chamber. The numerical results will demonstrate that the T-shaped flow chamber is an appropriate model to study the response of endothelial cells exposed to shear stress found at bifurcations. Two three dimensional segments of the parallel plates with a reservoir are analyzed numerically to evaluate the third and fourth design criterion. One segment of the parallel plates represents the vertical plate with a reservoir of the T-flow chamber. The other parallel plate represents one half of the horizontal parallel plate of the T-chamber. The vertical and horizontal segments are analyzed numerically to study the effect of the inlet reservoir and outlet reservoir, respectively. Only one horizontal segment is employed to study the effect of the outlet reservoir due to the geometrical symmetry.

Care should be taken to determine the geometrical ratio of the thickness of the parent branch to that of the daughter branch since the ratio plays an important role in generating the

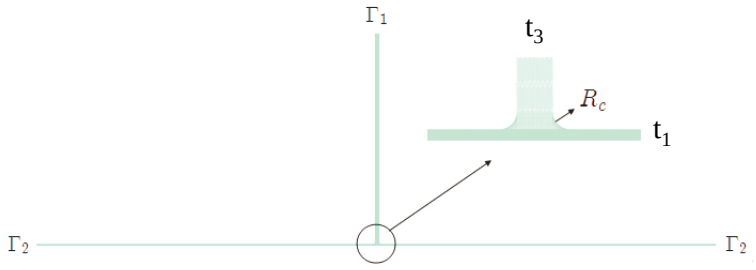

Figure 3.22. Two dimensional model of the T-shaped flow chamber.

flow recirculation at the T-junction. Moreover, the use of the sharp corner at the intersection of the vertical plate and upper horizontal plate can also create a secondary flow at a given flow rate. Prior to the design of a three dimensional T-shaped flow chamber, we pay our attention to the design of the T-junction of a two dimensional T-shaped channel in order to eliminate the flow recirculation in the region of the bifurcation of the T-channel. We also explore the effect of Reynolds number on the flow characteristics found at the T-junction of the T-channel.

3.7.3 Validation of T-shaped flow chamber

3.7.3.1 Numerical Geometry and Dimensionless Parameter.

A two dimensional model of the T-shaped channel is generated in ADINA as shown in Figure 3.22 to design the T-junction. We round the sharp corner that the vertical plate and upper horizontal plates intersect, to avoid vortex generation. The T-channel is then carefully remodeled in sizes of the radius of curvature, R_c, thickness of the parent branch, t_3 and height of the daughter branches, t_1 to eliminate the flow recirculation (see the blow–up

in Figure 3.22). In addition, we employ long enough channels for the parent and daughter branches to obtain approximately fully developed flow at the outer slide region. t_3, t_1 and R_c of the channel are then chosen to be 0.001, 0.0003 and 0.0005 m, respectively. Reynolds number for this study is defined as

$$Re = \frac{\rho t_3 v_{inlet}}{\mu}. \tag{3.11}$$

where ρ is the fluid density, μ is the fluid viscosity and v_{inlet} is the average velocity at the inlet.

3.7.3.2 Numerical Boundary Conditions.

In Figure 3.22, Γ_1 and Γ_2 denote the inlet and two outlets, respectively. At the inlet,Γ_1, uniform velocity is given to obtain a required flow rate and C_2 in Equation 2.8 is set to be zero at the two outlets, Γ_2. This leads nearly fully developed flow at the outlets.

3.7.3.3 Results.

The numerical computation is performed in the range of the Reynolds number $50 \sim 500$. The properties of water are used for this study. The values of ρ and μ of water are 1.0 g/cm^3 and 0.01 g/(cm s) (see,e.g.[50]), respectively at 20^oC and 1 atmospheric pressure. Streamlines in the region the T-junction as shown in Figure 3.23 are smoothly divided into the two daughter branches without generating any flow disturbance. The flow in this carefully chosen model in dimension does not generate the flow recirculation in the bifurcation region even at the highest Re used in this study. Figure 3.24 and 3.25 represent the distributions of axial shear stresses and shear stress gradients found on the bottom plate, respectively. From Figure 3.24, one may conclude that the maximum shear stress (maximum τ) and shear stress found in the region far from the T-junction (asymptotic τ) increase as the Re increases. As the Re becomes smaller, the difference between the maximum shear stress and the asymp-

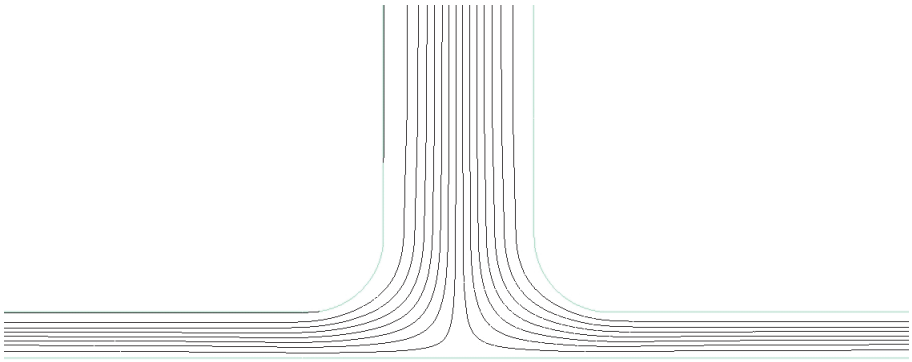

Figure 3.23. Streamlines in the bifurcation region when $Re = 500$.

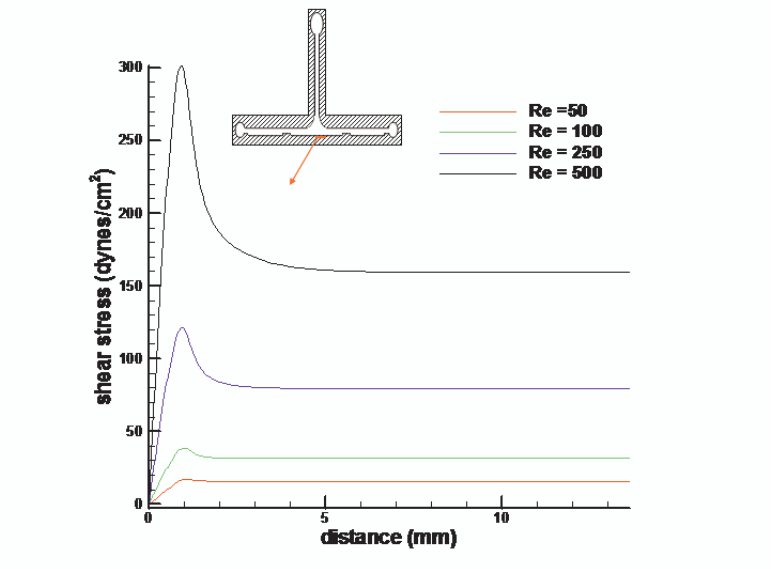

Figure 3.24. Axial shear stress distributions on the bottom plate.

Table 3.5. Re effect on the changes of the point where the maximum shear stress occurs in distance .

Re	Maximum τ (dynes/cm^2)	Asymptotic τ (dynes/cm^2)	Distance from the origin (mm)
50	17.4	15.9	1.04
100	38.6	31.8	1
250	121.55	79.6	0.93
500	301.55	159.2	0.9

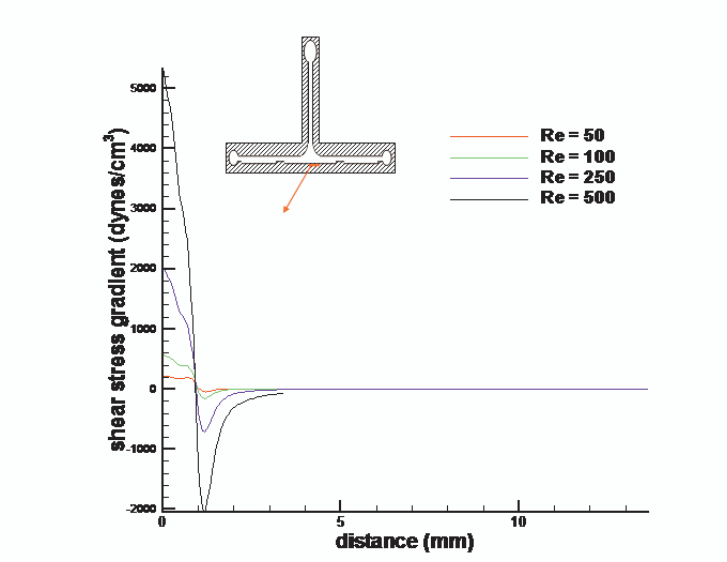

Figure 3.25. Shear stress gradients on the bottom plate.

totic shear stress becomes smaller and the maximum shear stress shifts to the right. Table 3.5 shows these results clearly. It shows the Re effect on the change of the position where the maximum shear stress occurs in distance. One can also see that the changes of shear stress gradients become larger as the Re increases. Moreover, the distance between the origin and region which is free of axial shear stress gradient becomes longer as Re increases, Figure 3.25.

The wall shear stress found at the apex of the arterial bifurcation (Section 3.2) is now compared to the results of the two dimensional analysis on the T-shaped channel. It is shown that comparing the shear stress curve in Figure 3.2 with the shear distributions in Figure

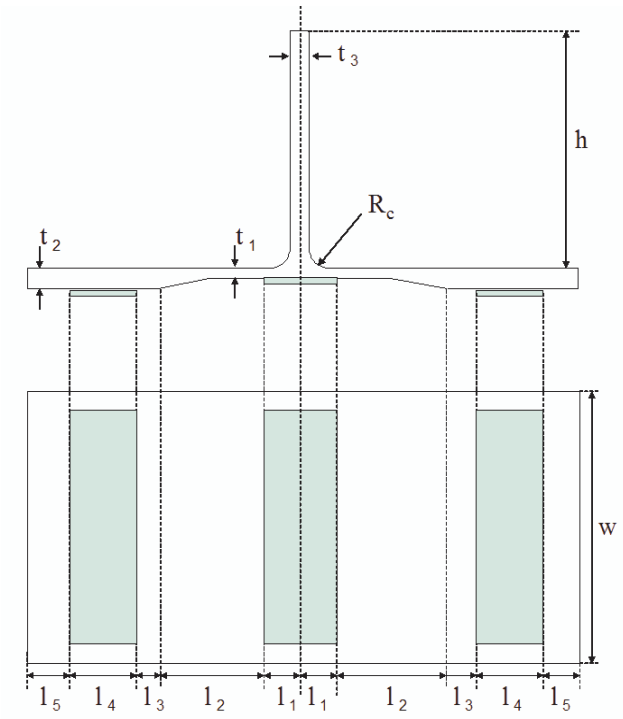

Figure 3.26. Flow region geometry with its dimensions (not drawn to scale).

3.24, the T-shaped channel recreates the qualitative feature of the wall shear stress found at the apex of the bifurcation (criterion 1). The second criterion is also well satisfied since the wall shear stress in both cases are all order of 100 dynes/cm^2 for Re = 250 and 500.

3.7.4 Design of T-shaped Flow Chamber

With the help of the results in Section 3.7.3, we design a three dimensional T-shaped flow chamber. We focus our attention on obtaining the dimensions of flow regions in the T-shaped flow chamber that satisfy all the design criterion discussed in section 3.3. A representative flow region geometry with its dimensions is seen in Figure 3.26. The figure shows all the dimensions of the cross section and bottom plate as well as three slides. In the figure, the radius of curvature, R_c, the thickness of the parent and daughter branches, t_3, t_1 are 0.5, 1 and 0.3 mm respectively. These dimensions are the results of the two dimensional analysis performed in Section 3.7.2. The width of plate, W are same as in the parallel plate flow chamber. The width of slides near the outlet reservoir, l_4 is 38.1 mm. Note that the bottom

Table 3.6. Analysis required to obtain the individual dimension .

Dimension	h	t_2	l_1	l_3	l_5
Analysis	B,C	A	A	A	D

plate is symmetric in the axial direction. In this work, we compute the remaining dimensions shown in the figure using two and three dimensional numerical analysis. In particular, the positions of the three slides and size of the middle slide are determined.

ADINA fluid solver is used again for this analysis. The density and viscosity of water under the temperature and pressure used in typical experimental runs are used. The values of ρ and μ of water are 0.993 g/cm^3 and 0.007 g/(cm s) (see,e.g.[50]), respectively at 37^{o}C and 1 atmospheric pressure. We compute the minimum values in dimension which satisfy all the design criterion by performing the numerical analyses. In Table 3.6, the type of analysis required to obtain the individual dimension is shown. The analysis A though D are explained as follows.

3.7.4.1 Analysis A.

In this analysis, a two dimensional T-shaped model is employed to compute the minimum values of t_2, l_1, l_3. Figure 3.27 shows the two dimensional domain corresponding to the T-shaped model given in Figure 3.26. For numerical boundary conditions, C_2 in Equation 2.8 is set to zero at the two outlets, Γ_2 and a uniform and constant velocity is specified at the inlet, Γ_1 for a required flow rate. The no slip boundary condition is used for the walls.

Along with the first and second design criterion, an additional design requirement is considered to determine t_2. The endothelial cells on the center slide are to be exposed to the corresponding maximum shear stress, about 200 dynes/cm^2 while on the other two slides, the corresponding shear stress in the range of 15 to 30 dynes/cm^2 for a given flow rate. This

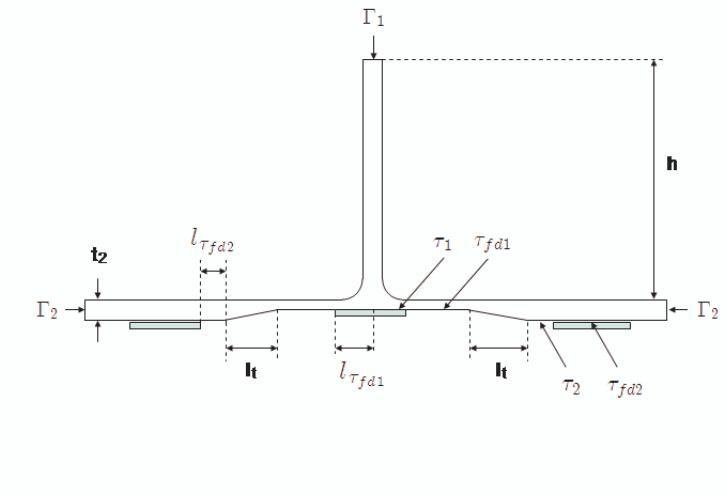

Figure 3.27. Fluid domain and slides for two dimensional T-shaped model, (not drawn to scale).

enables the flow chamber to be used to perform two different types of experiments simultaneously ; one for the response of cells to shear stress found at the arterial bifurcation, the other for the response of cells to shear stress found on the walls of a straight artery. The bottom parallel plates include two tapering regions to satisfy this additional design requirement and the design requirement determines t_2. Note that l_t and l_1+l_2 are chosen to be 1 and 3 cm.

The cells must be contained in the "well defined flow region". The cells on the slides should be exposed to the wall shear stress to satisfy all the design criterion. So to obtain l_1, l_3, the position where the flow becomes nearly fully developed near the T-junction and taper is computed using the following condition.

$$l_\alpha \geq l_{\tau_{fd\alpha}} \quad : \quad 100\,\frac{|\tau_\alpha - \tau_{fd\alpha}|}{|\tau_{fd\alpha}|} \leq \gamma, \tag{3.12}$$

where α represents 1 or 3, $\tau_{fd\alpha}$ is the wall shear stress in the fully developed region and $l_{\tau_{fd\alpha}}$ is the corresponding length that the condition 3.12 is met, respectively. They are all shown

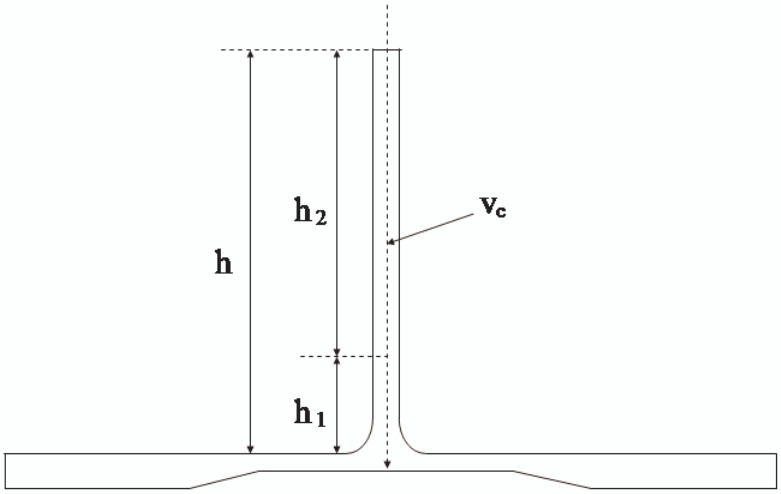

Figure 3.28. T-shaped model showing v_c and h_1, h_2 (not drawn to scale).

in Figure 3.27. τ_α is the wall shear stress found in the region shown in the figure. For a chosen value of γ of 5%, we obtain the minimum values of l_1, l_3 using the equality condition 3.12.

3.7.4.2 Analysis B.

In order to determine the height of the vertical plates h, we have to quantify the entrance effect due to the inlet reservoir which will be studied in Analysis C and the upstream influence of the bifurcation region. In this analysis, the upstream influence of the T-junction is quantified. From the results of Analysis A, the centerline velocities, v_c are obtained and then h_1 shown in Figure 3.28 is found using the following condition.

$$\frac{|v_c - v_{cfd}|}{|v_{cfd}|} \leq \gamma, \tag{3.13}$$

where v_{cfd} is the fully developed centerline velocity. We choose the value of γ of 5%. The value of h_1 is added to h_2 which will be computed in Analysis C to find h.

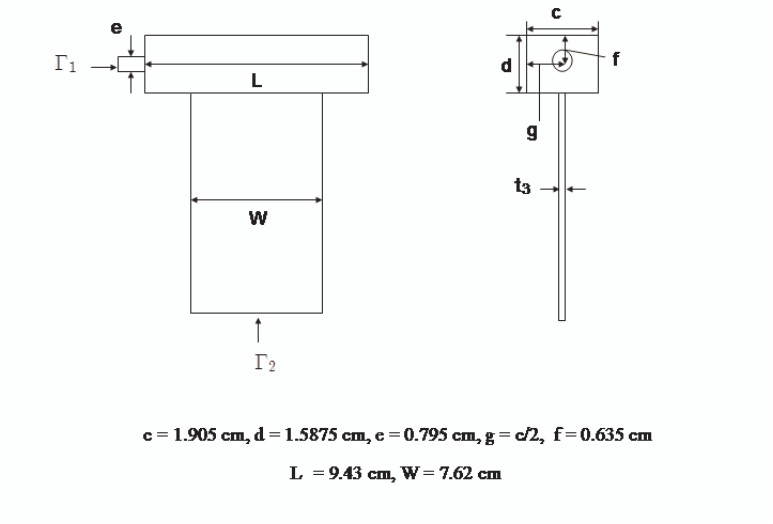

Figure 3.29. Parent branch with the inlet reservoir (not drawn to scale).

3.7.4.3 Analysis C.

In this analysis, the three dimensional model of the vertical plates with the inlet reservoir is used as shown in Figure 3.29 to investigate the entrance effect due to the inlet reservoir. We define h_2 as the minimum length required to avoid the entrance effect. The height h_2 obtained from this analysis (see Figure 3.28) is added to h_1 from Analysis B to determine the minimum length of the vertical plates, h. The dimensions of the inlet opening and reservoir are given in the figure. The boundary conditions used in this model are no slip conditions on the walls, C_2 in Equation 2.8 is set to zero at Γ_2 and C_1 in Equation 2.8 is chosen to obtain the flow rate given in Analysis A at the inlet opening, Γ_1. We again use the condition 3.7 to compute the entrance length, L_{en} and then choose h_2 such that

$$h_2 > L_{en}. \tag{3.14}$$

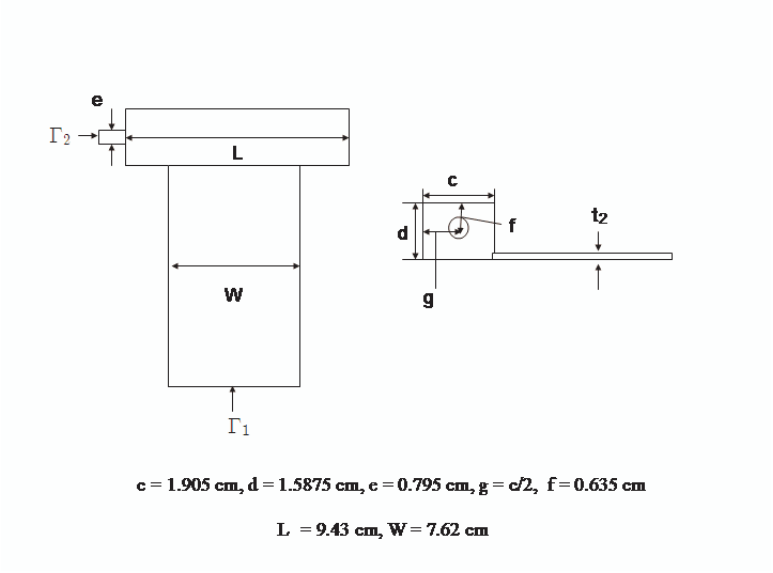

Figure 3.30. Daughter branch with the outlet reservoir (not drawn to scale).

3.7.4.4 Analysis D.

The three dimensional model of the daughter branch with the outlet reservoir is employed to find the exit length, L_{ex} as seen in Figure 3.30. Because of the symmetrical geometry of the horizontal plates in the axial direction, the one half model can represent both the left and right daughter branches. Note that the dimensions of the outlet opening and reservoir are the same as those of the inlet opening and reservoir. C_1 is set to zero at Γ_1 and C_2 is chosen to obtain the required flow rate given in Analysis A. No slip conditions are applied on the walls. As in Analysis C, the condition 3.7 is used to compute L_{ex} and then l_5 is determined using

$$l_5 > L_{ex}. \tag{3.15}$$

3.7.4.5 Results.

Analysis A

According to the previous numerical results of the T-channel (see Figure 3.24), the range of wall shear stress does not drop to the $15 - 30\ dynes/cm^2$ desired in Test Region

Table 3.7. Corresponding shear stresses to four different Re .

Re	142	284	535	583
τ_{max} $(dynes/cm^2)$	29	71	163	183
τ_{∞} $(dynes/cm^2)$	6	11	21	23

Table 3.8. The values of l_1 and l_3 for the corresponding Re .

Re	l_1 (mm)	$l_3(mm)$
142	1.6	1.1
284	2.2	1.1
535	3.5	3.5
583	3.8	4.3

I as the maximum reaches $150 - 190\ dynes/cm^2$ in Test Region II. In addition, for a fully developed flow in infinite parallel plates, the wall shear stress is reversely proportional to the gap of the two parallel plates. Therefore, t_2 is chosen to be twice larger than t_1 to obtain the required τ_w for the two flow regimes. Four different Reynolds numbers are studied ; Re = 142, 284, 535, 583. The highest Re is found to be eligible to obtain the required range of τ_w in the two test regions. Table 3.7 shows the Reynolds numbers and the corresponding wall shear stresses found on the two test regions of the bottom plate. Figure 3.31 illustrates how the wall shear stress behaves on the bottom plate for chambers with a tapered region. The wall shear stress at the bifurcation region of T-chamber has quantitatively and qualitatively similar characteristics to that found at an arterial bifurcation and then, drops to a constant value through the tapering region. As stated earlier, the tapering region plays the role of reducing the magnitude of wall shear stress. l_α is determined by the equality condition, Equation 3.12 for the corresponding Re. The results are listed in Table 3.8.

Analysis B

For Re = 583, the equality condition, Equation 3.13 results in $h_1 = 1.3$ mm.

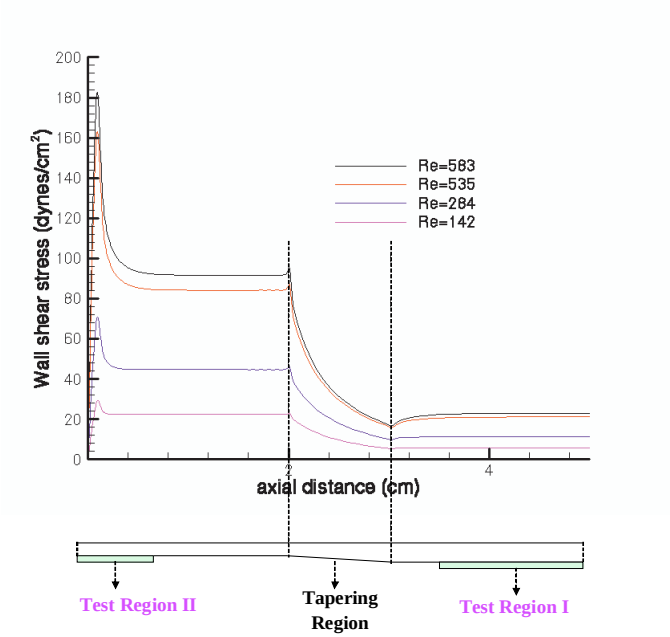

Figure 3.31. Wall shear stress on the bottom plate for four different Re (not drawn to scale).

Analysis C

We employ the mesh densities of the model of parallel plate flow chamber (see Section 3.6) for the current computational domain. The meshed vertical plate with the inlet reservoir is shown in Figure 3.32. In order to find L_{en} for the required range of wall shear stress on the bottom plate of T-chamber, the volume flow rate is calculated from Analysis A and applied to the inlet opening to find C_1. The dimensions of the cylindrical opening and reservoir are same with those of the half model of parallel plate flow chamber (Section 3.6) except the position and thickness of the parallel plate. Applying the equality condition 3.7 results in

$$L_{en} = 42.2mm \quad \text{when} \quad L_w = 0.21cm, \tag{3.16}$$

for the largest Re given in Analysis A. We set $h_2 = L_{en}$ to find the minimum value of h.

Analysis D

The T-shaped flow chamber has a wider gap than the parallel plate chamber. We

Figure 3.32. The meshed body of the vertical plate with an inlet reservoir.

Table 3.9. The dimensions of the flow region geometry .

	t_1	t_2	t_3	R_c	W	h	l_1	l_2	l_3	l_4	l_5
Analysis		A				B,C	A		A		D
Dimensions (mm)	0.3	0.6	1.0	0.5	76.2	43.5	3.8	26.2	4.3	38.1	19.8

adapt the previous half model of parallel plate flow chamber by increasing the gap of the model. We determine the minimum value of l_5. Figure 3.33 shows the meshed model used in this analysis. We evaluate the volume flow rate from Analysis A and then find C_2 for the highest Re given in Analysis A. The equality condition, Equation 3.7 results in

$$L_{ex} = 19.8mm \quad \text{when} \quad L_w = 0.21cm. \tag{3.17}$$

For the minimum value of l_5, we set $l_5 = L_{ex}$.

The dimensions of the flow region geometry from the analyses are listed in Table 3.9. The value of h_1 from Analysis B and h_2 from Analysis C are summed to determine h. These dimensions are the minimum values that we can obtain from the analyses. The T-shaped

Figure 3.33. The meshed body of the horizontal plate with an outlet reservoir.

flow chamber should be designed using these minimum requirements in dimension for the expected shear stress range on the bottom plate of the chamber.

3.7.5 Construction of the T-shaped Flow Chamber

Based on the computational results, we have manufactured the novel T-shaped flow chamber [1]. The flow chamber is composed of seven machined polycarbonate pieces. The chamber requires that three pieces be bonded together to make the bottom plate and four pieces be bonded to make the top plate (see Figure 3.19). The bonding of acrylic and polycarbonate was tested under autoclave and it was found that any air bubbles, inherent in the bonding process, would expand inside the acrylic joint and warp the plastic. Polycarbonate, with its much higher strength, melting temperature, and rigidity did not warp during the autoclaving process. It was also learned that prolonged exposure to ethyl alcohol would cause acrylic to cloud over and in some cases turn brittle. Since ethyl alcohol rinses and autoclaving are the two primary methods of sterilizing the system, polycarbonate became the final choice. Another benefit of polycarbonate was its ability to keep tighter tolerances due to its increased

[1] Andrew Cardine and Bill Kreke, former undergraduate students, performed the assembling process of the T-shaped flow chamber. The flow chamber was machined in the Machine Shop of University of Pittsburgh.

rigidity. This became more important with the T-flow chamber because of the complexity of the seven parts that had to come together to form the chamber.

3.7.5.1 Top Plate.

The top plate (Figure 3.19, see also Figures 3.20) is machined from four pieces of 1.0 inch polycarbonate. These four plates are then bonded together to form one top plate. The top plate is composed of three flow paths, a parent branch and two daughter branches, and three reservoirs, an inlet reservoir and two outlet reservoirs. As stated earlier, the depth of the daughter branches is 0.3 mm. This is a constant depth across the daughter flow path since the necessary expansions are taken care of in the machining of the bottom plate. The parent flow path has a depth of 1.0 mm. 0.5 mm is cut out of each of the uprights that form the inlet reservoir and the parent flow path. At the bottom of the T-junction there is a curved surface of 0.5 mm forming the transition between the parent and daughter branches. There are six ports on the top plate, an entrance port, two exit ports (one for each daughter branch), and three air release ports. The four ports associated with the two outlet reservoirs are 1/4 inch NPT (note that 1/4 inch NPT is much larger than 0.25 inch and is actually a tapered thread). The other two ports lie along a bonded surface. These ports have stainless steel adapters that take the 1/4 inch NPT fitting to a 7/16-20 straight thread. The straight thread eliminates the wedging effect of the NPT fitting at the bonded surface.

3.7.5.2 Bottom Plate.

The bottom plate (Figure 3.19, see also Figures 3.21) for the flow chamber is made of three individual pieces of 0.5 inch polycarbonate. The three pieces are then bonded together to form a single bottom plate. The break lines for the three piece bottom plate are shown as dotted lines in Figure 3.21. To isolate the high shear stress region (150 to 190 $dynes/cm^2$) at the T-junction, a 0.400 $\times$ 3.000 inch slide is used below the T-junction. In order to achieve wall shear stress levels between 15 and 25 $dynes/cm^2$ throughout the rest of the chamber so that a parallel plate control slide 1.500 $\times$ 3.000 inch could be monitored, the 0.3 mm gap

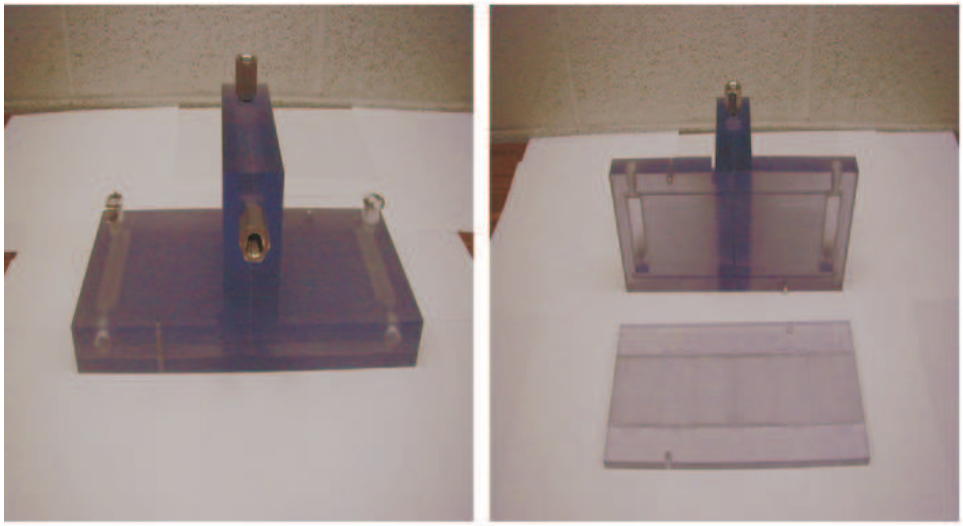

Figure 3.34. T-shaped flow chamber.

had to be expanded to 0.6 mm. The increase was made by ramping the surface shown by the cross-hatching. It is this ramping that requires the plate to be broken into three pieces before assembly.

3.7.5.3 Assembly.

The top and bottom plates are sealed together with an o-ring. The plates will be clamped together to reduce the amount of time that the cultured cells are exposed to uncontrolled conditions. The clamping device should include a base plate to hold the chamber stationary and should apply even pressure around the top plate keeping it firmly locked to the bottom plate. An additional note about the top plate is the need for retaining ridges, which are identified by gray blocks on Figure 3.20. These ridges are necessary to fill in the gap left by the 3.000 inch slides as they go across the 2.750 inch flow path as shown in Figure 3.21. Since the depth of the flow region is 0.6 mm and the top plate flow region is cut to a depth of 0.3 mm, the extra 0.3 mm must be filled by the ridges. Figure 3.34 represents the assembled T-shaped flow chamber.

3.8 Discussion of Results and Future Work

The previous investigation of characteristics of flow at arterial bifurcations showed that wall shear stress found at arterial bifurcation varies along the center neck of the bifurcation. This inhomogeneous characteristic is shown to be closely two dimensional so that we could build a novel flow chamber to test endothelial cells exposed to wall shear fields found at the bifurcations. The T-shaped flow chamber was applicable to investigate the cells exposed to such the wall shear fields since it produces the flow fields quantitatively and qualitatively similar to those found at arterial bifurcations. We devised the T-shaped flow chamber to generate two types of wall shear stress fields ; one found at arterial bifurcations and the other found in straight arteries. This device could enable us to expose the cells to two different wall shear stress fields simultaneously during one experimental run.

Prior to the construction of the T-shaped flow chamber, the numerical design of T-shaped flow chamber was carefully performed satisfying all the design criteria. These criteria were taken account because the chamber must produce the "well defined flow" to test the cells. The consideration of this "well defined flow" was made since the novel flow chamber should recreate the qualitative and quantitative features of wall shear stresses found at arterial bifurcations, and the test cells must be grown in the confined region beyond the region governed by inertial and lateral wall effects. The inertial effects generated by the inlet and outlet reservoirs of the chamber and lateral wall effects could be quantified analytically and numerically. However, determining the size of the test region by quantifying these effects was dependent on the choice of a certain value of γ given in Equation 3.7. We chose γ of 5%. If this is a conservative choice, let us consider L_w, L_{en} and L_{ex} in the parallel plate flow chamber using larger values of γ. Figure 3.10 included the dependence of β on $\tilde{L}_w$ for the choice of γ of 10% and 20%. As shown in the figure, larger values of γ results in smaller $\tilde{L}_w$. From the numerical analysis, we found that increasing the value of γ to 10% and 20% lowered L_{en} and L_{ex} by 75–80% and 87–99%, respectively compared to the results of the choice of

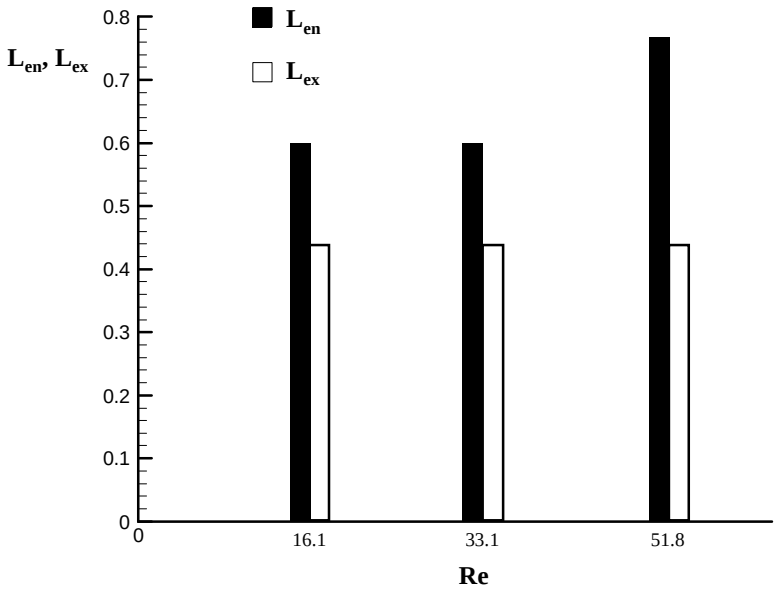

Figure 3.35. Dependence of L_{en} and L_{ex} (in cm) on Reynolds number for $L_w = 0.031cm$ and Re = 16.1, 33.1, 51.8 ($\tau_{fd_{2D}} = 15.0, 30.1, 48.0 dynes/cm^2$) when $\gamma = 10\%$.

γ of 10% as shown in Figures 3.35 and 3.36. These results imply that a chosen value of γ determines the size of ATR. Therefore, it is critical for us to know a value reasonable based on the experimental error that found in most studies. However, the value is not currently available and so, we made a conservative choice for γ.

The parallel plate flow chamber was built and tested in our laboratory. The T-shaped flow chamber was also manufactured but has not been tested yet. For future work, we plan to add a step to the T-chamber to recreate the flow circulation found in the outer walls of bifurcations. To do this a drop will be created inside the chamber after the fluid leaves the T-junction. This will enable us to simultaneously run tests to compare endothelial cell response to flow at the apex of bifurcations, outer walls of bifurcations and straight segment of arteries. This is particularly important since many genetic tests provide a relative, not an absolute number.

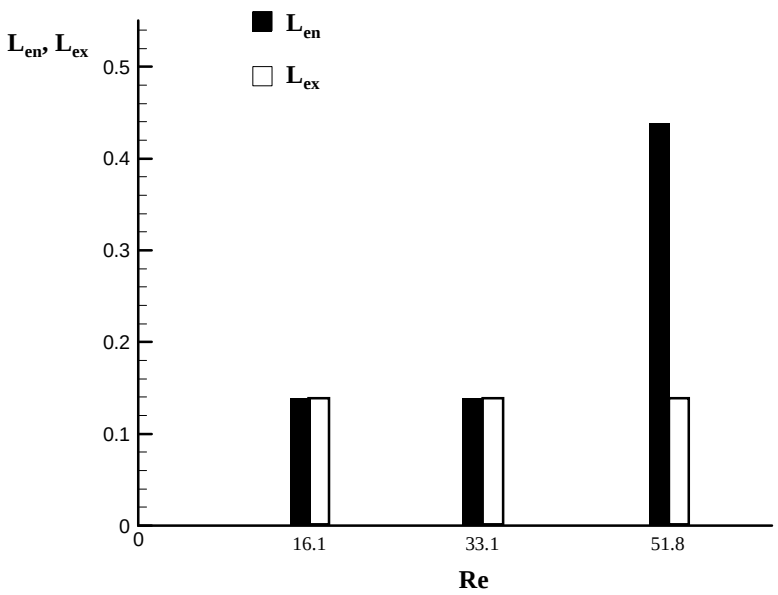

Figure 3.36. Dependence of L_{en} and L_{ex} (in cm) on Reynolds number for $L_w = 0.031cm$ and Re = 16.1, 33.1, 51.8 ($\tau_{fd_{2D}} = 15.0, 30.1, 48.0 dynes/cm^2$) when $\gamma = 20\%$.

J.A. Frangos *et al*. reported that temporal shear gradients are important factors for endothelial cell proliferation and gene expression.[33,34] The sudden or ramped onset of flow with step, impulse, ramped transient or ramped type of flow profile has been shown to affect cell proliferation and gene expression in their studies. Hence, as future work, transient analysis on the flow chamber can also be made numerically to test endothelial cells under unsteady loading conditions.

4.0 THE MATHEMATICAL MODELING OF THE MOTION OF VESSEL WALLS

4.1 Objectives

The periodic motions of arterial walls are typically modeled as linearly elastic[140,145,146] since the radial deformation by pulsatility is relatively small. *In vivo* arteries are preloaded by prestretch and a base pressure (100 $mmHg$), a large deformation. Arterial walls preloaded by these deformations are also loaded with an oscillatory pressure waveform. The strain due to the preloadings are reported to be large compared to the oscillatory deformation.[114,136] Hence we can model the periodic motions of vessel walls as small deformations superposed on large deformations using a small on large theory. The mathematical and numerical analyses of the vessel wall behavior are however very expensive since *in vivo* vessel geometry is not simple. We employ a simple geometry : a straight cylindrical tube as the unloaded reference configuration. Here we address the separate roles of elastin and collagen fibres, the importance of including prestretch and the nonlinear characteristics of the wall in describing the motion of vessel walls.

Arteries are composed of three layers: the intima, the media and the adventitia (e.g.[127,128]). The intima is the innermost layer and its main components are endothelial cells and a thin basal membrane. The endothelial cells act as a mechanical transducer to transmit the signal to the media as a result of shear stress and pressure arising from blood flow.[129] The media consists of smooth muscle cells, elastin and collagen fibrils. On the other hand, the adventitia is the outermost layer of the artery and composed mainly of wavy collagen fibrils with admixed elastin, nerves, fibroblasts and the vasal vasorum. To investigate the functions of fibrils, most studies have been performed in *in vitro* experiments using arteries excised from autopsy.[112,118,119,125,126,152] The behavior of arteries *in vivo* are influenced by pulsatile transluminal pressure, axial force, chemical hormones and nervous control and therefore, *in vivo* investigations of the mechanical behavior of arteries are very limited.[116]

Previous mechanical tests of arteries under static biaxial loading[130] or static uniform inflation with an axial extension[112,118,119,125,126,152] after pre–conditioning showed that the vessel exhibits a highly nonlinear stress–strain relationship. Additionally, in a pressure–radius curve, the slope becomes larger as the internal pressure increases. M.R. Roach and A.C. Burton isolated the roles of elastin and collagen fibers on the mechanical function of arteries by using formic acid (to degrade collagen) and trypsin (to degrade elastin).[112] They reported that the elastin fibers dominate the mechanical function at lower levels of pressure and adversely, at a higher level of pressure the collagen fibers dominate the function. Accordingly, the stability and integrity of arteries under the pulsatile loading condition are preserved by the collagen fibers since the arterial wall stiffens at a higher level of pressure. The smooth muscle cells also contribute to the mechanical function but have been understood not to play the major role in the passive state of arteries.[112,113]

The significance of prestretch and residual stress has been reported by many authors (e.g.[114,116,120,125,144]). *In vivo*, arteries are axially prestretched and therefore, the arteries retract axially when cut cross sectionally. The amount of axial retraction differs in various types of vessels in the arterial tree. It has been reported that the ratio of the *in vivo* length to the retracted length is between 1.1 to 1.6.[114,116,131] In addition, the vessels have been shown to be under circumferential stress even when unloaded. In particular, when a longitudinal cut is made on the unloaded arterial segment, the arteries retract circumferentially forming an open sector. The circumferential retraction has been known to occur due to the residual stress. It has been reported that the incorporation of the residual stress slightly softens the material of the artery.[116]

Based on the continuum theory of hyperelastic materials, various strain energy functions for arteries have been developed (e.g.[116,120,132,133]). Most of the arteries have close to a cylindrical shape and remain the same shape even after they are excised at autopsy.

Accordingly an infinite cylindrical tube with a thin or thick wall is taken as a domain for analytical analyses based on finite deformation. As stated earlier, arteries are under both axial and intramural pressure forces. As just mentioned, even unloaded arteries are not stress free bodies and have residual stress. Several authors have accounted for the prestretch and residual stress.[116,120] G.A. Holzapfel *et al.* included an additional torsional force related to the residual stresses.[116] They constructed the constitutive equations for the strain energy for both the media and adventitia considering the role of collagen fibers, taking the strain energy as a linear combination of isotropic and anisotropic components.

Even though the mathematical analysis of vessel wall motion by large deformations including the roles of fibrils and the effects of prestretching and residual stress has been performed by many authors, the behavior of healthy arterial walls is typically modeled as linearly elastic in the analysis of vessel wall motion under physiological loading conditions (e.g.[140,145,146]). This is motivated by the fact that the pressure waveform that propagates down the vessel results in a relatively small deformation. In particular, the radial strain is usually smaller than 0.1.[136] Underlying this linear analysis is the assumption that the unloaded reference configuration is that found at the average physiological pressure *in vivo*. Hence, this analysis does not account for axial prestretch, which has been shown to be on the order of 1.1–1.6[114,116,131] or for the radial distension associated with the base or average pressure, which is for example, approximately 100 $mmHg$ for ascending or descending aortas.[114,136] In addition the separate roles of the elastin and collagen fibrils are not taken account in these analysis.

The hypothesis underlying this work is that the axial loading and pressure loading (prestretch and average pressure loading) that a vessel experiences play an important role in the mechanical response of the vessel and warrant a nonlinear analysis of the vessel motion that includes these loadings. Other researchers have already noted the importance of this prestretch.[114,116,120,125] In this work, both the axial stretch and radial extension by aver-

age pressure loading will be considered as large deformations. The periodic motion of the artery will then be included as a small deformation superposed on these large deformations using a small on large theory.[115] The arterial wall motion is governed mainly by both elastin and collagen fibers with negligible contributions of smooth muscle cells (muscular inactive behavior) in the media.[112,113] Collagen recruitment has been considered previously by other researchers, (see, e.g.[116]). A mathematical model accounting separately for the role of the elastin and collagen including the effect of collagen fiber recruitment will be developed through an extension of a multi-mechanism theory that has previously been applied to cerebral arteries.[137–139,141–143]

The specific aims of this research are therefore, described as follows:

1. Based on the continuum theory of multiple mechanisms,[137–139] further develop a constitutive equation of the arterial wall that separately accounts for the role of the elastin and collagen, including the effect of collagen fiber recruitment. The quantitative values for the parameters in the multi-mechanism model will be obtained from the experimental pressure–radius curve which includes prestretch given in.[114] Significantly, when analyzing this data, the unloaded reference configuration will be chosen to correspond to the unloaded vessel wall (prior to prestretch and the radial distension associated with the base or average pressure),

2. An investigation of the motion of the arterial wall will then be made to describe the oscillatory wall motion due to pulsatile flow in arteries using a small on large theory[115] for the multi-mechanism constitutive equation developed in Specific Aim 1. The central ideas is that the oscillatory motion arising from the pulsatile arterial waveform is small and will be superposed on the large deformation corresponding to axial prestretch and radial inflation due to the average pressure in the vessel. This analysis will be performed for a cylindrical tube of finite thickness.

The assumptions underlying this work are

1. Only axisymmetric arteries of constant radius are considered. Therefore the current work will not be applicable to non–axisymmetric arterial segments such as bifurcations or segments with substantial sclerotic changes. This work can be generalized to include other geometries though the finite deformations in the small on large theory will need to be solved computationally.

2. The arterial media is assumed to be homogeneous. The media of artery is historically heterogeneous.[117] However, according to P.B. Dobrin[118] the media was found to act mechanically as a homogeneous material.

3. The arterial wall is assumed to be an incompressible material. Earlier experimental studies of incompressibility of the arterial wall showed that under physiological conditions of both internal pressure and longitudinal stretch an incompressible assumption is justified.[119]

4. According to the theory of multiple mechanisms, a microstructural change is associated with a certain deformation parameter and is referred to a scalar kinematic parameter s. Therefore, there is an activation criterion for collagen recruitment, s_a. Here we assume that all of the collagen fibers have the same activation criterion. This assumption can be relaxed using an integral model if experimental data warrants this increased complexity.

5. In use of the dual mechanism theory, two types of strain energies are used to model the experimental data curve. For each of these strain energy functions the material is assumed to be isotropic. The proposed model can be extended to anisotropic materials, (see, e.g.[116]).

6. The significance of the residual stress in the arterial wall has been discussed by many authors.[116,120,121] A cylindrical tube with an opened angle was therefore taken as a

stress–free body. The aim of this research is to study the effect of prestretch and the role of the dual mechanisms. This effect can be considered in a future work.

4.2 Pressure–Radius Curve for the Descending Aorta of A Dog

Only recently has a quantitative model including recruitment of collagen fibers in the mechanical behavior of arterial walls been formulated using a multi-mechanism theory,.[141–143] However, this model was directed at cerebral arteries and in addition, did not take into account the effects of prestretch. Atabek *et al.* provided detailed information on the mechanical behavior of the descending aorta of a dog[114] which makes an extension of this multi-mechanism model to include prestretch possible. In their article, the effect of prestretch is considered. A distinguishing feature is that pressure–radius curves merge to a single line for all tested axial stretching ratios after collagen recruitment. One focus of this research is to use this data to extend the work of[141–143] to include prestretch and to apply this formulation to noncerebral arteries. We summarize the pressure–radius curve given in[114] below.

Shown in Figure 4.1 is the typical pressure–radius curve for the descending aorta of a dog.[114] In the figure h_o, R_o and l_o are the initial thickness, inner radius and length of an undeformed configuration, respectively and $\bar{p}$ is the systemic pressure, 100 $mmHg$. The defined dimensionless parameters λ_1 and λ_2 are

$$\frac{l}{l_o} \equiv \lambda_1, \qquad \frac{R}{R_o} \equiv \lambda_2 \tag{4.1}$$

where l and R are the length and inner radius of a current configuration, respectively.

According to,[114] the *in vivo* artery is axially prestretched by the amount of $\lambda_1 \approx 1.4$ before pressure loading so that λ_2 is approximately 0.85 under initial longitudinal strains at $p/\bar{p} = 0$. The artery was loaded by a uniform pressure after being stretched axially by three

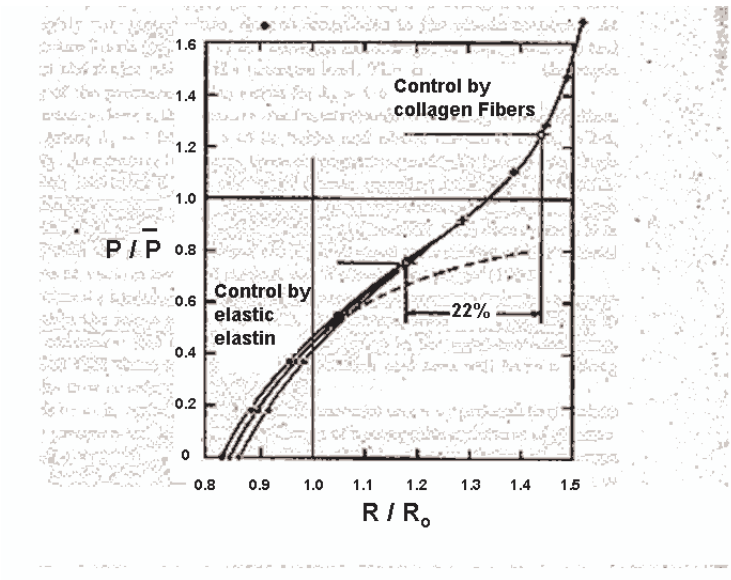

Figure 4.1. Typical pressure-radius curve for the descending aorta of a dog [114].

different values of λ_1. When the value of λ_1 for prestretch is 1.35, the value of λ_2 is larger than 0.85 at $p/\bar{p} = 0$ and inversely, when $\lambda_1 = 1.45$, λ_2 is smaller than 0.85 at $p/\bar{p} = 0$ since larger prestretch results in smaller diameter of the vessel before pressure loading.

The curve in the figure has an inflection point. Up to $p/\bar{p} = 0.6$ the slope of the curve decreases as pressure increases. It is reported that arteries are controlled by highly elastic elastin lamellae, showing a nonlinear "ballooning effect" up to this level of pressure.[114] For $p/\bar{p}$ greater than approximately 0.6 the slope increases linearly, inflects smoothly and rises exponentially with the increment of pressure. This steep increase of the slope is believed to be due to the contribution of collagen fibers. It is also reported that the collagen fibers begin to straighten out at a certain pressure value larger than $p/\bar{p} = 0.6$.[114]

The curves of $\lambda_1 = 1.35$, 1.4 and 1.45 merge to a single curve for approximately $\lambda_2 \geq 1.25$. Note that pulsatility of pressure is between 0.75 and 1.25. This corresponds to deviation of 10 % of λ_2 about the mean.

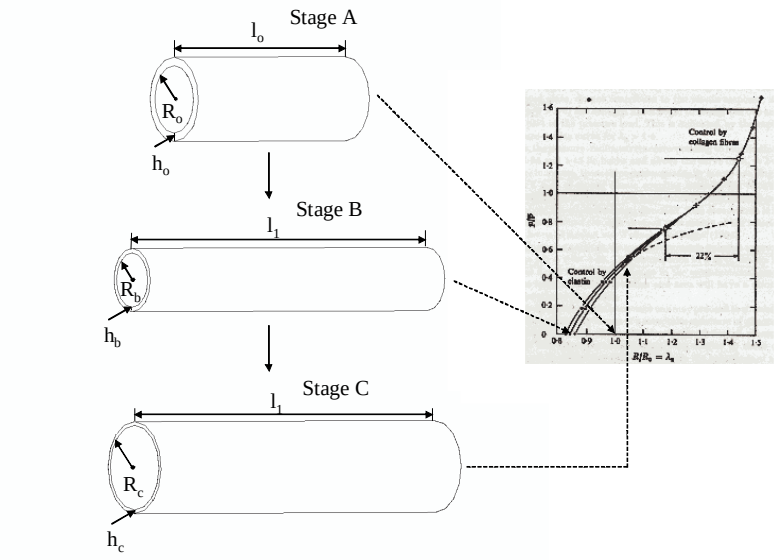

Figure 4.2. Deformation stages according to the pressure-radius curve.

4.3 Mathematical Analysis to Fit the Experimental Data

4.3.1 Deformation Stages According to the Pressure–Radius Curve

We consider deformation stages according to the pressure–radius curve. In Figure 4.2, the pressure-radius curve has three stages A, B and C. Three cylindrical tubes corresponding to these stages are also shown in the figure to simplify discussion of the deformation history due to the stretching and pressure forces acting on the artery. At Stage A, we have an undeformed initial configuration. Both the extension and inflation ratios λ_1 and λ_2, respectively begin with the value of 1. Therefore, a magnitude of axial stress, σ is zero in this stage. The artery is then stretched and reaches Stage B. The initial inner radius and thickness of the artery, R_o and h_o change to R_b and h_b, respectively by the amount of λ_1 larger than 1. In this stage, the pressure is not yet applied however, λ_2 is less than 1 due to the extension and therefore, σ is not zero. At Stage C, a uniform pressure force normal to the surfaces of the artery starts to act on the surfaces, while the length of the segment l is held fixed. Then R_b and h_b change to R_c and h_c, respectively. In this stage, starting with λ_2 less than 1, λ_2 reaches 1 and becomes larger than 1 as the pressure force increases.

As previously stated, collagen fibres become load bearing at a certain pressure level. Before collagen fibres begin to straighten out, the motion of arterial walls is governed purely by elastic elastin lamellae. In order to model such characteristics of motion of arterial walls, a muti mechanism theory is used in this study. According to the theory, a microstructural change is associated with a certain deformation parameter and is referred to a scalar kinematic parameter s. Therefore, there is an activation criterion for collagen recruitment, s_a. We assume that there is a single value of s_a throughout of the material.

4.3.2 Dual Mechanism Constitutive Model

Using previous work on dual mechanism models for arteries, we consider the stress–free body to correspond to an arterial segment excised from autopsy. The excised artery is idealized as an axisymmetric cylindrical tube. It is then subjected to both axial stretch and pressure forces. The first mechanism is the elastin and the second mechanism corresponds to the collagen. The unloaded configuration of the elastin corresponds to the unloaded configuration of the arterial wall. Significantly, the unloaded configuration of the collagen is different than that for the elastin. As will be discussed below, and explained in detail in,[141–143] the reference configuration at which collagen recruitment begins depends on an activation criterion. At the early loading stage, the elastin fibers dominate the motion. The motion is described as the motion of a particle in an initial configuration, κ_1 to a current configuration, κ governed by

$$\mathbf{x} = \chi_{\kappa_1}(\mathbf{y}, t), \tag{4.2}$$

as seen in Figure 4.3. Mechanical response of the material due to collagen is dependent on the stretch of the collagen relative to the unloaded configuration, κ_2. The motion is described as the motion of a particle in the newly introduced configuration, κ_2 for collagen recruitment

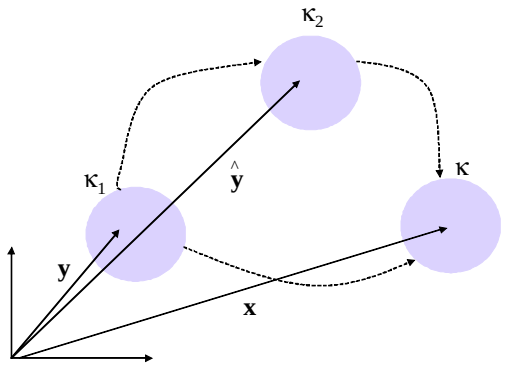

Figure 4.3. Kinematics of dual mechanisms.

to a current configuration, κ governed by

$$\mathbf{x} = \chi_{\kappa_2}(\hat{\mathbf{y}}, t), \tag{4.3}$$

as also seen in Figure 4.3. The motion of a particle in the initial configuration, κ_1 to the newly introduced configuration, κ_2 is governed by

$$\hat{\mathbf{y}} = \chi_{\kappa_1}(\mathbf{y}, t_2), \tag{4.4}$$

where t_2 is the time at which the κ_2 is achieved. As stated in the assumptions, the collagen recruitment is associated with a scalar kinematic parameter s expressed as

$$s = A(F_{ij}), \tag{4.5}$$

where F_{ij} is the components of deformation gradient tensor.

$$F_{ij} = \frac{\partial x_i}{\partial y_j}. \tag{4.6}$$

For isotropic and incompressible materials, s can be written as a function of the first and second invariants of

$$s = s(I_1, I_2). \tag{4.7}$$

$s(I_1, I_2)$ is chosen such that $s = 0$ when $t = t_1$ at which the body is rest. The activation of the second mechanism is defined as

$$A_a = s(I_1, I_2) - s_a = 0, \tag{4.8}$$

where s_a is the initiation value of collagen recruitment. Likewise, if the loading is of sufficient magnitude, such that a second activation criterion is met, s_b, the elastin will rupture. So, s_b can be also taken account for elastin breakage when

$$A_b = s(I_1, I_2) - s_b = 0. \tag{4.9}$$

Three stages for a loading condition are considered depending on the value of s.

1. $0 \leq s < s_a$

   s starts at zero and increases before it reaches s_a. In this stage, only the elastin contributes to the motion of the arterial walls. The Cauchy stress tensor, $\mathbf{T}$ is only a function of $\mathbf{F}$.

2. $s_a \leq s < s_b$

   When s reaches s_a collagen fibres begin to straighten out. So, in this stage, both elastin and collagen fibres play a role in deformation of the arterial wall. The Cauchy stress tensor, $\mathbf{T}$ is then a function of $\mathbf{F}$ and $\hat{\mathbf{F}}$ where

$$\hat{F_{ij}} = \frac{\partial x_i}{\partial \hat{y}_j}. \tag{4.10}$$

3. $s \geq s_b$

   At $s = s_b$ all of the elastin break simultaneously. The arterial wall motion is governed by only collagen fibres in this stage. The Cauchy stress tensor, $\mathbf{T}$ is then only a function of $\hat{\mathbf{F}}$.

In order to take into account the roles of both the fibers in the second stage, the strain energy for the stage is a linear combination of two types of strain energy functions; one responsible for the elastin and the other for the collagen fibers. In the third stage, the strain energy is due to that for the collagen fibers alone. Therefore, the constitutive relation is a different type at each stage. The following constitutive relation can be proposed for hyperelastic, homogenous, isotropic and incompressible materials to model the motion of arterial walls using the mathematical notation referred to in;[135]

$$\tau^{ij} = pG^{ij} + \Phi g^{ij} + \Psi B^{ij} + \hat{\Phi}\hat{g}^{ij} + \hat{\Psi}\hat{B}^{ij}, \tag{4.11}$$

where

$$\Phi = 2\frac{\partial W}{\partial I_1}, \quad \Psi = 2\frac{\partial W}{\partial I_2}, \tag{4.12}$$

$$\hat{\Phi} = 2\frac{\partial W}{\partial \hat{I}_1}, \quad \hat{\Psi} = 2\frac{\partial W}{\partial \hat{I}_2}, \tag{4.13}$$

with

$$W = \begin{cases} W(I_1, I_2) & \text{if} \quad 0 \leq s < s_a; \\ W(I_1, I_2) + \hat{W}(\hat{I}_1, \hat{I}_2) & \text{if} \quad s_a \leq s < s_b; \\ \hat{W}(\hat{I}_1, \hat{I}_2) & \text{if} \quad s \geq s_b. \end{cases} \tag{4.14}$$

s_a and s_b can be determined using

$$s = I_1 - 3. \tag{4.15}$$

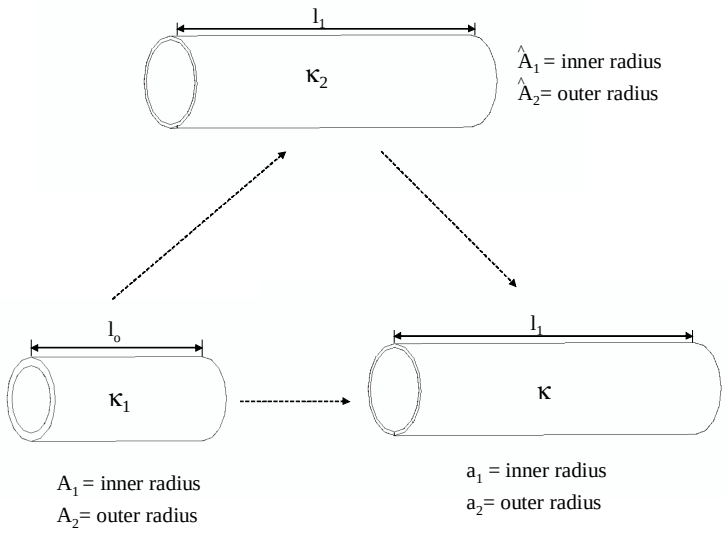

Figure 4.4. Motion of arterial walls by dual mechanisms.

In Equation 4.11, p is the Lagrange multiplier, G^{ij} is the contravariant components of metric tensor in κ, g^{ij} is the contravariant components of metric tensor in κ_1, $\hat{g}^{ij}$ is the contravariant components of metric tensor in κ_2, B^{ij} is the contravariant components of tensor associated with the first invariant I_1, g^{ij} and G_{ij} and $\hat{B}^{ij}$ is the contravariant components of tensor associated with the first invariant $\hat{I}_1$ in κ_2, $\hat{g}^{ij}$ and G_{ij}, respectively.

We now consider a homogeneous deformation of both extension and inflation of a cylindrical tube. Figure 4.4 shows the motion of arterial walls categorized by the three stages. The motion from the initial configuration, κ_1 to the current configuration, κ can be solved using the strain energy shown in the first equation in Equation 4.14. Therefore, in the first stage, only elastin plays a role in the motion. For the second stage the motion from the configuration, κ_2 to the current configuration, κ is considered. In this stage, the strain energy includes two terms ; one term for elastin part, the other term for collagen recruitment (see the second equation in Equation 4.14). According to the pressure–radius curve in Section 4.2, there is no elastin breakage so, we do not consider Stage III in this study.

We define

$$\lambda_2 = \frac{a_1}{A_1}, \quad \lambda_{2a} = \frac{a_1}{\hat{A}_1}, \tag{4.16}$$

where A_1 and a_1 are the initial and current inner radius respectively, $\hat{A}_1$ is the inner radius in the configuration, κ_2. We can then find λ_{2a} through

$$\lambda_2 = \lambda_{2a}|_{s=s_a} \quad \text{for} \;\; A_a = 0, \tag{4.17}$$

where $\lambda_{2a} > 1$. Therefore, Stage I and Stage II can be recategorized through λ_{2a} as follows;

- $1 \leq \lambda_2 < \lambda_{2a}$

  Strain energy accounting for elastin is $W = W(I_1, I_2)$ in this stage.

- $\lambda_{2a} \leq \lambda_2 < \lambda_{2b}$

  Strain energy for both elastin and collagen recruitment is $W = W(I_1, I_2) + \hat{W}(\hat{I}_1, \hat{I}_2)$ in this stage.

In order to model the data in Stage I, we use a strain energy function corresponding to the Neo–Hookian model defined as

$$W = C_1(I_1 - 3), \tag{4.18}$$

where C_1 is a material constant. The strain energy function for an exponential model defined as

$$\hat{W} = \frac{\alpha}{2\gamma} e^{\gamma(\hat{I}_1 - 3)}, \tag{4.19}$$

where α, γ are all material constants is linearly combined with the strain energy in Stage I (see Equation 4.18) to fit the data in Stage II.

4.3.3 Classical Solutions of the Extension and Inflation of A Cylindrical Tube

4.3.3.1 Stage I ($\lambda < \lambda_a$).

We consider the motion from the configuration κ_1 to κ. The cylindrical coordinate(r, θ, z) is used to define the motion from the body B_o in κ_1 to the body B in κ as

$$y_1 = \rho(r)cos\theta, \quad y_2 = \rho(r)sin\theta, \quad y_3 = z/\lambda_1 \quad \text{for } B_o, \tag{4.20}$$

$$x_1 = rcos\theta, \quad x_2 = rsin\theta, \quad x_3 = z \quad \text{for } B. \tag{4.21}$$

Metric tensors for the body B_o can be found as

$$g_{ik} = \frac{\partial y^m}{\partial \theta^i}\frac{\partial y^m}{\partial \theta^k}, \tag{4.22}$$

$$g^{ik} = \frac{\partial \theta^i}{\partial y^m}\frac{\partial \theta^k}{\partial y^m}, \tag{4.23}$$

so that

$$[g_{ik}] = DIAG\left[\rho'(r)^2,\ \rho(r)^2,\ \frac{1}{\lambda_1^2}\right], \tag{4.24}$$

$$[g^{ik}] = DIAG\left[\frac{1}{\rho'(r)^2},\ \frac{1}{\rho(r)^2},\ \lambda_1^2\right], \tag{4.25}$$

where $'$ stands for $\partial()/\partial r$ and θ^i are r, θ, z when $i = 1, 2, 3$. Metric tensors for the body B are

$$G_{ik} = \frac{\partial y^m}{\partial \theta^i}\frac{\partial y^m}{\partial \theta^k}, \tag{4.26}$$

$$G^{ik} = \frac{\partial \theta^i}{\partial y^m}\frac{\partial \theta^k}{\partial y^m}, \tag{4.27}$$

so that

$$[G_{ik}] = DIAG\ \left[1,\ r^2,\ 1\right], \tag{4.28}$$

$$[G^{ik}] = DIAG\ \left[1,\ \frac{1}{r^2},\ 1\right], \tag{4.29}$$

To satisfy incompressibility condition,

$$I_3 = \frac{G}{g} = 1, \tag{4.30}$$

where G and g are

$$G = |G_{ik}| = r^2, \tag{4.31}$$

$$g = |g_{ik}| = \frac{\rho'(r)^2\rho(r)^2}{\lambda_1^2}. \tag{4.32}$$

Therefore,

$$\frac{\rho'(r)^2\rho(r)^2}{\lambda_1^2} = r^2. \tag{4.33}$$

This results in

$$\rho(r) = \sqrt{\lambda_1 r^2 + C}. \tag{4.34}$$

We now apply initial conditions which are

$$A_1 = \rho(a_1), \quad A_2 = \rho(a_2). \tag{4.35}$$

Then applying Equation 4.34 to 4.35 yields

$$\rho(r) = \sqrt{\lambda_1 r^2 + A_1^2 - \lambda_1 a_1^2}. \tag{4.36}$$

We then find three invariants using the metric tensors as follows ;

$$I_1 = g^{rs}G_{rs} = \frac{1}{\rho'(r)^2} + \frac{r^2}{\rho(r)^2} + \lambda_1^2, \tag{4.37}$$

$$I_2 = G^{rs}g_{rs}I_3 = \rho'(r)^2 + \frac{\rho(r)^2}{r^2} + \frac{1}{\lambda_1^2}, \tag{4.38}$$

$$I_3 = 1. \tag{4.39}$$

Using the first invariant, we calculate B^{ij} which is defined as

$$B^{ij} = I_1 g^{ij} - g^{ir}g^{js}G_{rs}, \tag{4.40}$$

so that

$$[B^{ij}] = DIAG\left[\frac{r^2}{\rho(r)^2\rho'(r)^2} + \frac{\lambda_1^2}{\rho'(r)^2},\ \frac{1}{\rho(r)^2\rho'(r)^2} + \frac{\lambda_1^2}{\rho(r)^2},\ \frac{\lambda_1^2}{\rho'(r)^2} + \frac{\lambda_1^2 r^2}{\rho(r)^2}\right]. \tag{4.41}$$

Then, the components of Cauchy stress tensor can be written as

$$\tau^{ij} = \Phi g^{ij} + \Psi B^{ij} + pG^{ij}, \tag{4.42}$$

so that using g^{ij}, G^{ij}, B^{ij} we can obtain the stress tensor as follows ;

$$\begin{aligned}[\tau^{ij}] = DIAG\,[&\frac{1}{\rho'(r)^2}\Phi + \left(\frac{r^2}{\rho(r)^2\rho'(r)^2} + \frac{\lambda_1^2}{\rho'(r)^2}\right)\Psi + p, \\ &\frac{1}{\rho(r)^2}\Phi + \left(\frac{1}{\rho(r)^2\rho'(r)^2} + \frac{\lambda_1^2}{\rho(r)^2}\right)\Psi + \frac{p}{r^2}, \\ &\lambda_1^2\Phi + \left(\frac{\lambda_1^2}{\rho'(r)^2} + \frac{\lambda_1^2 r^2}{\rho(r)^2}\right) + p]\end{aligned} \tag{4.43}$$

With a negligible gravity force, the equilibrium equations take the form

$$\tau^{ik}||_i = 0, \tag{4.44}$$

where || represents the differentiation of the second order tensor in the current configuration. These can be rewritten in terms of the second Christoffel symbols in

$$\tau^{ik}_{,i} + \Gamma^{i}_{ir}\tau^{rk} + \Gamma^{k}_{ir}\tau^{ir} = 0. \tag{4.45}$$

The second Christoffel symbols are defined as

$$\Gamma^{k}_{ir} = \frac{\partial^2 y^m}{\partial\theta^r \partial\theta^i}\frac{\partial y^m}{\partial\theta^l}G^{kl}, \tag{4.46}$$

so that we can obtain

$$\Gamma^{1}_{22} = -r, \quad \Gamma^{2}_{12} = \Gamma^{2}_{21} = \frac{1}{r}, \tag{4.47}$$

and all other Christoffel symbols are zero. Since τ^{ik} is a function of r, only the differentiation of τ^{ik} with respect to r exists. This reduces the equilibrium equations to

$$\begin{aligned} \tau^{11}_{,1} + \frac{1}{r}\tau^{11} - r\tau^{22} &= 0, & (4.48)\\ \tau^{33}_{,2} &= 0, & (4.49)\\ \tau^{33}_{,3} &= 0. & (4.50) \end{aligned}$$

Substituting the components of τ into the equilibrium equations results in

$$\begin{aligned} \frac{\partial\tau^{rr}}{\partial r} &= r\left(\frac{1}{\rho(r)^2}\Phi + \left(\frac{1}{\rho(r)^2\rho'(r)^2} + \frac{\lambda_1^2}{\rho(r)^2}\right)\Psi + \frac{p}{r^2}\right) & (4.51)\\ &\quad -\frac{1}{r}\left(\frac{1}{\rho' r^2}\Phi + \left(\frac{r^2}{\rho(r)^2\rho'(r)^2} + \frac{\lambda_1^2}{\rho'(r)^2}\right)\Psi + p\right),\\ \tau^{zz}_{,\theta} &= \frac{\partial p}{\partial\theta} = 0, & (4.52)\\ \tau^{zz}_{,z} &= \frac{\partial p}{\partial z} = 0. & (4.53) \end{aligned}$$

Equation 4.52 and 4.53 inform us that $p = p(r)$ since Φ and Ψ are also functions of r. We

integrate Equation 4.52 from the inner radius to the arbitrary radial position r to obtain

$$\tau^{rr}|_{r=r} - \tau^{rr}|_{r=a_1} = \int_{a_1}^{r} \left(r\tau_{\theta\theta} - \frac{1}{r}\tau^{rr} \right) dr. \tag{4.54}$$

External forces exerting on the inner and outer surfaces of the tube can be written as

$$P^k = P^1\mathbf{G_1} + P^2\mathbf{G_2} + P^3\mathbf{G_3} = \tau^{ik}n_i, \tag{4.55}$$

where n_i are the components of unit normal vector to the surface. The unit normal vector is written in the form of

$$\mathbf{n} = n_1\mathbf{G^1} + n_2\mathbf{G^2} + n_3\mathbf{G^3}. \tag{4.56}$$

At $r = a_2$, the normal vector is

$$\mathbf{n} = \frac{\mathbf{G^1}}{\sqrt{G^{11}}}, \tag{4.57}$$

so that we have

$$n_1 = \frac{1}{\sqrt{G^{11}}} = 1, \quad n_2 = n_3 = 0 \quad \text{at} \quad r = a_2. \tag{4.58}$$

Substituting Equation 4.58 into Equation 4.55 yields

$$\tau^{rr}|_{r=a_2} = P^1. \tag{4.59}$$

Similarly, at $r = a_1$,

$$\mathbf{n} = -\frac{\mathbf{G^1}}{\sqrt{G^{11}}}. \tag{4.60}$$

Therefore, we obtain

$$n_1 = \frac{-1}{\sqrt{G^{11}}} = -1, \quad n_2 = n_3 = 0 \quad \text{at} \quad r = a_1. \tag{4.61}$$

Substituting Equation 4.61 into Equation 4.55 gives

$$\tau^{rr}|_{r=a_1} = -P^1. \tag{4.62}$$

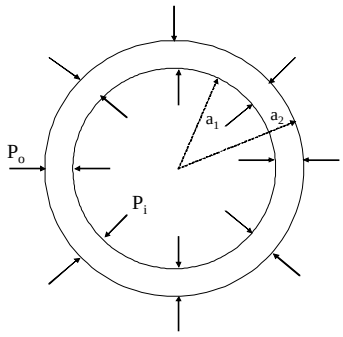

Figure 4.5. External forces acting on the inner and outer surfaces of a cylindrical tube.

From the boundary conditions shown in Figure 4.5, we have

$$P^1|_{r=a_1} = P_i, \quad P^1|_{r=a_2} = -P_o. \tag{4.63}$$

Therefore, we obtain

$$\tau^{rr}|_{r=a_1} = -P_i, \quad \tau^{rr}|_{r=a_2} = -P_o. \tag{4.64}$$

Applying Equation 4.64 to Equation 4.54 and defining $\triangle P \equiv P_i - P_o$ yields

$$\triangle P = \int_{a_1}^{a_2} \left(\left(\frac{r}{\rho(r)^2} - \frac{\rho(r)^2}{\lambda_1^2 r^3} \right) \Phi + \left(\frac{\lambda_1^2 r}{\rho(r)^2} - \frac{\rho(r)^2}{r^3} \right) \Psi \right) dr. \tag{4.65}$$

For the elastin stage, a neo–Hookian model is employed. Referring to Equation 4.18, we obtain

$$\Phi = 2\frac{\partial W}{\partial I_1} = 2C_1, \quad \Psi = 2\frac{\partial W}{\partial I_2} = 0. \tag{4.66}$$

This further reduces Equation 4.65 to

$$\triangle P = 2C_1 \int_{a_1}^{a_2} \left(\frac{r}{\rho(r)^2} - \frac{\rho(r)^2}{\lambda_1^2 r^3} \right) dr. \tag{4.67}$$

Integration of Equation 4.67 results in

$$\triangle P = \frac{C_1}{\lambda_1} \ln \left| \frac{\lambda_1(a_2^2 - a_1^2) + A_1^2}{A_1^2} \right| - \frac{2C_1}{\lambda_1} \ln \left| \frac{a_2}{a_1} \right| + \frac{C_1}{\lambda_1^2}(A_1^2 - \lambda_1 a_1^2) \left(\frac{1}{a_2^2} - \frac{1}{a_1^2} \right). \tag{4.68}$$

Now we use the incompressibility condition to find the relationship between a_1 and a_2 such that

$$A_2 = \rho(a_2) = \sqrt{\lambda_1 a_2^2 + A_1^2 - \lambda_1 a_1^2}. \tag{4.69}$$

Therefore,

$$a_2 = \sqrt{\frac{A_2^2 - A_1^2 + \lambda_1 a_1^2}{\lambda_1}}. \tag{4.70}$$

Equation 4.68 can be rewritten using an inflation ratio, λ_2 in the form of

$$\triangle P = \frac{C_1}{\lambda_1} \ln \left| \frac{\lambda_1 a_2^2 + A_1^2(1 - \lambda_1\lambda_2^2)}{A_1^2} \right| - \frac{2C_1}{\lambda_1} \ln \left| \frac{a_2}{\lambda_2 A_1} \right| + \frac{C_1 A_1^2}{\lambda_1^2}(1 - \lambda_1\lambda_2^2) \left(\frac{1}{a_2^2} - \frac{1}{\lambda_2^2 A_1^2} \right), \tag{4.71}$$

with

$$a_2 = \sqrt{\frac{A_2^2 - A_1^2(1 - \lambda_1\lambda_2^2)}{\lambda_1}}. \tag{4.72}$$

4.3.3.2 Stage II ($\lambda_a \leq \lambda < \lambda_b$).

We consider the motion from the configuration κ_2 to κ. Collagen fibres play a role independently on the arterial wall motion so that the stretching ratio, λ_1 is not taken account for the collagen recruitment. Starting with an unknown radius, $\rho_a(r)$ of the body B_1, the motion from B_1 to B can be described as

$$\hat{y}_1 = \rho_a(r)cos\theta, \quad \hat{y}_2 = \rho_a(r)sin\theta, \quad \hat{y}_3 = z \quad \text{for } B_1, \tag{4.73}$$

$$x_1 = rcos\theta, \quad x_2 = rsin\theta, \quad x_3 = z \quad \text{for } B. \tag{4.74}$$

Using the cylindrical coordinates. Metric tensors for the body B_1 become

$$[\hat{g}_{ik}] = DIAG\left[\rho_a'(r)^2,\ \rho_a(r)^2,\ 1\right], \tag{4.75}$$

$$[\hat{g}^{ik}] = DIAG\left[\frac{1}{\rho_a'(r)^2},\ \frac{1}{\rho_a(r)^2},\ 1\right]. \tag{4.76}$$

Metric tensors for the body B are shown in Equations 4.26 and 4.27. Since the incompressibility condition still holds, we obtain

$$\hat{I}_3 = \frac{G}{\hat{g}} = 1, \tag{4.77}$$

where G and $\hat{g}$ are

$$G = |G_{ik}| = r^2, \tag{4.78}$$

$$\hat{g} = |\hat{g}_{ik}| = \rho_a'(r)^2\rho_a(r)^2. \tag{4.79}$$

Therefore,

$$\rho_a'(r)^2\rho_a(r)^2 = r^2. \tag{4.80}$$

Then we can find the radius of body B_1 such that

$$\rho_a(r) = \sqrt{r^2 + C}. \tag{4.81}$$

Applying the initial conditions which are

$$\hat{A}_1 = \rho_a(a_1), \quad \hat{A}_2 = \rho_a(a_2), \tag{4.82}$$

to Equation 4.81 yields

$$\rho_a(r) = \sqrt{r^2 + \hat{A}_1^2 - a_1^2}. \tag{4.83}$$

Three invariants can be found using the metric tensors as follows ;

$$\hat{I}_1 = \hat{g}^{rs}G_{rs} = \frac{1}{\rho'_a(r)^2} + \frac{r^2}{\rho_a(r)^2} + 1, \tag{4.84}$$

$$\hat{I}_2 = G^{rs}\hat{g}_{rs}\hat{I}_3 = \rho'_a(r)^2 + \frac{\rho_a(r)^2}{r^2} + 1, \tag{4.85}$$

$$\hat{I}_3 = 1. \tag{4.86}$$

Using the first invariant, we obtain $\hat{B}^{ij}$ defined as

$$\hat{B}^{ij} = \hat{I}_1\hat{g}^{ij} - \hat{g}^{ir}\hat{g}^{js}G_{rs}, \tag{4.87}$$

as follows ;

$$[\hat{B}^{ij}] = DIAG\left[\frac{r^2}{\rho_a(r)^2\rho'_a(r)^2} + \frac{1}{\rho'_a(r)^2},\ \frac{1}{\rho_a(r)^2\rho'_a(r)^2} + \frac{1}{\rho_a(r)^2},\ \frac{1}{\rho'_a(r)^2} + \frac{r^2}{\rho_a(r)^2}\right]. \tag{4.88}$$

The strain energy for this stage is a linear combination of W and $\hat{W}$ which are given in Equations 4.18 and 4.19 so that

$$W = W(I_1, I_2) + \hat{W}(\hat{I}_1, \hat{I}_2) = C_1(I_1 - 3) + \frac{\alpha}{2\gamma}e^{\gamma(\hat{I}_1 - 3)}. \tag{4.89}$$

We then obtain

$$\hat{\Phi} = 2\frac{\partial W}{\partial \hat{I}_1} = \alpha e^{\gamma(\hat{I}_1 - 3)}, \tag{4.90}$$

$$\hat{\Psi} = 2\frac{\partial W}{\partial \hat{I}_2} = 0. \tag{4.91}$$

This reduces the proposed constitutive relation, Equation 4.11 to

$$\tau^{ij} = pG^{ij} + 2C_1 g^{ij} + \hat{\Phi}\hat{g}^{ij}. \tag{4.92}$$

Stress tensor τ can be obtained using the metric tensors as follows ;

$$[\tau^{ij}] = DIAG\,[p + \frac{2C_1}{\rho'(r)^2} + \frac{\hat{\Phi}}{\rho'_a(r)^2}, \frac{p}{r^2} + \frac{2C_1}{\rho(r)^2} + \frac{\hat{\Phi}}{\rho_a(r)^2}, p + 2C_1\lambda_1^2 + \hat{\Phi}]. \tag{4.93}$$

With a negligible gravity force, equilibrium equations in this stage form

$$\tau^{ik}||_i = 0. \tag{4.94}$$

Rewriting 4.94 in terms of the second Christoffel symbols yields

$$\tau^{ik}_{,i} + \Gamma^i_{ir}\tau^{rk} + \Gamma^k_{ir}\tau^{ir} = 0. \tag{4.95}$$

Then the equilibrium equations can become

$$\begin{aligned} \tau^{rr}|_{r=a_2} - \tau^{rr}|_{r=a_1} &= \int_{a_1}^{a_2} (r\tau^{\theta\theta} - \frac{1}{r}\tau^{rr})\ dr \\ &= \int_{a_1}^{a_2} (\frac{2C_1}{\rho(r)^2}r - \frac{2C_1}{\rho'(r)^2}\frac{1}{r} \\ &\quad + \frac{\hat{\Phi}}{\rho_a(r)^2}r - \frac{\hat{\Phi}}{\rho'_a(r)^2}\frac{1}{r})\ dr \end{aligned} \tag{4.96}$$

Applying the boundary conditions shown in Figure 4.5 such that

$$\tau^{rr}|_{r=a_1} = -P_i, \quad \tau^{rr}|_{r=a_2} = -P_o, \tag{4.97}$$

results in

$$\triangle P = \int_{a_1}^{a_2} \left(\frac{2C_1}{\rho(r)^2}r - \frac{2C_1}{\rho'(r)^2}\frac{1}{r} + \frac{\hat{\Phi}}{\rho_a(r)^2}r - \frac{\hat{\Phi}}{\rho'_a(r)^2}\frac{1}{r} \right)\ dr, \tag{4.98}$$

where

$$\rho(r) = \sqrt{\lambda_1 r^2 + A_1^2 - \lambda_1 a_1^2}, \tag{4.99}$$

$$\rho'(r) = \lambda_1 r(\lambda_1 r^2 + A_1^2 - \lambda_1 a_1^2)^{-1/2}, \tag{4.100}$$

$$\rho_a(r) = \sqrt{r^2 + \hat{A}_1^2 - a_1^2}, \tag{4.101}$$

$$\rho_a'(r) = r(r^2 + \hat{A}_1^2 - a_1^2)^{-1/2}. \tag{4.102}$$

Integrating Equation 4.98 yields

$$\begin{aligned} \triangle P = & \frac{C_1}{\lambda_1} \ln \left| \frac{\lambda_1(a_2^2 - a_1^2) + A_1^2}{A_1^2} \right| - \frac{2C_1}{\lambda_1} \ln \left| \frac{a_2}{a_1} \right| \\ & + \frac{C_1}{\lambda_1^2}(A_1^2 - \lambda_1 a_1^2) \left(\frac{1}{a_2^2} - \frac{1}{a_1^2} \right) \\ & + \alpha \int_{a_1}^{a_2} \left(\frac{r e^{\gamma(\hat{I}_1 - 3)}}{r^2 + \hat{A}_1^2 - a_1^2} \right) \, dr. \\ & - \alpha \int_{a_1}^{a_2} \left(\frac{(r^2 + \hat{A}_1^2 - a_1^2) e^{\gamma(\hat{I}_1 - 3)}}{r^3} \right) \, dr \end{aligned} \tag{4.103}$$

Now the incompressibility condition can be applied to find the relationship between a_1 and a_2 as follows :

$$\hat{A}_2 = \rho_a(a_2) = \sqrt{a_2^2 + \hat{A}_1^2 - a_1^2}, \tag{4.104}$$

so that

$$a_2 = \sqrt{\hat{A}_2^2 - \hat{A}_1^2 + a_1^2} = \sqrt{\frac{A_2^2 - A_1^2 + \lambda_1 a_1^2}{\lambda_1}}. \tag{4.105}$$

Since λ_{2a} is $\hat{A}_1/A_1$, using the inflation ratio, λ_2, we rewrite Equation 4.98 in terms of λ_1, λ_2

and λ_{2a} such that

$$\begin{aligned}\triangle P &= \frac{C_1}{\lambda_1}\ln\left|\frac{\lambda_1 a_2^2 + A_1^2(1-\lambda_1\lambda_2^2)}{A_1^2}\right| - \frac{2C_1}{\lambda_1}\ln\left|\frac{a_2}{\lambda_2 A_1}\right| \\ &+\frac{C_1 A_1^2}{\lambda_1^2}(1-\lambda_1\lambda_2^2)\left(\frac{1}{a_2^2}-\frac{1}{\lambda_2^2 A_1^2}\right) \\ &+\alpha\int_{a_1}^{a_2}\left(\frac{re^{\gamma(\hat{I}_1-3)}}{r^2+(\lambda_{2a}^2-\lambda_2^2)A_1^2}\right)\,dr \\ &-\alpha\int_{a_1}^{a_2}\left(\frac{(r^2+(\lambda_{2a}^2-\lambda_2^2)A_1^2)e^{\gamma(\hat{I}_1-3)}}{r^3}\right)\,dr,\end{aligned} \tag{4.106}$$

where

$$a_2 = \sqrt{\frac{A_2^2 - A_1^2(1-\lambda_1\lambda_2^2)}{\lambda_1}}, \tag{4.107}$$

$$\hat{I}_1 = \frac{r^2+(\lambda_{2a}^2-\lambda_2^2)A_1^2}{r^2} + \frac{r^2}{r^2+(\lambda_{2a}^2-\lambda_2^2)A_1^2} + 1. \tag{4.108}$$

The material constants, C_1, α and γ are obtained by fitting the pressure-radius curve in Figure 4.1 using the nonlinear equation given in Equation 4.106. These material constants are then used to evaluate oscillatory motions of arterial wall using the small on large theory discussed in next section.

4.4 Mathematical Analysis of Periodic Motions of Vessel Wall

As a result of the pulsatile nature of blood flow, the arterial wall oscillates.[134,136] However, due to the complexity of the problem, analytical studies of nonlinear deformations of the arterial wall are confined to static uniform loading.[114,116,120,125,144] Studies that account for the fluctuation of the vessel wall, have not accounted for the large deformation associated with prestretch and uniform loading under average physiological pressure. Rather these studies only considered the small periodic motions of vessel wall, about an assumed stress free configuration. The pressure oscillation corresponds to approximately 20 to 25 % change of the systemic pressure[114,126] and the corresponding radial strain is smaller than 0.1.[136]

This suggests that the motion of *in vivo* arterial wall can be modeled using the small on large theory proposed by A.E. Green *et al.*.[115] In this work, the axial extension and inflation corresponding to loading up to the systemic pressure are modeled as large deformations and the oscillatory motions superposed on these are small.

The small on large theory approximates the exact theory for a complete nonlinear behavior using a superposition method. We superpose small deformations on a known finite deformation of a homogeneous elastic body. The theory approximates the covariant base vectors to obtain the vectors of a current configuration by deforming a body by a small amount. Based on these approximated base vectors, the strain invariants, the strain energy, the stress components and therefore, the linear momentum equations for the current body can be obtained. The detailed procedure to obtain the equations are given in the Appendix B. To apply these equations to the dual mechanism material, we consider two stages for the collagen recruitment described earlier. All of the equations in the Appendix B can be applicable to the two stages. Accordingly, for the first stage based on the small on large theory, the classical solutions of the elastin stage are used to obtain the approximate solutions whereas the classical solutions from the elastin/collagen stage are used for the second stage based on the small on large theory. Since different strain energy functions are applied to each stage based on the small on large theory, each stage will have a different form of constitutive relations, λ^{ij} and therefore, the linear momentum equations. To describe the behavior of periodic motions of vessel wall we find solutions of small deformation with time by prescribing an oscillatory pressure force.

4.4.1 Small Deformation Superposed on Finite Uniform Extension and Inflation of a Cylindrical Tube under a Static Loading Condition

We further deform the strained body B which is deformed by finite uniform extension and inflation by an infinitesimal displacement, $\epsilon\mathbf{w}$ (see B.1), defining the displacement vector, $\mathbf{w}$

as

$$\mathbf{w} = w_m \mathbf{G}^m = w^m \mathbf{G}_m, \quad w_1 = u,\ w_2 = v,\ w_3 = w. \tag{4.109}$$

Consider the deformation $u = u(r)$, and $v = w = 0$. Then ϵ is defined as

$$\epsilon = \frac{(\bar{a}_1 - a_1)}{u(a_1)}, \tag{4.110}$$

where $\bar{a}_1$ is the current inner radius of the body $\bar{B}$ (see Appendix B). Referring to Equation B.8, we obtain the components of the covariant metric tensor,

$$G'_{ij} = w_{i,j} + w_{j,i} - 2\Gamma^1_{ij} u, \tag{4.111}$$

so that

$$[G'_{ij}] = DIAG\left[2\frac{\partial u(r)}{\partial r}, 2u(r)r, 0\right]. \tag{4.112}$$

The components of the contravariant metric tensor from Equation B.8 become

$$\begin{aligned} G'^{ij} \quad = \quad & -(G^{i1}G^{j1}G'_{11} + G^{i1}G^{j2}G'_{12} + G^{i1}G^{j3}G'_{13} \\ & G^{i2}G^{j1}G'_{21} + G^{i2}G^{j2}G'_{22} + G^{i2}G^{j3}G'_{23} \\ & G^{i3}G^{j1}G'_{31} + G^{i3}G^{j2}G'_{32} + G^{i3}G^{j3}G'_{33}), \end{aligned} \tag{4.113}$$

so that

$$[G'^{ij}] = DIAG\left[-2\frac{\partial u(r)}{\partial r}, -\frac{2u(r)}{r^3}, 0\right]. \tag{4.114}$$

We use these results and the components of contravariant base vectors, g^{ij} in Stage I and $\hat{g}^{ij}$ in Stage II (see Equations 4.25 and 4.77) to obtain three invariants for each stage (see

Equation B.10) as follows. For Stage I,

$$\begin{aligned} I_1' = g^{rs}G_{rs}' &= g^{1s}G_{1s}' + g^{2s}G_{2s}' + g^{3s}G_{3s}' \\ &= g^{11}G_{11}' + g^{22}G_{22}' + g^{33}G_{33}' \\ &= \frac{1}{(\rho')^2}G_{11}' + \frac{1}{\rho^2}G_{22}' + \lambda^2 G_{33}' \\ &= \frac{2}{(\rho')^2}\frac{\partial u}{\partial r} + \frac{2u(r)r}{\rho^2}, \end{aligned} \tag{4.115}$$

$$\begin{aligned} I_2' &= g_{11}(G''^{11} + G^{11}I_3') + g_{22}(G''^{22} + G^{22}I_3') + g_{33}(G''^{33} + G^{33}I_3') \\ &= -2\rho'^2\frac{\partial u}{\partial r} - \rho^2\frac{2u(r)}{r^3}. \end{aligned} \tag{4.116}$$

For Stage II,

$$\begin{aligned} \hat{I}_1' = \hat{g}^{rs}G_{rs}' &= \frac{1}{(\rho_a')^2}G_{11}' + \frac{1}{\rho_a^2}G_{22}' + G_{33}' \\ &= \frac{2}{(\rho_a')^2}\frac{\partial u}{\partial r} + \frac{2u(r)r}{\rho_a^2}, \end{aligned} \tag{4.117}$$

$$\begin{aligned} \hat{I}_2' &= \hat{g}_{11}(G''^{11} + G^{11}I_3') + \hat{g}_{22}(G''^{22} + G^{22}I_3') + \hat{g}_{33}(G''^{33} + G^{33}I_3') \\ &= -2\rho_a'^2\frac{\partial u}{\partial r} - \rho_a^2\frac{2u(r)}{r^3}. \end{aligned} \tag{4.118}$$

For all the stages,

$$\begin{aligned} I_3' = \hat{I}_3' &= I_3 G^{ij}G_{ij}' \\ &= G^{11}G_{11}' + G^{22}G_{22}' + G^{33}G_{33}' \\ &= 2\frac{\partial u}{\partial r} + \frac{2u(r)}{r} \\ &= 0, \end{aligned} \tag{4.119}$$

It then follows that

$$\frac{\partial u}{\partial r} = -\frac{u(r)}{r}, \tag{4.120}$$

so that

$$u(r) = \frac{k}{r}. \tag{4.121}$$

The components of stress tensor in Stage I are expressed in Equation B.21. For Stage II, the proposed constitutive equation given in Equation 4.11 becomes

$$\begin{aligned} \bar{\tau}^{ij} = \tau^{ij} + \epsilon\tau'^{ij} &= (p+\epsilon p')(G^{ij}+\epsilon G'^{ij}) + (\Phi+\epsilon\Phi')g^{ij} + (\Psi+\epsilon\Psi')(B^{ij}+\epsilon B'^{ij}) \\ &\quad +(\hat{\Phi}+\epsilon\hat{\Phi}')\hat{g}^{ij} + (\hat{\Psi}+\epsilon\hat{\Psi}')(\hat{B}^{ij}+\epsilon\hat{B}'^{ij}), \end{aligned} \tag{4.122}$$

for the current body. Neglecting the terms of $O(\epsilon^2)$ and collecting the terms of $O(\epsilon)$, we find that in Stage II,

$$\tau'^{ij} = p'G^{ij} + pG'^{ij} + \Phi' g^{ij} + \Psi B'^{ij} + \Psi' B^{ij} + \hat{\Phi}'\hat{g}^{ij} + \hat{\Psi}\hat{B}' ij + \hat{\Psi}'\hat{B}^{ij}. \tag{4.123}$$

Generally for all the stages under a static loading condition, neglecting body force and acceleration, the equation of motion (B.24) becomes

$$\lambda^{ij}||_i = 0, \tag{4.124}$$

where

$$\lambda^{ij} = \tau'^{ij} + \tau^{im}w^j_{,m} + \tau^{im}\Gamma^j_{sm}w^s + \tau^{ij}w^m_{,m} + \tau^{ij}\Gamma^m_{km}w^k, \tag{4.125}$$

so that

$$[\lambda^{ij}] = DIAG\left[\tau'^{11} + 2\tau^{11}\frac{\partial u}{\partial r} + \tau^{11}\frac{u}{r}, \tau'^{22} + 2\tau^{22}\frac{u}{r} + \tau^{22}\frac{\partial u}{\partial r}, \tau'^{33} + \tau^{33}\frac{\partial u}{\partial r} + \tau^{33}\frac{u}{r}\right]. \tag{4.126}$$

Since differentiation of λ^{ij} with respect to i in the body B is defined as

$$\lambda^{ij}||_i = \lambda^{ij}_{,i} + \lambda^{ij}\Gamma^s_{si} + \lambda^{is}\Gamma^j_{si}, \tag{4.127}$$

where

$$\Gamma^m_{2m} = \Gamma^m_{3m} = 0, \quad \Gamma^m_{1m} = \frac{1}{r}, \tag{4.128}$$

finally, the equilibrium equations for all the stages can be written in the form of

$$\begin{aligned} \frac{\partial \lambda^{11}}{\partial r} + \frac{\lambda^{11}}{r} - \lambda^{22} r &= 0 \quad \text{when} \quad j = 1, && (4.129)\\ \frac{\partial \lambda^{22}}{\partial \theta} &= 0 \quad \text{when} \quad j = 2, && (4.130)\\ \frac{\partial \lambda^{33}}{\partial z} &= 0 \quad \text{when} \quad j = 3. && (4.131) \end{aligned}$$

We now look for solutions of two separate stages using dual mechanisms in the small on large theory.

4.4.1.1 Stage I ($\lambda < \lambda_a$).

In this stage, the scalar invariants Φ' and Ψ' are found to be

$$\begin{aligned} \Phi' &= AI_1' + FI_2' = 0,\\ \Psi' &= FI_1' + BI_2' = 0, \end{aligned} \tag{4.132}$$

because the constants, A, B, F in Equations B.18 and B.19 become

$$A = \frac{\partial \Phi}{\partial I_1} = 0, \quad B = \frac{\partial \Psi}{\partial I_2} = 0, \quad F = \frac{\partial \Psi}{\partial I_1} = 0, \tag{4.133}$$

where

$$\Phi = 2C_1, \quad \Psi = 0, \quad I_3 = 1, \quad I_3' = 0. \tag{4.134}$$

Then from the components of stress tensor τ' (see Equation B.21), we can find that

$$[\tau'^{ij}] = DIAG\left[\frac{2pk}{r^2} + p', -\frac{2pk}{r^4} + \frac{p'}{r^2}, p'\right]. \tag{4.135}$$

Using the result of the incompressibility condition, Equation 4.121, the components of tensor, λ (see Equation 4.126) can be found as

$$[\lambda^{ij}] = DIAG\left[p' + \frac{2pk}{r^2} - \tau^{11}\frac{k}{r^2}, -\frac{2pk}{r^4} + \frac{p'}{r^2} + \tau^{22}\frac{k}{r^2}, p'\right], \tag{4.136}$$

where

$$\begin{cases} \tau^{11} &= \dfrac{2C_1}{\rho'^2} + p, \\ \\ \tau^{22} &= \dfrac{2C_1}{\rho^2} + \dfrac{p}{r^2}. \end{cases} \tag{4.137}$$

recalling that p and τ are a function of r and applying Equation 4.136 to the equilibrium equations, Equations 4.129 to 4.131 yields

$$\frac{\partial \lambda^{11}}{\partial r} = \frac{2kC_1}{r\rho^2} + \frac{2kC_1}{r^3\rho'^2} - \frac{2kp}{r^3}, \tag{4.138}$$

$$\frac{\partial p'}{\partial \theta} = 0, \tag{4.139}$$

$$\frac{\partial p'}{\partial z} = 0, \tag{4.140}$$

so that $p' = f(r)$. We now apply boundary conditions. The current external force measured per unit area of the surface of the body B is expressed as

$$\mathbf{P} + \epsilon\mathbf{P'} = (P^j + \epsilon P'^j)\mathbf{G}_j = (n_i\tau^{ij} + \epsilon n_i\lambda^{ij})\mathbf{G}_j, \tag{4.141}$$

so that we can find the current inner and outer pressures of the body $\bar{B}$ such that

$$\begin{aligned}(\mathbf{P}+\epsilon\mathbf{P}')|_{r=a_1} &= (-\tau^{1j}-\epsilon\lambda^{1j})\mathbf{G}_j)|_{r=a_1},\\ (\mathbf{P}+\epsilon\mathbf{P}')|_{r=a_2} &= (\tau^{1j}+\epsilon\lambda^{1j})\mathbf{G}_j)|_{r=a_2},\end{aligned} \tag{4.142}$$

since the normal vectors for the inner and outer surfaces of body $\bar{B}$ are

$$\begin{aligned}n_1 &= -1, \quad n_2=n_3=0 \quad \text{at} \quad r=a_1,\\ n_1 &= 1, \quad\quad n_2=n_3=0 \quad \text{at} \quad r=a_2,\end{aligned} \tag{4.143}$$

respectively. Defining the current inner and outer pressures as $\bar{P}_i$ and $\bar{P}_o$, respectively, applying the boundary conditions yields that

$$(\mathbf{P}+\epsilon\mathbf{P}')|_{r=a_1} = -\bar{P}_o\mathbf{G}_1, \tag{4.144}$$

$$(\mathbf{P}+\epsilon\mathbf{P}')|_{r=a_2} = \bar{P}_i\mathbf{G}_1, \tag{4.145}$$

so that the pressure difference defined as $\triangle\bar{P}\equiv\bar{P}_i-\bar{P}_o$ can be found as

$$\triangle\bar{P}\mathbf{G}_1 = (\mathbf{P}+\epsilon\mathbf{P}')|_{r=a_1}+(\mathbf{P}+\epsilon\mathbf{P}')|_{r=a_2}, \tag{4.146}$$

$$\triangle\bar{P} = (\tau^{11}|_{r=a_2}-\tau^{11}|_{r=a_1})+\epsilon(\lambda^{11}|_{r=a_2}-\lambda^{11}|_{r=a_1}), \tag{4.147}$$

$$\triangle\bar{P} = \triangle P+\epsilon(\lambda^{11}|_{r=a_2}-\lambda^{11}|_{r=a_1}), \tag{4.148}$$

where

$$\lambda^{11}|_{r=a_2}-\lambda^{11}|_{r=a_1} = 2kC_1\int_{a_1}^{a_2}\left(\frac{1}{r\rho^2}+\frac{1}{r^3\rho'^2}\right)dr-2k\int_{a_1}^{a_2}\frac{p(r)}{r^3}dr. \tag{4.149}$$

The above equation is obtained by integrating Equation 4.138 with respect to r.

4.4.1.2 Stage II ($\lambda_a \leq \lambda < \lambda_b$).

In this stage, $\rho_a(r)$ is used and the scalar invariants $\hat{\Phi}'$ and $\hat{\Psi}'$ become

$$\begin{aligned} \hat{\Phi}' &= A\hat{I}_1' + F\hat{I}_2' = \alpha\gamma e^{\gamma(\hat{I}_1-3)}\hat{I}_1', \\ \hat{\Psi}' &= F\hat{I}_1' + B\hat{I}_2' = 0, \end{aligned} \tag{4.150}$$

because the constants A, B, F in Equations B.18 and B.19 in this stage are found to be

$$A = \frac{\partial\hat{\Phi}}{\partial\hat{I}_1} = \alpha\gamma e^{\gamma(\hat{I}_1-3)}, \quad B = \frac{\partial\hat{\Psi}}{\partial\hat{I}_2} = 0, \quad F = \frac{\partial\hat{\Psi}}{\partial\hat{I}_1} = 0, \tag{4.151}$$

where

$$\hat{\Phi} = \alpha e^{\gamma(\hat{I}_1-3)}, \quad \hat{\Psi} = 0, \quad \hat{I}_3 = 1, \quad \hat{I}_3' = 0. \tag{4.152}$$

The components of the stress tensor τ' (see Equation 4.123) then become

$$\begin{aligned} [\tau'^{ij}] = \quad & DIAG[\frac{\alpha\gamma e^{\gamma(\hat{I}_1-3)}}{\rho_a'^2}\hat{I}_1' - 2p\frac{\partial u}{\partial r} + p', \frac{\alpha\gamma e^{\gamma(\hat{I}_1-3)}}{\rho_a^2}\hat{I}_1' - \frac{2pu}{r^3} + \frac{p'}{r^2}, \\ & \lambda^2\alpha\gamma e^{\gamma(\hat{I}_1-3)}\hat{I}_1' + p']. \end{aligned} \tag{4.153}$$

Using the result of the incompressibility condition, Equation 4.121, The three invariants are found to be

$$\hat{I}_1' = -\frac{2k}{\rho_a'^2 r^2} + \frac{2k}{\rho_a^2} \tag{4.154}$$

$$\hat{I}_2' = 2\rho_a'^2\frac{k}{r^2} - 2\rho_a^2\frac{k}{r^4} \tag{4.155}$$

$$\hat{I}_3' = 0 \tag{4.156}$$

The components of the tensor, λ (see Equation 4.126) with $u(r) = k/r$ can then be found as

$$\begin{cases} \lambda^{11} &= \dfrac{\alpha\gamma e^{\gamma(\hat{I}_1-3)}}{\rho_a'^2}\hat{I}_1' + p' + \dfrac{2kp}{r^2} - \tau^{11}\dfrac{k}{r^2}, \\ \lambda^{22} &= \dfrac{\alpha\gamma e^{\gamma(\hat{I}_1-3)}}{\rho_a^2}\hat{I}_1' - \dfrac{2pk}{r^4} + \dfrac{p'}{r^2} + \tau^{22}\dfrac{k}{r^2}, \\ \lambda^{33} &= \lambda^2\alpha\gamma e^{\gamma(\hat{I}_1-3)}\hat{I}_1' + p', \\ \lambda^{12} &= \lambda^{13} = \lambda^{21} = \lambda^{23} = \lambda^{31} = \lambda^{32} = 0, \end{cases} \tag{4.157}$$

where

$$\begin{cases} \tau^{11} &= \dfrac{2C_1}{\rho'^2} + p + \dfrac{\alpha e^{\gamma(\hat{I}_1-3)}}{\rho_a'^2}, \\ \tau^{22} &= \dfrac{2C_1}{\rho^2} + \dfrac{p}{r^2} + \dfrac{\alpha e^{\gamma(\hat{I}_1-3)}}{\rho_a^2}. \end{cases} \tag{4.158}$$

recalling that p and τ and $\hat{I}_1$ are a function of r and substituting Equation 4.157 into the equilibrium equations, Equation 4.129 to 4.131 yields

$$\frac{\partial\lambda^{11}}{\partial r} = \frac{-1}{r\rho_a'^2}\alpha\gamma e^{\gamma(\hat{I}_1-3)}\hat{I}_1' + \frac{r}{\rho_a^2}\alpha\gamma e^{\gamma(\hat{I}_1-3)}\hat{I}_1' - \frac{4kp}{r^3} + \tau^{11}\frac{k}{r^3} + \tau^{22}\frac{k}{r}, \tag{4.159}$$

$$\frac{\partial p'}{\partial\theta} = \frac{\partial p'}{\partial z} = 0, \tag{4.160}$$

so that $p' = f(r)$. Applying the boundary conditions in Equation 4.144 and 4.145, the pressure difference, $\triangle\bar{P}$ can be written in

$$\triangle\bar{P} = \triangle P + \epsilon(\lambda^{11}|_{r=a_2} - \lambda^{11}|_{r=a_1}), \tag{4.161}$$

where, by integrating Equation 4.159 with respect to r,

$$\lambda^{11}|_{r=a_2} - \lambda^{11}|_{r=a_1} = \int_{a_1}^{a_2} \left(\frac{-\alpha\gamma e^{\gamma(\hat{I}_1-3)}\hat{I}_1'}{r\rho_a'^2} + \frac{r}{\rho_a^2}\alpha\gamma e^{\gamma(\hat{I}_1-3)}\hat{I}_1' - \frac{4kp(r)}{r^3} + \tau^{11}\frac{k}{r^3} + \tau^{22}\frac{k}{r} \right) dr. \tag{4.162}$$

We rewrite Equation 4.162 using Equations 4.154 and 4.158 such that

$$\begin{aligned} \lambda^{11}|_{r=a_2} - \lambda^{11}|_{r=a_1} &= k\Big(\int_{a_1}^{a_2} \frac{-\alpha\gamma e^{\gamma(\hat{I}_1-3)}}{r\rho_a'^2}\left(\frac{2}{\rho_a^2} - \frac{2}{r^2\rho_a'^2}\right) + \frac{r}{\rho_a^2}\alpha\gamma e^{\gamma(\hat{I}_1-3)}\left(\frac{2}{\rho_a^2} - \frac{2}{r^2\rho_a'^2}\right) \\ &\quad + \frac{1}{r}\left(\frac{\alpha e^{\gamma(\hat{I}_1-3)}}{\rho_a^2} + \frac{2C_1}{\rho^2}\right) + \frac{1}{r^3}\left(\frac{\alpha e^{\gamma(\hat{I}_1-3)}}{\rho_a'^2} + \frac{2C_1}{\rho'^2}\right) dr \\ &\quad - \int_{a_1}^{a_2} \frac{1}{r^2}\frac{\partial p}{\partial r} dr + \left(\frac{p(a_2)}{a_2^2} - \frac{p(a_1)}{a_1^2}\right)\Big), \end{aligned} \tag{4.163}$$

integrating the term of $p(r)$ in Equation 4.162 by parts. Equation 4.163 includes the term of $\partial p(r)/\partial r$ which can be obtained from the analysis in Stage I of the large deformations and written in the form of

$$\begin{aligned} \frac{\partial p}{\partial r} &= 4C_1\left(\frac{A_1^2}{\lambda_1^2} - \frac{a_1^2}{\lambda_1}\right)\frac{1}{r^3} + C_1\left(\frac{A_1^2}{\lambda_1 r^2 + A_1^2 - \lambda_1 a_1^2}\right)\frac{2r}{A_1^2} \\ &\quad \frac{2C_1}{r\lambda_1} - \frac{2C_1}{r^3\lambda_1^2}(A_1^2 - \lambda_1 a_1^2). \end{aligned} \tag{4.164}$$

We again rewrite Equation 4.163 using $p(a_1)$ and $p(a_2)$ so that

$$\begin{aligned} \lambda^{11}|_{r=a_2} - \lambda^{11}|_{r=a_1} &= k\Big(\int_{a_1}^{a_2} \frac{-\alpha\gamma e^{\gamma(\hat{I}_1-3)}}{r\rho_a'^2}\left(\frac{2}{\rho_a^2} - \frac{2}{r^2\rho_a'^2}\right) + \frac{r}{\rho_a^2}\alpha\gamma e^{\gamma(\hat{I}_1-3)}\left(\frac{2}{\rho_a^2} - \frac{2}{r^2\rho_a'^2}\right) \\ &\quad + \frac{1}{r}\left(\frac{\alpha e^{\gamma(\hat{I}_1-3)}}{\rho_a^2} + \frac{2C_1}{\rho^2}\right) + \frac{1}{r^3}\left(\frac{\alpha e^{\gamma(\hat{I}_1-3)}}{\rho_a'^2} + \frac{2C_1}{\rho'^2}\right) dr \\ &\quad - \int_{a_1}^{a_2} \frac{1}{r^2}\frac{\partial p}{\partial r} dr + \left(\frac{2C_1\rho^2(a_1)}{\lambda_1^2 a_1^4} - \frac{2C_1\rho^2(a_2)}{\lambda_1^2 a_2^4}\right) \\ &\quad + \frac{\triangle P}{a_1^2} + \left(\frac{1}{a_1^2} - \frac{1}{a_2^2}\right) P_o\Big), \end{aligned} \tag{4.165}$$

Equation 4.165 includes the unphysical term of P_o which arises from the approximations by the small on large theory as expected in the linearized theory of elasticity. This term of P_o is taken to be zero in our analysis.

4.4.2 Periodic Motions of Vessel Wall

So far, we obtained the solutions of small radial deformation superposed on the large deformations under a static loading condition. The base pressure of artery reported in[114] is $100mmHg$ and the corresponding dimensionless pressure, $P/\bar{P}$ is 1. The vessel deforms by the large deformations up to $P/\bar{P} = 1$ under a static loading condition and then, experiences a pulsatile pressure force. The motions of vessel wall governed by the pulsatility are to be described by the small deformation. The body B deformed by the large deformations has the inner and outer radius, a_1 and a_2, respectively, at the base pressure. These radii and $\triangle P$ are constants and therefore, the current pressure-radius relation (see Equation 4.161) of the body $\bar{B}$ turns out to be linear. From Equation 4.110, the current inner radius of the body $\bar{B}$ is obtained by

$$\bar{a}_1 = a_1 + \epsilon u(a_1) = a_1 + \frac{\epsilon k}{a_1}, \tag{4.166}$$

and rewriting Equations 4.161 and 4.165 by taking k out of the integral yields

$$\begin{aligned}
\triangle\bar{P} = \triangle P \;+\; & \epsilon k\Bigg(\int_{a_1}^{a_2} \frac{-\alpha\gamma e^{\gamma(\hat{I}_1-3)}}{r\rho_a'^2}\left(\frac{2}{\rho_a^2} - \frac{2}{r^2\rho_a'^2}\right) + \frac{r}{\rho_a^2}\alpha\gamma e^{\gamma(\hat{I}_1-3)}\left(\frac{2}{\rho_a^2} - \frac{2}{r^2\rho_a'^2}\right) \\
& + \frac{1}{r}\left(\frac{\alpha e^{\gamma(\hat{I}_1-3)}}{\rho_a^2} + \frac{2C_1}{\rho^2}\right) + \frac{1}{r^3}\left(\frac{\alpha e^{\gamma(\hat{I}_1-3)}}{\rho_a'^2} + \frac{2C_1}{\rho'^2}\right) dr \\
& - \int_{a_1}^{a_2} \frac{1}{r^2}\frac{\partial p}{\partial r} dr + \left(\frac{2C_1\rho^2(a_1)}{\lambda_1^2 a_1^4} - \frac{2C_1\rho^2(a_2)}{\lambda_1^2 a_2^4}\right) \\
& + \frac{\triangle P}{a_1^2} + \left(\frac{1}{a_1^2} - \frac{1}{a_2^2}\right) P_o\Bigg) \\
\equiv \;& \triangle P + \epsilon k C_2,
\end{aligned} \tag{4.167}$$

From Equations 4.166 and 4.167, we know that ϵk determines the current pressure, $\triangle\bar{P}$ so that when ϵk is zero, $\triangle\bar{P} = \triangle P$ and $\bar{a}_1 = a_1$ as shown in Figure 4.6.

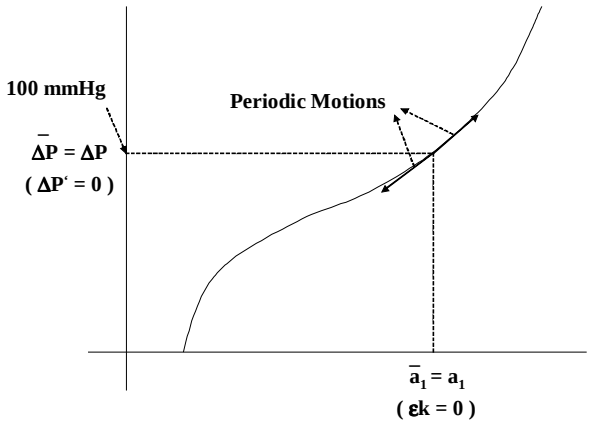

Figure 4.6. Relation between $\triangle \bar{P}$ and $\triangle P$.

Under a periodic pressure force, the equations of motion (see Equation B.23) of the body $\bar{B}$ become

$$\tau^{ij}||_i + \epsilon\lambda^{ij}||_i = \rho(f^j + \epsilon f'^j), \tag{4.168}$$

neglecting the body force where ρ is the density of artery. Since the large deformations are under a static loading condition, f^j is zero. Then collecting the terms of $O(\epsilon)$ of Equation 4.168 yields

$$\lambda^{ij}||_i = \rho f'^j = \rho\frac{d^2u(a_1)}{dt^2} = \frac{\rho}{a_1}\frac{d^2k}{dt^2}, \tag{4.169}$$

so that

$$\frac{\partial\lambda^{11}}{\partial r} + \frac{\lambda^{11}}{r} - \lambda^{22}r = \frac{\rho}{a_1}\frac{d^2k}{dt^2}. \tag{4.170}$$

As will be discussed in the result section, the vessel deformed by the large deformations up to the base pressure is in Stage II and therefore, the solutions of Stage II are used to describe the periodic motions. Integrating Equation 4.170 and applying the boundary conditions give

$$\triangle P' = kC_2 + \frac{\rho(a_2 - a_1)}{a_1}\frac{d^2k}{dt^2}. \tag{4.171}$$

If we consider a sinusoidal pressure force such that

$$\triangle \bar{P} = \triangle P + \epsilon \triangle p' = \triangle P + A_o \sin(\omega t), \tag{4.172}$$

then Equation 4.171 can be written as

$$\frac{\rho(a_2 - a_1)}{a_1} \frac{d^2(\epsilon k)}{dt^2} + C_2(\epsilon k) = A_o \sin(\omega t). \tag{4.173}$$

Solving Equation 4.173 in terms of ϵk yields

$$\epsilon k(t) = \frac{A_o}{C_2 - \rho(a_2 - a_1)\omega^2/a_1} \sin(\omega t). \tag{4.174}$$

Therefore, we obtain the current inner radius, $\bar{a}_1(t)$ with time using Equation 4.166.

4.5 Results

4.5.1 Material Constants and Activation Criterion

The pressure–radius relationships for the tube deformed by the finite extension and inflation given in Equations 4.71 and Equation 4.106 are solved simultaneously in a nonlinear regression iteration loop to find the material constants, C_1, α, γ and the activation criterion, λ_{2a} by fitting the pressure–radius data provided in Atabek's article.[114] A subroutine "RNLIN" in IMSL package of Fortran version 6.0 is used for the analysis of the nonlinear regression. This subroutine fits a nonlinear regression model which is of the form

$$y_i = f(x_i, \theta) + \epsilon_i, \quad i = 1, 2, \ldots, n \tag{4.175}$$

using least squares. θ is the vector of p regression parameters, and the ϵ_i's are independently distributed normal errors with mean zero and variance σ^2. The residuals are

$$e_i(\theta) = y_i - f(x_i, \theta). \quad i = 1, 2, \ldots, n \tag{4.176}$$

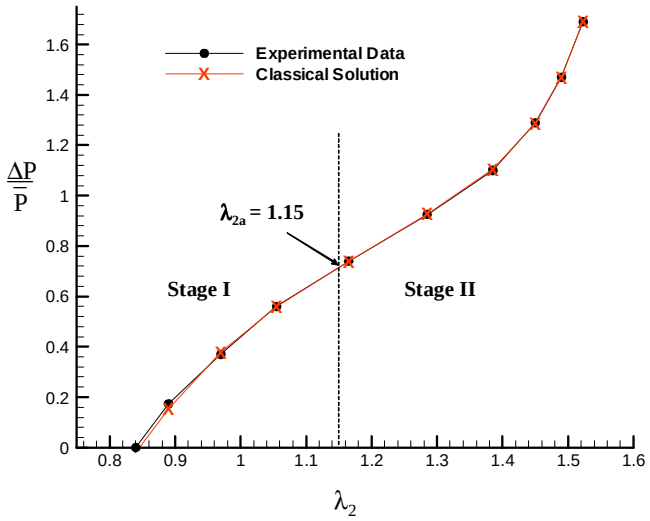

Figure 4.7. Pressure–radius curve fit using the Atabek's data [114] at $\lambda = 1.4$.

A value of θ is determined by minimizing the sum of the individual norms of $e_i(\theta)$. The integration of Equation 4.106 is numerically performed using a subroutine "QDAGS" in the IMSL package.

Under the assumption of isotropic materials, the activation criterion, s_a is a function of both λ_1 and λ_{2a}. Because in the muti mechanisms, the collagen recruitment in a body is assumed to initiate at a unique activation criterion, s_a, the variable s_a must be equal at different stretching ratios, λ_1's. It follows that a value of λ_1 should correspond to a unique value of λ_{2a} such that s_a is unchanged. By fitting all data sets for three stretching ratios in[114] keeping s_a same, we found that curves generated using the three different ratios did not merge in a single curve, as is shown in the pressure-radius curve in.[114] An anisotropic material may be needed to obtain this feature. In this research, we only consider the pressure–radius curve when the stretching ratio, λ_1 is 1.4. Figure 4.7 shows the result of the data fit. In the figure, the pressure is normalized by the systemic pressure. The value of r^2 obtained by the data fit is 0.99. The corresponding material constants and activation criterion are listed in Table 4.1. As shown in Figure 4.7 and Table 4.1, λ_{2a} is found in the vicinity of the inflection

Table 4.1. Material constants and activation criterion .

Constants	C_1	α	γ	λ_{2a}	s_a
	30 KPa	18.6 Kpa	7.49	1.15	0.67

point of the curve. The nonlinear ballooning effect of the arterial wall at a lower level of pressure is recreated by the strain energy using a neo–Hookian model before the collagen recruitment (Stage I). After the collagen straighten out at a higher level of pressure which satisfies the activation criterion, both elastin and collagen fibers start to play a role on the motion and then the arterial wall becomes stiffer. As in Figure 4.7, the exponential behavior in the slope of the curve after the recruitment of collagen fibers (Stage II) is recreated by the strain energy using both neo–Hookian and exponential models. The material constants and activation criterion shown in Table 4.1 are to be used to analyze the periodic motions of arterial wall superposed on the large extension and inflation.

4.5.2 Description of Motion of Arterial Wall by A Small Deformation

The oscillatory behavior of arterial walls is analyzed by the small on large theory. The theory is also applied to the dual mechanisms so that the separate roles of elastin and collagen fibers can be taken account. The material constants and activation criterion in Table 4.1 are used to solve Equation 4.165. The integration of the equation is also numerically performed using the subroutine, "QDAGS".

As in Table 4.1, the value of λ_2 is 1.15 at which the collage fibers come into play. Pressure begins to oscillate after the recruitment of collagen fibers so that the solutions in stage II using the small on large theory (see Equation 4.165) are used to describe the periodic motions of arterial wall. The pressure-radius lines, obtained by deforming the body B at the base pressure by a small inflation and compression under a static loading condition (see Equation 4.161) are presented in Figure 4.8. The figure describes the motion of the wall

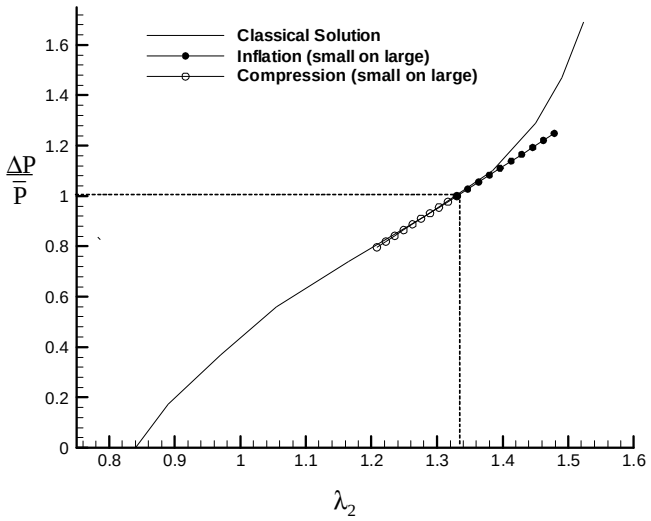

Figure 4.8. Pressure–radius lines by small on large theory under a static loading condition.

pressurized or compressed up to 25% of the average pressure, $100mmHg$. As seen in the figure, the lines for the small inflation and compression are linearly fit to the slope of the curve of large deformations under the static loading condition at the base pressure.

The periodic motions of vessel wall under a sinusoidal pressure force are obtained by Equation 4.174. The density of the artery similar to blood density, ρ and the period of one cardiac cycle in human arteries, T used in[147] were 1000 kg/m^3 and 0.8 sec. We use these values to present the dimensionless inner radius, $\lambda_2(t)$ in Figure 4.9. The figure presents the periodic motions of a vessel wall with time under a sinusoidal pressure force. The trend of the periodic motions of a wall under the sinusoidal pressure force is found to be similar to that under a static loading condition.

4.6 Discussion of Results and Future Work

The mathematical modeling of the motion of arterial walls was motivated by the fact that the periodic behavior of vessel walls can not be simply modeled using linear elasticity

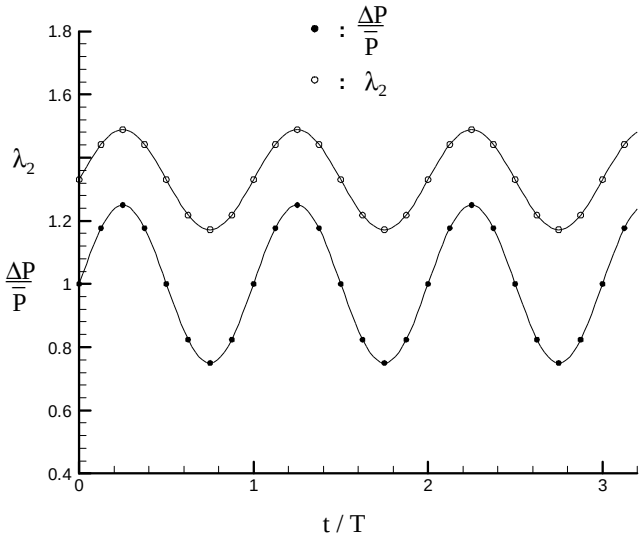

Figure 4.9. Periodic motions of vessel wall under a sinusoidal pressure force.

because *in vivo* arteries are prestretched and preloaded by the average pressure ($100mmHg$) and the deformations by these preloadings are large. Furthermore, several researchers reported the importance of the separate roles of elastin and collagen fibers in arterial wall motion.[112,113,116] The central idea was to approximate the large deformations to obtain a small deformation superposed on the large deformations using a small on large theory in modeling the periodic motions of vessel wall pre-deformed by the base pressure and prestretching. The novelty of this research was to (i) employ a nonlinear constitutive equation for the large deformation region, (ii) develop governing equations for the wall motion using a small on large theory and (iii) include the separate roles of elastin and collagen fibers in modeling vessel walls.

Taking a stress-free body as a reference configuration, we stretched and inflated the body to obtain the pressure-radius relation. During these large deformations, the collagen fibers begin to straighten out and therefore, the proposed constitutive relation accounting for the role of collagen fibers was used to find the pressure-radius relation after the recruitment of collagen fibers. The body at the base pressure was then deformed by the small inflation and

compression under a static loading condition to find the pressure-radius equation. Under a sinusoidal pressure force, a wave equation for the periodic motions of an arterial wall was obtained to solve the radial displacement with time.

The elastin degradation due to development regarded as the "growth" that occurs up to maturation,[120] aging and arterial disease such as aneurysms is reported by many authors.[141,152,153] The axial tension and pressure diameter test on the passive carotid arteries from dogs by Cox[152] revealed that development stiffens the wall, decreasing the distensibility, increasing the collagen fraction and decreasing the elastin fraction. The study of age–associated changes in wall structure by Yin[153] showed an increased deposition of collagen and some degradation of elastin. In the cerebral saccular aneurysmal walls mostly found at bifurcations the elastin and the media are degraded.[141] Therefore, the periodic motions of aged or diseased arterial walls can be predicted through further study using our constitutive model, which includes the separate roles of elastin and collagen fibers.

Blood flow in arteries is coupled to the motion of the vessel wall. Recently, theories for fluid–structure interaction have been applied to study blood flow coupled to the motion of vessel walls in order to find the mechanical factors responsible for arterial diseases. In these studies, the wall is usually modeled as a membrane. In a future work, we will use standard membrane approximations to obtain the governing equations for axisymmetric deformation of a cylindrical membrane composed of the dual mechanism material. The corresponding equations for small on large deformations can subsequently be developed. These membrane equations can then be incorporated into multi-scale models of the circulatory system (e.g.[145]). These multi-scale models also will be useful for investigations of the effects of elastin degradation and collagen remodeling due to aging or arterial diseases.

In this chapter, the arterial wall material was modeled as homogeneous, incompressible and isotropic. Earlier experimental studies of incompressibility of the arterial wall showed

that under physiological conditions of both internal pressure and longitudinal stretch an incompressible assumption is justified.[119] The merging feature shown in the pressure-radius curves at three different stretching ratios reported in[114] could not be predicted using the isotropic dual mechanism model. It is expected that this is due to the anisotropic character of the wall or possibly the need for a more complex function for the activation criterion. Anisotropic materials will be considered in a future work. The effect of residual stress on the stiffness of an arterial wall is reported to be significant[116,120,121] and therefore, also needs to be included in our future work. In developing the dual mechanism model to include prestretch, we used experimental data from the descending canine aorta. Our constitutive model and the theoretical developments for this model using a small on large theory can also be applied to other arteries such as cerebral arteries.

APPENDIX

APPENDIX

A. ACTUAL PROPERTIES OF HUMAN BLOOD BIFURCATION

We evaluate actual pressure values using the dimensionless pressure, $\bar{P}$ and Re (see Equation 2.4), considering two actual diameters, 0.002 and 0.004 meter. The corresponding non-dimensional pressures $\bar{P}$ to the ranges of Re considered are presented in Table A.1. In the table, j represents three different Re ($j = 1, 2, 3$; $Re = 255, 505, 755$). P_j represents pressures obtained numerically corresponding to three different Re cases. In order to obtain the actual pressures, actual velocities should be computed using three different Re. The results are shown in Table A.2. In the table, L_{ai} and D_{ai} are the actual radius and diameter of the parent vessel. i represents two different actual diameters ($i = 1, 2$; diameter = 0.002, 0.004 meter). U_{aij} are the actual velocities. Then the actual pressures can be calculated by

$$P_{ij} = \frac{\bar{P}_j \mu U_{aij}}{L_{ai}}. \tag{A.1}$$

Using the data in Table A.2, the following relationships between the actual and non-dimensional pressures are found.

$$P_{1j} = 3.5\bar{P}_j U_{a1j} \quad when \;\; i = 1 \tag{A.2}$$

$$P_{2j} = 1.75\bar{P}_j U_{a2j} \quad when \;\; i = 2 \tag{A.3}$$

We then finalize our calculations to obtain the actual pressures for the two actual vessel diameters with three Re cases as shown in Table A.3. This table can also be used to calculate actual wall shear stresses for the two actual diameters.

Table A.1. Non dimensional Pressures for Re = 255, 505, 755.

Re	μ (Ns/m^2)	U_j (m/s)	L (m)	P_{in} (Pa)	$\bar{P}_j$
255	0.0035	0.0004245	1	0	673061*P_1
505	0.0035	0.0008418	1	0	339409*P_2
755	0.0035	0.001257	1	0	227371*P_3

Table A.2. Calculations of Actual Velocities for Re = 255, 505, 755.

Re	ρ (kg/m^3)	P_{in} (Pa)	D_{a1}(m)	D_{a2}(m)	L_{a1}(m)	L_{a2}(m)	U_{a1j}(m/s)	U_{a2j}(m/s)
255	1050	0	0.002	0.004	0.001	0.002	0.425	0.2125
505	1050	0	0.002	0.004	0.001	0.002	0.8417	0.4208
755	1050	0	0.002	0.004	0.001	0.002	1.2583	0.6292

Table A.3. Relationship between Actual Pressures and Obtained Pressures for Re = 255, 505, 755.

AP	P_{11}	P_{12}	P_{13}	P_{21}	P_{22}	P_{23}
	1001178*P_1	999882*P_2	1001353*P_3	250294.6*P_1	249941*P_2	250358*P_3

APPENDIX

B. GENERAL THEORY OF SMALL DEFORMATIONS SUPERPOSED ON FINITE DEFORMATION (SMALL ON LARGE THEORY)

We consider a unstrained body B_o and strained body B by a known finite deformation of B_o. A strained body B is deformed to $\bar{B}$ by the infinitesimal displacements of the material points in B. The material points P_o of the body B_o are displaced to P of the body B by a known finite deformation. The points P are displaced to the points P' of the body $\bar{B}$ by an infinitesimal displacement. Then the displacement vector $\vec{P_oP'}$ can be written

$$\mathbf{v}(\theta_1, \theta_2, \theta_3, t) + \epsilon \mathbf{w}(\theta_1, \theta_2, \theta_3, t), \tag{B.1}$$

where ϵ is a constant, $\mathbf{v}$ and $\mathbf{w}$ is the displacement vector $\vec{P_oP}$ and $\vec{PP'}$, respectively, θ_i are the covariant coordinate system. ϵ is small so that ϵ^2 and higher order powers of ϵ are negligible. The covariant base vectors of θ_i at points P of the body B are

$$\mathbf{G}_i = \mathbf{R}_{,i} = \mathbf{v}_{,i} + \mathbf{r}_{,i}\,, \tag{B.2}$$

where $()_{,i}$ denote $\partial()/\partial\theta^i$. So, the covariant base vectors of θ_i at points P' of the body $\bar{B}$ are denoted by

$$\mathbf{G}_i + \epsilon \mathbf{G}'_i = \mathbf{v}_{,i} + \mathbf{r}_{,i} + \epsilon \mathbf{w}_{,i}\,. \tag{B.3}$$

The term of ϵ is then

$$\mathbf{G}'_i = \mathbf{w}_{,i}\,. \tag{B.4}$$

The displacement vector $\mathbf{w}$ can be written in terms of either contravariant or covariant

components by

$$\mathbf{w} = w_m \mathbf{G}^m = w^m \mathbf{G}_m. \tag{B.5}$$

Then, $\mathbf{G}'_i$ can be obtained by

$$\mathbf{G}'_i = w_m \|_i \mathbf{G}^m = w^m \|_i \mathbf{G}_m, \tag{B.6}$$

where

$$\begin{aligned} w_m \|_i &= w_{m,i} - \Gamma^s_{mi} w_s, \\ w^m \|_i &= w^m{}_{,i} + \Gamma^m_{si} w^s, \end{aligned} \tag{B.7}$$

where Γ^s_{mi} is the Christoffel symbol of the second. Based on $\mathbf{G}'_i$, we can obtain the covariant metric tensor G'_{ij}, contravariant metric tensor G'^{ij}, contravariant base vectors $\mathbf{G}'^i$ and the determinant of the metric tensor G' of the body $\bar{B}$ as follows.

$$\begin{aligned} G'_{ij} &= w_i \|_j + w_j \|_i, \\ G'^{ij} &= -G^{ir} G^{js} G'_{rs}, \\ \mathbf{G}'^i &= G^{ij} \mathbf{G}'_j + G'^{ij} \mathbf{G}_j, \\ G' &= G G^{ij} G'_{ij}. \end{aligned} \tag{B.8}$$

The strain invariants of the body $\bar{B}$ based on above results become

$$\begin{aligned} I_1 + \epsilon I'_1 &= g^{rs}(G_{rs} + \epsilon G'_{rs}), \\ I_2 + \epsilon I'_2 &= g_{rs}(G^{rs} + \epsilon G'^{rs})(I_3 + \epsilon I'_3), \\ I_3 + \epsilon I'_3 &= (G + \epsilon G')/g, \end{aligned} \tag{B.9}$$

so that

$$\begin{aligned} I_1' &= g^{rs}G_{rs}', \\ I_2' &= g_{rs}(G'^{rs}I_3 + G^{rs}I_3'), \\ I_3' &= G'/g. \end{aligned} \tag{B.10}$$

We assume that the vessel walls are homogeneous isotropic materials. Then, the elastic potential for the body B is a form of

$$W = W(I_1, I_2, I_3), \tag{B.11}$$

where

$$I_1 = g^{rs}G_{rs}, \quad I_2 = g_{rs}G^{rs}I_3, \quad I_3 = G/g \tag{B.12}$$

The elastic potential for the body $\bar{B}$ then becomes

$$W = W(I_1 + \epsilon I_1', I_2 + \epsilon I_2', I_3 + \epsilon I_3'). \tag{B.13}$$

The contravariant stress tensor τ^{ij} for the body B is expressed by

$$\tau^{ij} = \Phi g^{ij} + \Psi B^{ij} + pG^{ij}, \tag{B.14}$$

where the scalar invariants Φ, Ψ, p and B^{ij} are

$$\Phi = \frac{2}{\sqrt{I_3}}\frac{\partial W}{\partial I_1}, \quad \Psi = \frac{2}{\sqrt{I_3}}\frac{\partial W}{\partial I_2}, \quad p = 2\sqrt{I_3}\frac{\partial W}{\partial I_3}, \tag{B.15}$$

$$B^{ij} = I_1 g^{ij} - g^{ir}g^{js}G_{rs}. \tag{B.16}$$

By Taylor's expansion, using the scalar invariants $\Phi + \epsilon\Phi', \Psi + \epsilon\Psi', p + \epsilon p'$ for the body $\bar{B}$,

we obtain

$$\begin{aligned}\Phi' &= AI_1' + FI_2' + EI_3' - \frac{\Phi}{2I_3}I_3', \\ \Psi' &= FI_1' + BI_2' + DI_3' - \frac{\Psi}{2I_3}I_3', \\ p' &= I_3(EI_1' + DI_2' + CI_3') + \frac{p}{2I_3}I_3',\end{aligned} \tag{B.17}$$

where

$$\begin{aligned}A &= \frac{2}{\sqrt{I_3}}\frac{\partial^2 W}{\partial I_1^2}, \quad B = \frac{2}{\sqrt{I_3}}\frac{\partial^2 W}{\partial I_2^2}, \quad C = \frac{2}{\sqrt{I_3}}\frac{\partial^2 W}{\partial I_3^2}, \\ D &= \frac{2}{\sqrt{I_3}}\frac{\partial^2 W}{\partial I_2 \partial I_3}, \quad E = \frac{2}{\sqrt{I_3}}\frac{\partial^2 W}{\partial I_3 \partial I_1}, \quad F = \frac{2}{\sqrt{I_3}}\frac{\partial^2 W}{\partial I_1 \partial I_2},\end{aligned} \tag{B.18}$$

The tensor B^{ij} becomes $B^{ij} + \epsilon B'^{ij}$ for the body $\bar{B}$ and using G'_{ij},

$$B'^{ij} = (g^{ij}g^{rs} - g^{ir}g^{js})G'_{rs}. \tag{B.19}$$

To the first order of ϵ of the stress tensor $\tau^{ij} + \epsilon\tau'^{ij}$ and $T_i + \epsilon T_i'$ for the strained body $\bar{B}$,

$$\tau'^{ij} = g^{ij}\Phi' + B^{ij}\Psi' + B'^{ij}\Psi + G'^{ij}p + G^{ij}p', \tag{B.20}$$

$$\mathbf{T}_i' = \sqrt{G}\lambda^{ij}\mathbf{G}_j, \quad \lambda^{ij} = \tau'^{ij} + \tau^{im}w^j\|_m + \tau^{ij}w^m\|_m. \tag{B.21}$$

Finally, the equations of motion for B and $\bar{B}$ when the body force and acceleration vectors for the body $\bar{B}$ are $\mathbf{F} + \epsilon\mathbf{F}'$ and $\mathbf{f} + \epsilon\mathbf{f}'$ are

$$\begin{aligned}\mathbf{T}_{i,i} + \rho\mathbf{F}\sqrt{G} &= \rho\mathbf{f}\sqrt{G}, \\ \mathbf{T}'_{i,i} + \rho\mathbf{F}'\sqrt{G} &= \rho\mathbf{f}'\sqrt{G},\end{aligned} \tag{B.22}$$

where ρ is the density. Equation B.23 can be rewritten using Equation B.21 in the form

$$\lambda^{ij}\|_i + \rho F'^j = \rho f'^j, \tag{B.23}$$

where

$$\mathbf{F}' = F'^j \mathbf{G}_j, \quad \mathbf{f}' = f'^j \mathbf{G}_j. \tag{B.24}$$

BIBLIOGRAPHY

BIBLIOGRAPHY

1. H.N. Sabbah, F. Khaja, E.T. Hawkins, J.F. Brymer, T.M. McFarland, J. Bel–Kahn, P.T. Doerger, P.D. Stein, Relation of atherosclerosis to arterial wall shear in the left anterior descending coronary artery of man, Am Heart J 112:453–458, 1986.

2. N.D. Garcia, Focal and Regional Responses of Endothelium to Disturbed Flow In Vitro, Ph D. thesis, Massachusetts Institute of Technology, Cambridge, MA., 1987

3. J. Ravensbergen, J.W. Ravensbergen, J.K.B. Krijger, B. Hillen, H.W. Hoogstraten, Localizing Role of Hemodynamics in Atherosclerosis in Several Human Vertebrobasilar Junction Geometries, American Heart Association, 18(5): 708-716, May 1998.

4. M.M. Adel, S.L. Alper, S. Izumo, Hemodynamic Shear Stress and Its Role in Atherosclerosis, JAMA, December 1, 1999, Vol 282, No. 21, pp. 2035–2040.

5. A. Remuzzi, C.F. Dewey, P.F. Davies, M.A. Gimbrone, Orientation of Endothelial Cells in Shear Fields in vitro, Biorheology, 21; 617–630, 1984.

6. P.F. Davies, T. Mundel, K.A. Barbee, A Mechanism for Heterogeneous Endothelial Responses to Flow in vivo and in vitro, J. Biomechanics, Vol. 28, No. 12, pp. 1553–1560, 1995.

7. I. Levitan, B.P. Helmke, P.F. Davies, A Chamber to Permit Invasive Manipulation of Adherent Cells in Laminar Flow with Minimal Disturbance of the Flow Field, Annals of Biomedical Engineering, Vol. 28, pp. 1184–1193, 2000.

8. C. F. Dewey, Jr., S. R. Bussolari, M. A. Gimbrone, Jr., P. F. Davies, The dynamic response of vascular endothelial cells to fluid shear stress, ASME Journal of Biomechanical Engineering 103 (1981) 177–185.

9. B. R. Blackman, K. A. Barbee, L. E. Thibault, In vitro cell shearing device to investigate the dynamic response of cells in a controlled hydrodynamic environment, Annals of Biomedical Engineering 28 (2000) 363–372.

10. M.M. Peel, P.A. Dimilla, Effect of Cell–Cell Interactions on the Observable Strength of Adhesion of Sheets of Cells, Annals of Biomedical Engineering, Vol. 27, pp. 236–246, 1999.

11. A. I. Barakat, P. Davies, Responsiveness of vascular endothelium to shear stress: Potential of ion channels and cellular skeleton (Review), International Journal of Molecular Medicine 4 (1999) 323–332.

12. T. Iba, S.E. Sumpio, Morphological Response of Human Endothelial Cells Subjected to Cyclic Strain in Vitro, Microvascular Research 42, 245-254 (1991).

13. O. Thoumine, R.M. Nerem, P.R. Girard, Oscillatory Shear Stress and Hydrostatic Pressure Modulate Cell Matrix Attatchment Proteins in Cultured Endothelial Cells, In Vitro Cell. Dev. Biol. 31A:45–54, January 1995.

14. N. Resnick, M. A. Gimbrone, Jr., Hemodynamic forces are complex regulators of endothelial gene expression, The FASEB Journal 9 (1995) 874–882.

15. M.A. Haidekker, N. L'Heureux, J.A. Frangos, Fluid Shear Stress increases Membrain Fluidity in Endothelial Cells: A Study with DCVJ Fluorescence, Am J Physiol Heart Circ Physiol. 2000 Apr;278(4):H1401-6.

16. N. DePaola, M. A. Gimbrone, Jr., P. F. Davies, C. F. Dewey, Jr., Vascular endothelium responds to fluid shear stress gradients, Arterioscler Thromb 12(11) (1992) 1254–1257: Correction: 1993;13:465.

17. E. A. Nauman, K. J. Risic, T. M. Keaveny, R. L. Satcher, Quantitative assessment of steady and pulsatile flow fields in a parallel plate flow chamber, Annals of Biomedical Engineering 27 (1999) 194–199.

18. J. A. Frangos, L. McIntire, S. G. Eskin, Shear stress induced stimulation of mammalian cell metabolism, Biotechnology and Bioengineering 32 (1988) 1053–1060.

19. L. M. Khachigian, K. R. Anderson, N. J. Halnon, M. A. Gimbrone Jr., N. Resnick, T. Collins, Egr-1 is activated in endothelial cells exposed to fluid shear stress, Arteriosclerosis, Thrombosis and Vascular Biology 17 (1997) 2280–2286.

20. A. M. Malek, S. L. Alper, S. Izumo, Hemodynamic shear stress and its role in atherosclerosis, JAMA 282 (1999) 2035–2042.

21. R. M. Nerem, Hemodynamics and the vascular endothelium, J. Biomech. Engrg. 115 (1993) 510–514.

22. K. Kayembe, M. Sasahara, F. Hazama, Cerebral aneurysms and variations in the circle of Willis, Stroke 15 (1984) 846–850.

23. T. Sasaki, N. Kodama, H. Itokawa, Aneurysm formation and rupture at the site of anastomosis following bypass surgery, J. Neurosurg. 85 (1996) 500–502.

24. L. N. Sekhar, R. C. Heros, Origin, growth, and rupture of saccular aneurysms: A review, Neurosurger. 8 (1981) 248–260.

25. S. Rodbard, Vascular caliber. cardiology, Science 60 (1975) 4–49.

26. S. Rossitti, P. Svendsen, Shear stress in cerebral arteries supplying arteriovenous malformations, Acta Neurochir Wien. 137 (1995) 138–145.

27. B. B. BC, J. Abe, W. Min, J. Surapisitchat, C. Yan, Endothelial atheroprotective and anti-inflammatory mechanisms, Ann N Y Acad Sci. 947 (2001) 93–109.

28. J. C. Stanley, W. E. Burkel, J. W. Ford, D. W. Vinter, R. H. Kahn, W. M. Whitehouse, Jr., L. M. Graham, Enhanced patency of small-diameter, externally supportediliofemoral grafts seeded with endothelial cells, Surgery 92 (1982) 994–1005.

29. S. E. Greenwald, C. L. Berry, Improving vascular grafts: the importance of mechanical and haemodynamic properties, J Pathol. 190(3) (2000) 292–9.

30. A. Ratcliffe, Tissue engineering of vascular grafts, Matrix Biol 19(4) (2000) 353–7.

31. N. DePaola, P. F. Davies, W. F. Pritchard, Jr., L. Florez, N. Harbeck, D. C. Polacek, Spatial and temporal regulation of gap junction connexin43 in vascular endothelial cells exposed to controlled disturbed flows *in vitro*, Proc Natl Acad Sci U S A 96(6) (1999) 3154–9.

32. T. Nagel, N. Resnick, C. F. Dewey, Jr., M. A. Gimbrone, Jr., Vascular endothelial cells respond to spatial gradients in fluid shear stress by enhanced activation of transcription factor, Arteriscler. Thromb.Vasc. Biol. 19 (1999) 1–16.

33. X. P. Bao, C. Y. Lu, J. A. Frangos, Temporal gradient in shear but not steady shear stress induces pdgf-a and mcp-1 expression in endothelial cells - role of no, nf kappa b, and egr-1., Arteriosclerosis Thrombosis and Vascular Biology 19(4) (1999) 996–1003.

34. C.R. White, M. Haidekker, X. Bao, J. A. Frangos, Temporal gradients in shear but not spatial gradients, stimulate endothelial cell proliferation., Circulation. 103 (2001) 2508–2513.

35. R. M. Lum, L. M. Wiley, A. I. Barakat, Influence of different forms of fluid shear stress on vascular endothelial tgf-beta 1 mrna expression, International Journal of Molecular Medicine 5(6) (2000) 635–641.

36. U. Pohl, J. Holtz, R. Busse, E. Bassenge, Crucial role of endothelium in the vasodilator response to increased flow *in vivo*, Hypertension 8 (1986) 37–44.

37. L. Langille, F. O'Donnel, Reductions in arterial diameter produced by chronic decreases in blood flow are endothelium-dependent, Science 231 (1986) 405–407.

38. J. A. Frangos, S. G. Eskin, L. V. McIntire, C. L. Ives, Flow effects on prostacyclin production by cultured human endothelial cells, Science 227(4693) (1985) 1477–1479.

39. M. J. Levesque, R. M. Nerem, The elongation and orientation of cultured endothelial cells in response to shear stress, J. Biomech. Eng. 107 (1985) 341–347.

40. J.-J. Chiu, D. L. Wang, S. Chien, R. Skalak, S. Usami, Effects of disturbed flow on endothelial cells, ASME Journal of Biomechanical Engineering 120 (1998) 2–8.

41. S. P. Olesen, D. E. Clapham, P. F. Davies, Haemodynamic shear stress activates a k+ current in vascular endothelial cells, Nature 331(6152) (1988) 168–170.

42. E. R. Jacobs, C. Cheliakine, D. Gebremedhin, E. Birks, P. Davies, D. Harder., Shear activated channels in cell-attatched patches of cultured bovine aortic endothelial cells, Eur. J. Phys. 431 (1995) 129–131.

43. S. R. Bussolari, C. F. Dewey, Jr., M. A. Gimbrone, Jr., Apparatus for subjecting living cells to fluid shear stress, Rev Sci Instrum. 53(12) (1982) 1851–1854.

44. R. Ross, Cell biology of atherosclerosis, Annu Rev Physiol. 57 (1995) 791–804.

45. J. E. Gabriels, D. L. Paul, Connexin43 is highly localized to sites of disturbed flow in rat aortic endothelium but connexin37 and connexin40 are more uniformly distributed, Circ Res 83(6) (1998) 636–643.

46. D. B. Cowan, S. J. Lye, B. L. Langille, Regulation of vascular connexin43 gene expression by mechanical loads, Circ Res 82(7) (1998) 786–793.

47. A. Hotz-Wagenblatt, D. Shalloway, Gap junctional communication and neoplastic transformation, Crit Rev Oncog 4(5) (1993) 541–58.

48. J. Ruel, J. Lemay, G. Dumas, C. Doillon, J. Charara, Development of a parallel plate flow chamber for studying cell behvavior under pulsatile flow, ASAIO J. 41 (1995) 876–883.

49. K. Ookawa, M. Sato, N. Ohshima, Changes in the microstructure of cultured porcine aortic endothelial cells in the early stage after applying a fluid-imposed shear stress, J. of Biomechanics 25 (1992) 1321–1328.

50. F. M. White, Fluid Mechanics, 4th Edition, McGraw-Hill, 1999.

51. C. Kahane, On the spatial analyticity of weak solutions of the Navier-Stokes equations, Arch. Rat. Mech. Anal. **33** (1969) 386–405.

52. H. Schlichting, Boundary-Layer Theory, McGraw-Hill, Inc., 1987.

53. O. Yadoff, Sur les écoulements à la Poiseuille, C.R. Acad. Sci. Paris 223 (1946) 192–193.

54. O. Yadoff, Sur le calcul des débits dans les écoulements permanents à la Poiseuille, C.R. Acad. Sci. Paris 224 (1947) 374–376.

55. R. Berker, Fluid dynamics II, in: C. Truesdell (Ed.), Handbuch der Physik, Vol. VVIII/2, Springer-Verlag, 1963, Ch. Intégration des équations du mouvement d'un fluide visqueux incompressible, pp. p 70–71.

56. K. Bathe, Finite Element Procedures, Prentice Hall, 1996.

57. P. M. Gresho, Some current CFD issues relevant to the incompressible Navier-Stokes equations, Comput. Methods Appl. **87** (1991) 201–252.

58. J. G. Heywood, R. Rannacher, S. Turek, Artificial boundaries and flux and pressure conditions for the incompressible Navier-Stokes equations, International Journal for Numerical Methods in Fluids **22** (1996) 325–352.

59. M. Bathe, R. Kamm, A fluid-structure interaction finite element analysis of pulsatile blood flow through a compliant stenotic artery, J. Biomechanical Engineering 121 (1999) 361–369.

60. K. Kondratiev, Asymptotics of solution of the Navier–Stokes equation near angular points of the boundary, Prikl. Math. Mech. 31 (1967) 119–123.

61. I.V. Haljasmaa, A.M. Robertson, G.P. Galdi, On the Effect of Apex Geometry on Wall Shear Stress and Pressure in Two-Dimensional Models of Arterial Bifurcations, Mathematical Models and Methods in Applied Sciences, Vol.11, No.3, 2001, pp.499-520.

62. M.H. Friedman, L.W. Ehrlich, Numerical simulation of aortic bifurcation flows: the effect of flow divider curvature, Journal of Biomechanics, Vol. 17, No. 12: 881-888, 1984.

63. X. He and D.N. Ku, Pulsatile flow in the human left coronary artery bifurcation : Average conditions, ASME Journal of Biomechanical Engineering, 118, 74-82 (1996).

64. X.Y. Xu, M.W. Collins, and C.J.H. Jones, Flow studies in canine artery bifurcations using a numerical simulation method, ASME J. Biomechanical Engineering, 114, 504-511 (1992).

65. G.N. Foutrakis, H. Yonas, and R.J. Sclabassi, Blood pressure management of patients with cerebral aneurysms guided by computer modeling, AANS (April, 1996).

66. Bathe, K.J., 1996, Finite Element Procedures, Prentice Hall, NJ.; ADINA Theory and Modeling Guide, 1995,1999 article

67. C.G. Caro, The mechanics of the circulation, pp. 173-176.

68. WE. Stehbens, Etiology of interacranial berry aneurysms, J Neurosurg 1989;70:823-831.

69. C.W. Kerber, G. Steven, Imbesi, and K. Knox, Flow dynamics in a lethal anterial communicating artery aneurysm, AJNR Am J Neuroradiol 20:2000-2003, November/December 1999, technical note.

70. C.W. Kerber, S.T. Hecht, K. Knox, R.B. Buxton, and H.S. Meltzer, Flow dynamics in a fatal aneurysm of the basilar artery, AJNR Am J Neuroradiol 17:1417-1421, September 1996.

71. G.J. Hademenos, The physics of cerebral aneurysms, Physics Today, pp.24-30 February 1995.

72. H. K. Moffatt, Viscous and resistive eddies near a sharp corner, J. Fluid Mech. 18 (1964) 1–18.

73. G.N. Foutrakis, H. Yonas, and R.J. Sclabassi, Finite element methods in the simulation and analysis of intracranial blood flow, Neurological Research, April 1997, Volume 19, pp.174-186.

74. G.G. Ferguson, Physical factors in the initiation, growth, and rupture of human intracranial saccular aneurysms, J. Neurosurg. Volume 37 : 666-677, December 1972.

75. H. Niimi, Y. Kawano, and I. Sugiyama, Structure of blood flow through a curved vessel with an aneurysm, Bioreology, 21:603-615, 1984.

76. G.N. Foutrakis, H. Yonas, and R.J. Sclabassi, Saccular aneurysm formation in curved and bifurcating arteries, AJNR Am J Neroradiol 20: 1309-1317, August 1999.

77. M. Lów, K. Perktold, R. Raunig, Hemodynamics in rigid and distensible saccular aneurysms: A numerical study of pulsatile flow characteristics, Biorhology, 30: 287-298, 1993.

78. M.R. Roach, S. Scott, and G.G. Ferguson, The hemodynamic importance of the geometry of bifurcations in the Circle of Willis (glass model studies), Stroke, Vol. 3: 255-267, May-June 1972.

79. E.S. Connolly, R.A. Solomon, Management of symptomatic and asymptomatic unruptured aneurysms, Neurosurgery Clinics of North America, Vol. 9, Number 3: 509-525, July 1998.

80. W.D. Forbus, On the origin of miliary aneurysms of the superficial cerebral arteries, Bulletin of the Johns Hopkins Hospital, Vol. 47, Num. 5: 239-284, 1930.

81. W.E. Stehbens, R.M. Ludatscher, Ultrastructure of the renal arterial bifurcation of rabbits, Exp Mol Pathol, 18: 50-67, 1973.

82. H.N. Sabbah, F. Khaja, E.T. Hawkins, J.F. Brymer, T.M. McFarland, J. Bel-Kahn, P.T. Doerger, and P.D. Stein, Relation of atherosclerosis to arterial wall shear in the left anterior descending coronary artery of man, American Heart Journal, 112: 453-458, 1986.

83. C.S. Lee, J.M. Tarbell, Wall shear rate distribution in an abdominal aortic bifurcation model: effects of vessel compliance and phase angle between pressure and flow waveforms, Journal of Biomechanical Engineering, Vol. 119: 333-342, August 1997.

84. K. Hayashi, Y. Yanai, T. Naiki, A 3D-LDA study of the relation between wall shear stress and intimal thickness in a human aortic bifurcation, Journal of Biomechanical Engineering, Vol. 118: 273-279, August 1996.

85. Z. Lou, W. Yang, A computer simulation of the non-Newtonian blood flow at the aortic bifurcation, Journal of Biomechanics, Vol. 26, No. 1: 37-49, 1993.

86. Z. Lou, W. Yang, Biofluid dynamics at arterial bifurcations, Critical Reviews in Biomedical Engineering, 19(6):455-493, 1992.

87. K. Perktold, R.O. Peter, M. Resch, G. Langs, Pulsatile non- Newtonian blood flow in three dimensional carotid bifurcation models: a numerical study of flow phenomena under different bifurcation angles, Journal of Biomedical Engineering, Vol. 13: 507-515, November 1991.

88. K. Perktold, M. Hofer, G. Rappitsch, M. Loew, B.D. Kuban, M.H. Friedman, Validated computation of physiologic flow in a realistic coronary artery branch, Journal of Biomechanics, 31: 217-228, 1998.

89. A.E. Green, R.S. Rivlin, R.T. Shield, Proc. R. Soc. A211 (9152) 128.

90. D.A. Caulk, P.M. Naghdi, Axisymmetric motion of a viscou fluid inside a slender surface of revolution, Journal of Applied Mecahnics March 1987, Vol. 54 pp: 190-196.

91. V. A. Solonnikov, On the Stokes equations in domains with non-smooth boundaries and on viscous incompresible ow with a free surface, in Pittman Research Notes in Mathematics Series, Longman Scientific and Technical, College de France Seminar, Vol. III, 70 (1982) 340–423.

92. A.E. Green, P.M. Naghdi, M.L. Wenner, 1974, Proceedings of the Royal Society of London, Vol. A 337, pp: 451-483.

93. J.G. Walmsley, M.R. Campling, and H. Chertkow, Interrelationship among wall structure, smooth muscle orientation, and contraction in human major cerebral arteries, Stroke, 14, 781-790 (1983).

94. H.M. Finlay, P. Whittaker, and P.B. Canham, Collagen organization in the branching region of human brain arteries, Stroke, 29, 1595-1601 (1998).

95. T.W.R. Macfarlane, S. Petrowski, L. Rigutto, and M.R. Roach, Computer–based video analysis of cerebral arterial geometry using the natural fluorescence of the arterial wall and contrast enhancement techniques, Blood Vessels, 20, 161-171 (1983).

96. T.W.R. Macfarlane, A computer–based quantitative image analysis of the geometry of human cerebral arterial bifurcations. PhD thesis, University of Western Ontario, 1985.

97. T.W.R. Macfarlane, M.R. Roach, and K. Chan, The geometry of human cerebral bifurcations : effect of static distending pressure, J. Biomechanics, 13, 265-277 (1980).

98. B.J. Chung, A.M. Robertson, D.G. Peters, The numerical design of a parallel plate flow chamber for investigation of endothelial cell response to shear stress, Computers and Structures, 81, p.535-546, 2003.

99. Carmichael R (1950), The pathogenesis of non-inflammatory cerebral aneurysms., J Pathol Bacteriol 62:1-19.

100. Carmichael R (1945), Gross defects in the muscular and elastic coats of the larger cerebral arteries., J Pathol Bacteriol 57:345-351.

101. Glynn I (1940) Medial defects in the circle of Willis and their relation to aneurysm formation., J Path Bact 51:213-219.

102. W.E. Stehbens, Medial defects in the cerebral arteries of man, J Pathol Bacteriol 78: 179-185, 1959.

103. G.G. Ferguson, Physical factors in the initiation, growth, abd rupture of human intracranial aneurysms., J Neurosurg, 37, 666-677.

104. S. A. Nazarov and B. A. Plamenevskiı, Elliptic Problems with Piecewise Smooth Boundaries, W. De Gruyter Expositions in Mathematics, Vol. 13 (Springer, 1994).

105. Eppinger H, Pathogenesis (Histogenesis and Aetiologie) der aneurysmen einschliesslich des aneurysma equi verminosum. Arch Klin Chir 35(Suppl I): 1-563, 1887.

106. T. Crawford, Some observations on the pathogenesis and natural history of incranial aneurysms, J Neurol Neurosurg Psychiat, 1959; 22:259-266.

107. H. Demiray, Stresses in Ventricular Wall, Journal of Applied Mechanics, Transactions of the ASME, vol. 98 pp : 194-197, 1976.

108. L.M. Srivastava and V.P. Srivastava, 1985, Interaction of peristaltic flow with pulsatile flow in circular cylindrical tube, J. Biomechanics, volume : 18(4), pp. 247-253.

109. Ling, Geometric and Elastic Nonlinear Effects, A.I.A.A. Paper no. 70-789

110. Patel, Austen, Greenfield and Tindall, Impedence of Certain large blood vessels in man., Ann. N.Y. Acad. Sci. volume 115, 1964, p 1129.

111. A.S. Saada, Elasticity Theory and Applications, Pergamon Press Inc. 1974.

112. M.R. Roach and A.C. Burton, The reason for the shape of the distensibility curves of arteries, Can. J. Biochem. Physiol. 35 (1957).

113. A.C. Burton, Physiol. Revs. 34. 619 (1954).

114. S.C. Ling and H.B. Atabek, A nonlinear analysis of pulsatile flow in arteries, J. Fluid Mech. vol. 55, part 3, pp. 493-511 (1972).

115. A.E. Green, R.S. Rivlin and R.T. Shield, General theory of small elastic deformations superposed on finite elastic defomations, Proc. R. Soc. A211 pp. 128-154 (1952).

116. G.A. Holzapfel, T.C. Gasser and R.W. Ogden, A new constitutive frame work for arterial wall mechanics and a comparative study of material models, Journal of Elasticity 61: 1-48 (2000).

117. H. Wolinsky, S.Glagov, Structural basis for the static mechanical properties of the aortic media, Circ Res., 14: 400-413 (1964).

118. P.B. Dobrin, Distribution of Lamellar Deformations (Implications for properties of the arterial media), Hypertension, 33: 806-810 (1999).

119. T.E. Carew, R.N. Vaishnav and D.J. Patel, Compressibility of the arterial wall, Circulation Research, Vol. XXIII, july 1968.

120. J.D. Humphrey, Mechanics of the arterial wall : Review and Directions, Critical Reviews in Biomedical Engineering, Vol. 23 / Issues 1 & 2 (1995).

121. R.N. Vaishnav and J. Vassoughi, Estimation of residual stresses in aortic segments, In CW Hall (ed), Biomedical Engineering II, Recent Developments, PP. 330-333, Newyork, Pergamon Press. (1983).

122. T. Crawford, Some observations on the pathogenesis and natural history of incranial aneurysms, J Neurol Neurosurg Psychiat, 1959; 22:259-266.

123. R. M. Nerem, Vascular fluid mechanics, the arterial wall, and atheroclerosis, J Biomech Eng 114: 274-282, 1992.

124. R.H. Cox, Three–dimensional mechanics of arterial segments in vitro : methods, Journal of Applied Physiology, Vol. 36, No. 3, March 1974.

125. P.B. Dobrin and T.R. Canfield, Elastase, Collagenase, and the biaxial elastic properties of dog carotid artery, Am. J. Physiol. 247 (Heart Circ. Physiol. 16) : H124-H131 (1984).

126. P.B. Dobrin, W.H. Baker and W.C. Gley, Elastolytic and collagenolytic studies of arteries (Implications for the mechanical properties of aneurysms), Arch Surg 1984;119:405-409.

127. J.A.G. Rhodin, Archtecture of the vessel wall, in Handbook of Physiology, Sect. 2, Vol. 2, Berne, RM., Ed., Am. Physiol. Soc., 1979.

128. D.W. Fawcett, A Textbook of Histology, W.B. Saunders, Philadelphia, 1986.

129. S. Chien, S. Li, J. Y-J. Shyy, Effects of Mechanical Forces on Signal Transduction and Gene Expression in Endothelial Cells, Hypertension, 1998; 31[part 2]: 162-169.

130. J. Hildebrandt, H. Fukaya and C.J. Martin, Simple uniaxial and uniform biaxial deformation of nearly isotropic incompressible tissues, Biophysical Journal Vol. 9 pp. 781-791 (1969).

131. P.B. Dobrin Vascular mechanics. In: Handbook of Physiology. The Cardiovasular System. Bethesda, MD: Am. Physiol. Soc., 1983, Sect. 2, Vol. III, chap. 3, pp. 65-102.

132. J.D. Humphrey, An evaluation of pseudoelastic descriptors used in arterial mechanics, J. Biomech. Engr. 121 (1999) 259-262.

133. C.J. Chuong, Y.C. Fung, Three–dimensional stress distribution in arteries, J. Biomech. Engr. 105 (1983) 268-274.

134. M.I. Cohen, D.M. Wang and J.M. Tarbell, Measurement of oscillatory flow pressure gradient in an elastic artery model, Biorheology, Vol. 32, No. 4, pp. 459-471, 1995.

135. A.E. Green and W. Zerna, Theoretical elasticity, 2nd Edition, Oxford University Press. 1968.

136. DJ. P.W. Gerald Austen, J.C. Greenfield, G.T. Tindall, Impedance of certain large blood vessles in man, Annals New York Academy of Sciences, pp. 1129-1139.

137. A. S. Wineman and K. R. Rajagopal. On a constitutive theory for materials undergoing microstructural changes. Arch. Mech., 42:53-75, 1990.

138. K. R. Rajagopal and A. S. Wineman. A constitutive equation for nonlinear solids which undergo deformation induced microstructural changes. International Journal of Plasticity, 8:385-395, 1992.

139. A. S. Wineman and H. E. Huntley. Numerical simulation of the effect of damaged induced softening on the inflation of a circular rubber membrane. Int. J. Solids Structures, 31:3295-3313, 1994.

140. L. Formaggia, J.F. Gerbeau, F.Nobile, A. Quarteroni, On the coupling of 3D and 1D Navier–Stokes equations for flow problems in compliant vessels, Comput. Methods Appl. Mech. Engrg. 191:561-582, 2001.

141. R. Wulandana, A Nonlinear And Inelastic Constitutive Euation For Human Cerebra Arterial And Aneurysm Walls, PhD thesis, University of Pittsburgh, 2003.

142. R. Wulandana, A.M. Robertson, A.M; Use of A Multi-Mechanism constitutive Model for Inflation of Cerebral Arteries, Proceedings of the First Joint BMES/EMBS Conference, p.235, 1999.

143. R. Wulandana, A.M. Robertson, A.M; A Model of Early Stage Aneurysm Development Based on an Inelastic Multi–Mechanism Constitutive Model, BED–Vol. 50, ASME 2001 Bioengineering Conference, p. 419-420, 2001.

144. M. Heiland, T.J. Pedley, Large Axisymmetric Deformation of A Cylindrical Shell Conveying A Viscous Flow, Journal of Fluids and Structures (1995) 9,237-256.

145. A. Quarteroni, M. Tuveri, A. Veneziani, Computational Vascular Fluid Dynamics: Problems, Models and Methods, Comp. Vis. Science 2 (2000) 163-197.

146. K. Perktold, E. Thurner and T. Kenner, Flow and Stress Charateristics in Rigid Walled and Compliant Carotid Models, Medic. and Biolog. Eng. and Comp., 32:19-26, 1994.

147. X. Ma, G.C. Lee, S.G. Wu, Numerical Simulation for the Propagation of Nonlinear Pulsatile Waves in Arteries, Journal of Biomechanical Engineering, Vol. 114:490-496, November, 1992.

148. M. Zamir, The Physics of Pulsatile Flow, 2000 Springer–Verlag New York, Inc.

149. S.G. Wu, G.C. Lee, N.T. Tseng, Nonlinear Elastic Analysis of Blood Vessels, Journal of Biomechanical Engineering, Vol. 106:376-383, November, 1984.

150. Z. Lou, W-J. Yang, A computer Simulation of the Blood Flow at the Aortic Bifurcation with Flexible Walls, Journal of Biomechanical Engineering, Vol. 115:306-315, August, 1993.

151. D. Tang, C. Yang, H. Walker, S. Kobayashi, D.N. Ku, Simulating cyclic artery compression using a 3D unsteady model with fluid–structure interactions, Computers and Structures 80 (2002) 1651–1665.

152. R.H. Cox, Carotid artery mechanics, connective tissue and electrolyte changes in puppies, Am. J. Physiol., 227. 563-568, 1974.

153. F.C.P. Yin, The aging vasculature and its effects on the heart, in The Aging Heart, Vol. 12, Weisfeldt. M.L., Ed., Raven Press, New York, 1980.

154. T. J. Ingall, J. P. Whisnant, D. O. Wiebers, and W. M. O'Fallon. Has there been a decline in subaracnoid hemorrhage mortality. Stroke, 20:718–724, 1989.

155. J. P. Broderick, T. G. Brott, J. E. Duldner, T. Tomsick, and A. Leach. Initial and reccurent bleeding are the major causes of death following subarachnoid hemorrhage. Stroke, 25:1342–1347, 1994.

156. R. L. Sacco, P. A. Wolf, N. E. Bharucha, S. L. Meeks, W. B. Kannel, L.J. Charette, P.M. McNamara, E. P. Palmer, and R. D'Agostino. Subarachnoid and intracerebral hemorrhage: Natural history, prognosis and percursive factors in the Framingham study. Neurology, 34:847–854, 1984.

157. K. Perktold, M. Resch and H. Florian, Pulsatile non-Newtonian flow characteristics in a three dimensional human carotid bifurcation model, Journal of Biomechanical Engineering, Vol. 113:464–475, Nov. 1991.